STELLAR MAGNETISM AND ACTIVITY
FROM STELLAR INTERIORS TO ORBITING EXOPLANETS

Wyke Chun Victor See

A Thesis Submitted for the Degree of PhD
at the
University of St Andrews

2016

Full metadata for this item is available in
St Andrews Research Repository
at:
http://research-repository.st-andrews.ac.uk/

Please use this identifier to cite or link to this item:
http://hdl.handle.net/10023/9602

This item is protected by original copyright

This item is licensed under a
Creative Commons Licence

Stellar magnetism and activity

From stellar interiors to orbiting exoplanets

by

Wyke Chun Victor See

University of
St Andrews

FOUNDED
1413

Submitted for the degree of Doctor of Philosophy in Astrophysics

September 2016

Declaration

I, Wyke Chun Victor See, hereby certify that this thesis, which is approximately 30,000 words in length, has been written by me, and that it is the record of work carried out by me, or principally by myself in collaboration with others as acknowledged, and that it has not been submitted in any previous application for a higher degree.

Date Signature of candidate

I was admitted as a research student in September 2012 and as a candidate for the degree of PhD in September 2012; the higher study for which this is a record was carried out in the University of St Andrews between 2012 and 2016.

Date Signature of candidate

I hereby certify that the candidate has fulfilled the conditions of the Resolution and Regulations appropriate for the degree of PhD in the University of St Andrews and that the candidate is qualified to submit this thesis in application for that degree.

Date Signature of supervisor

Copyright Agreement

In submitting this thesis to the University of St Andrews I understand that I am giving permission for it to be made available for use in accordance with the regulations of the University Library for the time being in force, subject to any copyright vested in the work not being affected thereby. I also understand that the title and the abstract will be published, and that a copy of the work may be made and supplied to any bona fide library or research worker, that my thesis will be electronically accessible for personal or research use unless exempt by award of an embargo as requested below, and that the library has the right to migrate my thesis into new electronic forms as required to ensure continued access to the thesis. I have obtained any third-party copyright permissions that may be required in order to allow such access and migration, or have requested the appropriate embargo below.

The following is an agreed request by candidate and supervisor regarding the electronic publication of this thesis: Access to Printed copy and electronic publication of thesis through the University of St Andrews.

Date Signature of candidate

Date Signature of supervisor

Collaboration Statement

This thesis is the result of work I conducted at the University of St Andrews between September 2012 and April 2016. Some of the work presented is published in scientific journals as part of the peer review process. All text in this thesis is written by me and all figures in this thesis have been produced by me unless explicitly stated in the figure's caption.

- Chapter 3 is based of *"The energy budget of stellar magnetic fields*", V. See, M. Jardine, A. A. Vidotto, J.-F. Donati, C. P. Folsom, S. Boro Saikia, J. Bouvier, R. Fares, S. G. Gregory, G. Hussain, S. V. Jeffers, S. C. Marsden, J. Morin, C. Moutou, J. D. do Nascimento Jr, P. Petit, L. Rosén, I. A. Waite, 2015, Monthly Notices of the Royal Astronomical Society, 453, 4301-4310. Data, in the form of Zeeman-Doppler maps, were provided by J.-F. Donati, C. P. Folsom, S. Boro Saikia, R. Fares, S. V. Jeffers, S. C. Marsden, J. Morin, J. D. do Nascimento Jr, P. Petit, L. Roén and I. A. Waite. C. P. Folsom provided the code that outputs the magnetic field energies form the Zeeman-Dopper maps. All co-authors of this paper provided comments on the final manuscript.

- Chapter 4 is based of *"The connection between stellar activity cycles and magnetic field topology*", V. See, M. Jardine, A. A. Vidotto, J.-F. Donati, C. P. Folsom, S. Boro Saikia, J. Bouvier, R. Fares, S. G. Gregory, G. Hussain, S. V. Jeffers, S. C. Marsden, J. Morin, C. Moutou, J. D. do Nascimento Jr, P. Petit, L. Rosén, I. A. Waite. This manuscript has been submitted to Monthly Notices of the Royal Astronomical Socity for peer review. Data, in the form of Zeeman-Doppler maps, were provided by J.-F. Donati, C. P. Folsom, S. Boro Saikia, R. Fares, S. V. Jeffers, S. C. Marsden, J. Morin, J. D. do Nascimento Jr, P. Petit, L. Roén and I. A. Waite. C. P. Folsom provided the code that outputs the magnetic field energies form the Zeeman-Dopper maps. All co-authors of this paper provided comments on the submitted manuscript.

- Chapter 5 is based of *"The effects of stellar winds on the magnetospheres and potential habitability of exoplanets*", V. See, M. Jardine, A. A. Vidotto, P. Petit, S. C. Marsden, S. V. Jeffers, J. D. do Nascimento Jr, 2014, Astronomy & Astrophysics, 570, A99. Data, in the form of chromospheric observations, were provided by S. C. Marsden. I developed the code required for the calculations in this work. All co-authors of this paper provided comments on the final manuscript.

- Chapter 6 is based of *"Time-scales of close-in exoplanet radio emission variability*", V. See. M. Jardine, R. Fares, J.-F. Donati, C. Moutou, 2015, Monthly Notices of the Royal Astronomical Society, 450, 4323-4332. Data, in the form of Zeeman-Doppler maps, were provided by R. Fares. M. Jardine provided the code, originally written by A. A. van Ballegooijen (see van Ballegooijen et al. (1998)), to carry out the field extrapolation. I adapted this code to perform calculations required for this work. All co-authors of this paper provided comments on the final manuscript.

Abstract

The study of magnetic fields on low-mass stars is important due to their ubiquity. They are responsible for phenomena spanning a wide range of spatial and temporal scales. Over the last two decades, the Zeeman-Doppler imaging (ZDI) technique has been used to study the topologies of stellar magnetic fields. A great deal has been learnt about how the magnetic characteristics of cool dwarfs vary as a function of parameters such as mass, rotation or age.

In this thesis, I assemble a sample of stars with Zeeman-Doppler maps. I study their poloidal and toroidal components as a function of fundamental parameters and also in relation to activity cycles. I find that the relationship between poloidal and toroidal fields is different for stars above and below the fully convective boundary, in line with previous ZDI studies. I also find that the fields of strongly toroidal stars must be generated axisymmetrically. With regards to activity cycles, I find that so called “inactive branch" stars appear to remain poloidal throughout their activity cycle while so called “active branch" stars appear to be able to generate strong toroidal fields.

Magnetic activity can also interact with exoplanets that may be orbiting a star. In this thesis, I consider two such interactions. The first is the compression of planetary magnetospheres by stellar winds. Sufficiently powerful winds can strip a planet of its atmosphere and render it uninhabitable. However magnetospheric shielding can provide some protection. I show that planets around $0.6\,M_\odot$ - $0.8\,M_\odot$ stars are the most likely to be able to protect their atmospheres. The second interaction I consider is exoplanetary radio emission. I present a wind model and show that exoplanetary radio emissions will depend strongly on the structure of the magnetic field structure of the central star.

Acknowledgements

After 4 years and roughly 30,000 words of thesis, I find myself at the end of a PhD - a feat that would not have been possible without the support of more people than I can name in these pages.

First and foremost, I must thank my parents for raising me in the manner that they did. Though I do not necessarily always say or show it, I greatly appreciate all they have done to give me the best chance at succeeding in life.

The members of the astro group also deserve mentioning. Thanks to Jo, Joe, Jack, Gabriella, Josh, David, Milena, Louise and James for sharing an office with me. There were laughs, tears and more than several projectile pens! For those who heard the coffee song, I hope you remember it for many years to come. Thanks to Rim and Aline for all their support - for reading and re-reading my paper drafts and for encouraging words before and after talks. And thanks to everyone else in the department who I ever shared a laugh, an interesting discussion or a drink with. I am grateful for it all.

And where would I be without Breakaway? Gwenllian, to whom I insisted I wouldn't join the committee (whoops!), and Christine, who insisted to me she wouldn't do a PhD (whoops again!), thanks for introducing me to the Scottish hills and being excellent housemates. Sophia, we joined committee at the same time and have survived right through to the end. It was a crazy and mostly sanity-free ride and I wouldn't change it for all the fairy gnomes in the world. Ed, Rosie, Phil, Sonia, the Lizzies, Michael and Marissa - the old guard. Thanks for teaching me to navigate with an OS map and a compass! And thanks to everyone I've climbed a hill with or who have kept me entertained during Whey Pat socials - Pip, Becca, Kate, George, Francis, the Pollys, the Katies, everyone I've already mentioned and everyone else I can't mention without this becoming a who's who of Fudge's Facebook friends.

And finally, my greatest thanks must go to Moira. You have supported me in every aspect of my academic life - putting out my minor panics, throwing conference talks my way and helping my future career prospects. The unique and infectious "Moira" spin you put on everything has made my time working with you incredibly amusing and deeply rewarding. I'm not sure if I ever told you but it was rather serendipitous that I ended up working with you. How glad I am for such a stroke of luck.

“Remember to look up at the stars and not down at your feet. Try to make sense of what you see and wonder about what makes the universe exist. Be curious."

Stephen Hawking

“If we knew what we were doing, it wouldn’t be called research"

Unknown but often
attributed to Albert Einstein

Contents

Declaration i

Copyright Agreement iii

Collaboration Statement v

Abstract vii

Acknowledgements ix

1 Introduction 1

1.1 Motivation . . . 1

1.2 Generating magnetic fields . . . 3

1.3 Observing stellar magnetic fields . . . 5

1.3.1 Absorption lines and the Zeeman effect . . . 5

1.3.2 Spectropolarimetry . . . 7

1.3.3 Zeeman-Doppler imaging . . . 9

1.4 Properties of stellar magnetic fields . . . 10

1.4.1 Effect of stellar mass . . . 11

1.4.2 Effect of rotation period . . . 13

1.4.3 Magnetic cycles . . . 14

1.5 Solar and stellar winds . . . 16

1.5.1 Early models . . . 16

1.5.2 Determining stellar wind properties . . . 16

1.5.3 Modern wind models and simulations . . . 18

1.6 Exoplanets and their host stars . . . 19

1.6.1 Searching for exoplanets . . . 19

1.6.2 Exoplanet characterisation from wind interactions . . . 21

1.7 Thesis outline 22

2 Field Modelling 23

2.1 Spherical Harmonics 23

2.2 Representing magnetic fields 27

2.2.1 Magnetic fields at the stellar surface 28

2.2.2 Non-potential surface fields 29

2.2.3 Extrapolating the 3D coronal field 30

3 The energy budget of stellar magnetic fields 35

3.1 Introduction 35

3.2 Stellar sample 37

3.3 Results 38

3.3.1 Toroidal Fields 38

3.3.2 Field saturation 40

3.3.3 Different dynamo modes? 42

3.3.4 Band latitudes 44

3.3.5 Field orientation 45

3.4 Conclusion 48

3.A Data tables 51

4 The connection between stellar activity cycles and magnetic field geometry 55

4.1 Introduction 55

4.1.1 Solar and stellar activity cycles 55

4.1.2 Solar and stellar magnetic cycles 57

4.2 Sample selection 59

4.3 Results 61

4.3.1 Field properties 61

4.3.2 Activity-rotation relation 63

4.3.3 Activity cycle branches 63

4.4 Discussion 65

4.4.1 Large-scale field geometry along activity branches 65

4.4.2 Magnetic vs chromospheric cycles 67

4.4.3 Breaking the degeneracy in rotation period/Rossby number 68
4.5 Conclusions 70
4.A Data tables 71

5 The effects of stellar winds on the magnetospheres and potential habitability of exoplanets 73
5.1 Introduction 73
5.1.1 The habitable zone 74
5.1.2 Other factors that affect habitability 75
5.2 Stellar wind models 78
5.2.1 Parker wind model 78
5.2.2 Cranmer and Saar model 80
5.3 Results and discussion 81
5.3.1 Magnetospheric extent within the habitable zone 81
5.3.2 Comparison with other work 85
5.3.3 Evolution of planetary systems 88
5.3.4 Observing Earth-analogues 89
5.4 Conclusion 90
5.A Data tables 93

6 Time-scales of close-in exoplanet radio emission variability 97
6.1 Introduction 97
6.2 Radio emission model 101
6.2.1 Stellar magnetic field extrapolation 103
6.2.2 Stellar wind 105
6.3 Stellar system properties 107
6.4 Results 109
6.4.1 HD 179949 109
6.4.2 HD 189733 110
6.4.3 τ Boo 113
6.4.4 Rest of sample 115
6.5 Discussion & Conclusion 115
6.A Runaway electron generation and the acceleration region 117

7 Conclusions and outlook **119**

7.1 Magnetic properties of low-mass dwarfs 119

7.2 Exoplanet-wind interactions 121

7.3 Outlook 122

Bibliography **123**

List of Figures

1.1 Images of the Sun during the June 2012 Venus transit taken with NASA's Solar Dynamics Observatory. The images are taken in visible light (left), at 304Å (middle) and 355Å (right) corresponding roughly to the photosphere, chromosphere and corona respectively. It is clear that active regions seen in the continuum correspond to magnetic structures seen higher up in the solar atmosphere. Courtesy of NASA/SDO and the AIA, EVE, and HMI science teams 2

1.2 Illustrations of the Ω- and α-effects. The Ω-effect (top) winds up an initially poloidal field, via differential rotation, into a toroidal field. As flux tubes buoyantly rise through the convection zone, coriolis forces induces twists in the field lines causing loops to form. This regenerates the poloidal field from the toroidal field, i.e the α-effect (bottom). 4

1.3 Left: a sketch of an energy level diagram for an atom and the associated spectrum. Only a single transition is usually possible. In the presence of a magnetic field however, the upper energy level splits. The corresponding spectrum is broadened into π, σ_{red} and σ_{blue} components. Right: the polarisation of the π, σ_{red} and σ_{blue} components as viewed from various orientations with respect to the magnetic field direction. In this example, the magnetic field orientation is in the z direction. When the observer's line of sight is parallel to the magnetic field (in the z direction), no π component is visible and the σ_{red} and σ_{blue} components are circularly polarised. When the observer's line of sight is perpendicular to the field line (in the x-y plane), all three components are linearly polarised though the π component is at 90 degrees to the other two components. Figure reproduced with permission from Reiners (2012). 7

1.4 The filters required to measure each polarisation state in the Stokes vector. The four components of the Stokes vector are I - unpolarised light, Q - linearly polarised light, U - linearly polarised light (at 45° to Q) and V - circularly polarised light. 9

1.5 A sample of stars with ZDI maps plotted in mass - rotation period space. The size of each point corresponds to the average magnetic field energy density at the surface of the star, red/blue symbols correspond to stars that are strongly poloidal/toroidal and regular polygons/star shapes correspond to stars that have axisymmetric/non-axisymmetric fields. Mathematical definitions of these quantities can be found in section 2.2.2. Figure reproduced from Donati & Landstreet (2009) with permission. 11

1.6 The magnetic characteristics of a sample of M dwarfs. The format is the same as Fig. 1.5. Above $0.5\,M_{\odot}$, stars show weak, non-axisymmetric fields and below this mass, stars show strong, poloidal and axisymmetric fields. Below $0.2\,M_{\odot}$, stars with both types of field coexist in a relatively small region of parameter space. Figure reproduced from Morin et al. (2010) with permission. 12

1.7 Average surface magnetic field strength (green) and percentage of fields that are poloidal (red) vs rotation rate for a sample of four solar mass stars. Figure reproduced with permission from Petit et al. (2008). 14

1.8 Magnetic field maps at the source surface (the limit of coronal confinement, see section 2.2.3) of τ Boo during seven different epochs. Maps are organised by year from left to right and by month from top to bottom. Global polarity switches occur with a ~ 1 year period and can be most easily seen in the 2007 June → 2008 June → 2009 June maps and the 2010 January → 2011 January maps. The field extrapolations required to construct these source surface maps can be found in See et al. (2015a) using data from Donati et al. (2008b), Fares et al. (2009) & Fares et al. (2013). 15

1.9 Mass-loss rates vs X-ray surface flux. Below the wind dividing line, $F_X \sim 10^6\,\mathrm{ergs\,cm^{-2}\,s^{-1}}$, the mass-loss rates are correlated with X-ray emission. However, this correlation breaks down for high activity stars. Figure reproduced with permission from Wood et al. (2014). 17

1.10 The 3D magnetic topology of τ Boo. This obtained from a 3D, self consistent simulation that uses a ZDI map as an inner boundary condition. Figure reproduced with permission from Vidotto et al. (2012). 19

1.11 Mass vs separation from host star for all confirmed exoplanets as of 11th January 2016. The colour for each point represents the methods used to discover the exoplanet - blue, red, green and brown for the transit, radial velocity, microlensing and direct imaging techniques respectively. This plot was made using the publicly available tools at exoplanets.org/plots. 20

2.1 A visualisation of the real part of $P_{lm}e^{im\phi}$ for the lowest l and m values. Expressions for P_{lm} are given in equation (2.15). Red and blue regions correspond to opposite polarities. It can be seen that m defines the number of nodal crossings in the ϕ direction while $l-m$ defines the number of nodal crossings in the θ direction. 26

2.2 A visualisation of how various spherical harmonic modes are modified by the potential field source surface model. Shown are the field lines of a pure dipole (top left), pure quadrupole (top right) and their geometries under the PFSS model (bottom row). Each panel shows a 2D cut in the (r,θ) plane. The dashed red lines indicate the location of the source surface. 31

3.1 A map of the azimuthal toroidal field of ξ Boo A. A ring of uni-directional field can clearly be seen. Data provided by Petit et al. (in prep). 36

3.2 The rotation periods and masses of each star in the sample. Filled blue points indicate stars observed at one epoch while open red data points indicate stars observed over multiple epochs. Dashed lines are included showing a stellar mass of $0.5\,\mathrm{M}_\odot$ and Rossby numbers of 0.01, 0.1 and 1.0. 37

3.3 Top: toroidal magnetic energy against poloidal magnetic energy. Stars with multiple maps are connected by grey lines. The dotted line indicates $\langle B^2_{\rm tor}\rangle = \langle B^2_{\rm pol}\rangle$. The sample is split into stars less massive (pentagon markers) and more massive than $0.5\,\mathrm{M}_\odot$ (circle markers). See text for further discussion of how these sub-samples were chosen. The two dashed lines are best fit lines for these sub-samples; $\langle B^2_{\rm tor}\rangle \propto \langle B^2_{\rm pol}\rangle^a$ with $a = 0.72 \pm 0.08$ and $a = 1.25 \pm 0.06$ for $\mathrm{M} < 0.5\,\mathrm{M}_\odot$ and $\mathrm{M} > 0.5\,\mathrm{M}_\odot$ respectively. AB Dor is shown with triangles. Each point is colour coded by stellar mass. Bottom: toroidal energy fraction against stellar mass. Format is the same as the top panel. Data-points are also colour coded by stellar mass to aid comparison with the top panel. While the two panels show very similar information, the difference in behaviours of the two mass ranges is much clearer in the bottom panel. 39

3.4 The ratio of X-ray to bolometric luminosity, $R_{\rm X} = L_{\rm X}/L_{\rm bol}$, against rotation period (left) and Rossby number (right). Both show increasing, and eventual saturation of, $R_{\rm X}$ with more rapid rotation. However, the scatter is vastly reduced when plotted as a function of Rossby number. Figure reproduced with permission from Wright et al. (2011). 40

3.5 Poloidal (top) and toroidal (bottom) magnetic energy against Rossby number. The formatting is the same as Fig. 3.3. Right/left facing arrows indicate stars that only have lower/upper estimates for their Rossby numbers. The saturated and unsaturated regimes can be clearly seen with the transition occurring at a Rossby number of approximately 0.1. Fits to the stars in the unsaturated regime, $\langle B^2_{\rm pol}\rangle \propto \mathrm{Ro}^{-2.25\pm0.19}$ and $\langle B^2_{\rm tor}\rangle \propto \mathrm{Ro}^{-2.99\pm0.28}$, are shown with dashed lines. Note: the magnetic energy axes of the two plots are not the same. 41

3.6 Left: the latitude at which the toroidal azimuthal field peaks for each star as a function of stellar rotation period. Each point is colour coded by stellar mass. The size of the points indicates the full-width half-maximum value for the band (see inset). Stars with multiple maps are connected by grey lines. Numerical values for the data points are included in Table 3.2. Right: a sketch of a solar type star showing the radiative core and convective outer layer. Arrows representing the buoyant rise of a flux tube from the tachocline is shown for a slowly rotating star (purple arrow) and a rapid rotator (blue arrow). Flux tubes are deflected to higher latitudes in more rapidly rotating stars. 45

3.7 Percentage of total magnetic energy contained in the axisymmetric component of the field against percentage of total magnetic energy contained in toroidal field. Stars observed at multiple epochs are connected by grey lines. The data points are colour coded by stellar mass and scale with the total magnetic energy density, $\langle B^2\rangle$ (see inset). Rosén et al. (2015) reconstructed the surface field of II Peg using Stokes IV (circularly polarised light) and also Stokes IQUV (circularly and linearly polarised light). These data points are shown by black diamond and square markers respectively. 46

3.8 Axisymmetric poloidal energy as a percentage of total poloidal energy (top panel) and axisymmetric toroidal energy as a percentage of total toroidal energy (bottom panel) as a function of toroidal energy. Format is the same as Fig. 3.7 48

3.9 Axisymmetric poloidal energy as a percentage of total poloidal energy against axisymmetric toroidal energy as a percentage of total toroidal energy. Format is the same as Fig. 3.7. Similarly to Fig. 3.7, the inset shows $\langle B^2 \rangle$ values of 5×10^{-1}G^2 to 5×10^6G^2 in multiples of 10 for the smallest to biggest points. The numerical values are omitted due to lack of space. 49

4.1 The sunspot record since 1874 as collected by the Royal Greenwich Observatory. Top: the latitude of sunspots is plotted as a function of time. The spots appear in two bands that move towards the equator as the solar cycle progresses forming the so called butterfly diagram. Bottom: the percentage of the visible hemisphere of the Sun that is covered in sunspots as a function of time. Both panels show that sunspots behave periodically with a time-scale of ~11 years. Image used from NASA in accordance with their media usage guidelines. 56

4.2 Panel (a) - (c): the axis of the dipole component of the solar magnetic field is plotted for solar cycles 21-23. Panel (d): The latitude of the dipole axis is plotted as a function of time. The solar magnetic dipole is mostly aligned or anti-aligned with the solar rotation axis. However, roughly every 11 years, it undergoes a polarity flip in a comparatively short amount of time. Figure reproduced from DeRosa et al. (2012) with permission, ©AAS. 58

4.3 The rotation periods and masses of the stars presented in table 4.1. Blue and red markers correspond to stars on the active and inactive branches respectively (see section 4.3). 60

4.4 Panel a: the sample of stars used in chapter 3 plotted in stellar mass-rotation period space. This is a similar plot to Fig. 3 of Donati & Landstreet (2009). The symbol colour represents the toroidal energy fraction (ranging from red for purely poloidal, i.e. $f_{\text{pol}} = 1$, to blue for purely toroidal, i.e. $f_{\text{pol}} = 0$) and symbol shape represents how axisymmetric the poloidal component of the field is (ranging from decagons for a purely axisymmetric poloidal field, i.e. $f_{\text{axi,pol}} = 1$, to pointed stars for a purely non-axisymmetric field, i.e. $f_{\text{axi,pol}} = 0$). Due to the large number of stars in the sample, symbol sizes have been kept the same for clarity and do not scale with $\log\langle B^2 \rangle$ as is usual with this type of plot. A dotted line indicates Ro = 1. Panel b: chromospheric activity cycle period against rotation period for the sample of Böhm-Vitense (2007) plotted with open circles (see their Fig. 1). Dashed lines indicate the active and inactive branches. Overplotted is the sample outlined in section 4.2 where symbol colour and shape have the same meaning as panel a. In this panel, symbol size does scale with $\log\langle B^2 \rangle$ as indicated by the key. Stars with multiple cycle periods are connected with a dashed line. On both panels the shaded region indicates the range of rotation periods where the active and inactive branches overlap. 62

4.5 Panel a: toroidal energy fraction against Rossby number for the sample of stars used chapter 3 (open square symbols). Stars observed at multiple epochs are joined by solid lines. Panel b: the ratio of X-ray to bolometric luminosity against Rossby number reproduced from Wright et al. (2011) (grey dots; see their Fig. 2). Panel c: the ratio of chromospheric cycle frequency to rotational frequency against Rossby number reproduced from Saar & Brandenburg (1999) (open circle symbols; see their Fig. 1). Panel d: chromospheric cycle period against Rossby number using the sample of Böhm-Vitense (2007). In panels c and d, stars with multiple cycles are connected by dashed lines. In each panel, the sample presented in table 4.1 is plotted with blue and red circles denoting active and inactive branch stars respectively. 64

5.1 The habitable zone distances (blue shaded region) shown as a function of host star mass. Overplotted are the solar system planets as well as a number of exoplanets that have been discovered in the habitable zones of their host stars. The habitable zones of lower mass stars that are cooler lie at smaller orbital distances compared to those of higher mass stars. Used with permission from Kasting et al. (2014). 74

5.2 An illustration of how the auroral oval angle of a planet (the angle between the pole and the last open field line), θ_{oval}, is affected by magnetosphere size, r_{ms}. As a crude first order estimate, θ_{oval} can be approximated by truncating a dipole to the size of the magnetosphere. In the figure, closed field lines are shown with solid lines while open field lines are shown with dotted lines. The figure clearly shows smaller values of θ_{oval} for larger magnetospheres. 76

5.3 Magnetospheric size as a function of host star mass for the Parker (left) and CS (right) wind models. The Bcool sample of solar-type stars is plotted with circles and the Sun is indicated by a star symbol. Values for these standoff distances can be found in App. A. Typical errorbars for this sample are indicated in the upper left of each panel. Magnetospheric sizes computed assuming constant activity, $\log R'_{\text{HK}} = -5.1, -4.8, -4.4, -4.0$, are plotted as solid lines. These correspond to chromospheric ages of 8.4, 3.2, 0.3, 0.008 Gyr respectively. It is worth noting that the Earth developed an oxygen rich atmosphere near 1.5 Gyr which corresponds to a solar chromospheric activity of $\log R'_{\text{HK}} = -4.6$. The upper limit for magnetospheric sizes as calculated by Vidotto et al. (2013), for a sample of M dwarfs, are plotted with squares. All points and curves are colour coded by chromospheric activity. The upper dashed line indicates the present day magnetosphere size and the shaded area indicates a range of possible Paleoarchean magnetosphere sizes. 82

5.4 Mass-loss rates per unit surface area as a function of X-ray flux for the Parker (left) and CS (right) models are plotted in blue. Values for these mass-loss rates can be found in App. A. The mass-loss rates and the wind dividing line of Wood et al. (2014) are overplotted in red (see their Fig. 4). These authors fit a power law (red solid line), $\dot{M} \propto F_X^{1.34\pm0.18}$, to their data points below the wind dividing line. For the Bcool data, I find power laws of $\dot{M} \propto F_X^{0.30\pm0.02}$ and $\dot{M} \propto F_X^{0.67\pm0.10}$ for the Parker and CS models respectively (solid blue lines). If I use the entire sample, I find $\dot{M} \propto F_X^{0.38\pm0.01}$ and $\dot{M} \propto F_X^{0.72\pm0.07}$ respectively. I note that the quoted errors are in the fit only. 86

5.5 Each star is plotted in Ca II H & K luminosity-bolometric luminosity space and colour coded according to the magnetospheric size of its planet according to the Parker wind model. HD 107213 and HD 18256 have not been plotted because of their large luminosities. Low-luminosity and low-activity stars, i.e. the stars below the Vaughan-Preston gap, represent optimum observing targets. 90

6.1 Image of Jupiter taken by NASA's Hubble Space Telescope. Overlayed are images of the auroral regions taken in UV. Auroral emissions are clearly visible in the auroral oval where radio emissions also originate from. 99

6.2 Radiometric Bode's law for the magnetised solar system planets. The figures show that the emitted radio power is proportional to the incident kinetic flow power (left) and the incident magnetic power (right) from the solar wind. Used with permission from (Zarka et al., 2001). 100

6.3 Examples of the magnetic field geometries of HD 179949 (2009 September), HD 189733 (2008 July), and τ Boo (2011 January). For each star, maps of the radial magnetic field at the stellar surface (first row) and source surface (second row) are shown. The colour bars indicate the magnetic field strengths in Gauss. Polarity inversion lines are shown with dashed lines. White dots on the surface maps indicate the foot points of the field lines that connect with the planet around the orbit. The large-scale 3D coronal field structure between the stellar surface and the source surface is also shown (third row). Closed and open field lines are coloured in red and blue respectively. Finally, the stellar wind ram pressure, for all latitudes and longitudes, at the orbit of the planet are shown in units of 10^{-6} dyne cm^{-2} (fourth row). All the stars display a complex field at the photosphere but a dipole dominated field exists at the source surface because higher order spherical harmonics decay more quickly with distance above the stellar surface. Three dimensional structure exists in the ram pressure and the stellar magnetic pressure (which has a structure similar to that seen in the second row). 104

6.4 Properties of the HD 179949 system during the 2007 June (left) and 2009 September (right) epochs. Top: Magnetic field maps of the source surface displayed in the same format as Fig. 6.3. Bottom: Predicted planetary radio flux (red) and stellar magnetic field strength along the planetary orbit (blue) as a function of the stellar longitude of the subplanetary point. Large drops in radio emission are evident as the planet crosses the polarity inversion line. . . . 110

6.5 Properties of the HD 189733 system during the 2007 June (left) and 2008 July (right) epochs. Data displayed in the same format as Fig. 6.4. 111

6.6 Properties of the τ Boo system over seven epochs. Data is displayed in the same format as Figure 6.5. The predicted radio flux displayed is that which could be expected if τ Boo b's subplanetary point sampled every stellar latitude. However it remains fixed at a single stellar longitude, 180°, due to tidal locking. Black vertical lines are included to indicate this longitude. The expected radio flux, at any given epoch, is given by the intersection of the red and black lines. Figure 6.7 shows how this flux varies with time. 112

6.7 Predicted radio flux of τ Boo b as a function of time. The connecting lines are visual aids only and should not be interpreted as a form of interpolation. Each epoch is plotted with a different symbol to allow easier comparison with Figs. 6.8 and 6.9. In contrast to HD 189733, where the principle source of variability can be attributed to the orbital motion of the planet, variations in radio flux are caused by dynamo driven evolution of the stellar magnetic field. 113

6.8 Location of the negative pole of the dipole component of τ Boo's magnetic field during each epoch. Lines connecting contiguous epochs are visual aids only and should not be interpreted as a form of interpolation. For each epoch, the symbol used is the same as that used in Fig. 6.7. The negative poles during 2009 June and 2010 January epochs are very close (latitude $\sim 8^\circ$ and longitude $\sim 180^\circ$) and only appear to be a single data point in this plot. 114

6.9 Radio flux as a function of angular separation between the subplanetary point and the closest magnetic pole of τ Boo during each epoch. Symbol shapes correspond to those used in Figs. 6.7 and 6.8. Filled symbols are used if the nearest pole is negative (the points plotted in Fig. 6.8) and unfilled symbols are used if the nearest pole is positive (antipodal to those in Fig. 6.8). A trend of decreasing radio flux can clearly be seen for increasing angular separation from the nearest stellar magnetic pole. 115

List of Tables

3.1 Parameters of our sample: star ID, alternative name, stellar mass, rotation period, Rossby number, $\langle B^2 \rangle$ (which is proportional to the magnetic energy density), toroidal magnetic energy (as a percentage of total energy), axisymmetric magnetic energy (as a percentage of total energy), poloidal axisymmetric magnetic energy (as a percentage of poloidal energy), toroidal axisymmetric magnetic energy (as a percentage of toroidal energy) and the observation epoch. Similarly to Vidotto et al. (2014), we have grouped the stars into solar-like stars, young Suns, hot Jupiter hosts and M dwarfs. References indicate the paper where the magnetic map was originally published. For the remaining parameters, references can be found in Vidotto et al. (2014) and references therein. 51

3.2 Numerical values for Fig. 3.6. For each star the rotation period, latitude of the band and the full-width half-maximum of the band are listed. 53

4.1 Parameters for the stars used in this study, ordered by Rossby number: spectral type, rotation period, convective turnover time, Rossby number, primary and secondary cycle period (if one exists), X-ray to bolometric luminosity ratio, toroidal energy fraction and the epoch of the observations from which each ZDI map was reconstructed. Each star is categorised as an active (A) or inactive (I) branch star corresponding to the blue and red points in Fig. 4.5. The paper from which cycle periods are taken are referenced with a superscript on each cycle period value. Similarly, the paper where each magnetic map was originally published is referenced with a superscript in the observation epoch column. Cycle periods listed as fair or poor under the false alarm probability scheme of Baliunas et al. (1995) are shown in brackets. For the remaining parameters, references can be found in Vidotto et al. (2014). 71

5.1 The numerical values used in this study for the present day Earth's magnetic moment (Tarduno et al., 2010), solar coronal number density (Guhathakurta et al., 1996), luminosity (Harmanec & Prša, 2011), X-ray luminosity (Judge et al., 2003), chromospheric activity (Mamajek & Hillenbrand, 2008), and mass loss rate (Cranmer & Saar, 2011). In addition, the values for the velocity (chosen to be roughly the escape velocity), number density (Balikhin et al., 1993), and ram pressure ($P^{\mathrm{E}}_{\mathrm{ram}} = mn^{\mathrm{E}}_{\mathrm{sw}}(v^{\mathrm{E}}_{\mathrm{sw}})^2$) of the solar wind in the vicinity of the Earth are also listed. 80

5.2 Magnetospheric standoff distances, r_{ms} for the five fictitious planets with the largest values of r_{ms} in the Parker (top 5 results) and CS (bottom 5 results) models. Superscripts indicate the model used. Stars with large activity ranges have minimum and maximum magnetospheric sizes listed. Ram pressure and magnetospheric sizes for the entire sample are shown in appendix 5.A 83

5.3 Ram pressure, P_{ram}, exerted on a hypothetical Earth analogue located in the centre of the habitable zone, r_{HZ}, the corresponding magnetospheric size, r_{ms}, and the mass-loss rates, $\dot{M}$, for the Bcool sample of stars. Superscripts indicate the wind model used. 93

6.1 Properties of the HD 189733, HD 179949 and τ Boo systems. Listed are the spectral type, stellar mass and radius, planetary orbital radius, stellar rotation period, planetary orbital and synodic periods and distance from the Sun. All values referenced from Fares et al. (2013) with the exception of P_{syn} (calculated) and d (referenced below). 108

6.2 Maximum predicted planetary radio fluxes for the rest of the systems presented by Fares et al. (2013). 116

1

Introduction

1.1 Motivation

It has been known since the early 20th century that the Sun possesses a magnetic field (Hale, 1908, 1913; Hale et al., 1918). Many explanations were proposed for the origin of the solar magnetic field but it was not until the seminal work of Parker (1955) that a coherent theory emerged. This study showed that a magnetic field can be sustained by a combination of cyclonic motion, i.e. the α-effect, and differential rotation, i.e. the Ω-effect (see section 1.2 for further details).

After their detection on the Sun, magnetic fields were also detected on chemically peculiar stars (Babcock, 1947) and white dwarfs (Kemp et al., 1970). While the existence of magnetic fields on cool stars other than the Sun had been predicted (e.g. Mullan, 1979), their detection did not occur until 1980 (Robinson et al., 1980). Since this first detection, magnetic fields have been detected in low-mass stars across the Hertzsprung Russell diagram (Donati & Landstreet, 2009; Reiners, 2012; Marsden et al., 2014). Indeed, the majority of low-mass

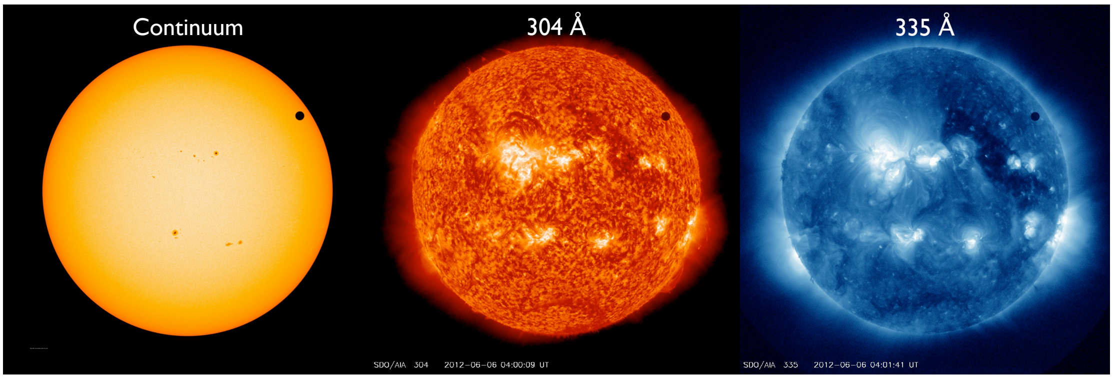
Continuum
304 Å
335 Å
SDO/AIA 304 2012-06-06 04:00:09 UT
SDO/AIA 335 2012-06-06 04:01:41 UT

Figure 1.1: Images of the Sun during the June 2012 Venus transit taken with NASA's Solar Dynamics Observatory. The images are taken in visible light (left), at 304Å (middle) and 355Å (right) corresponding roughly to the photosphere, chromosphere and corona respectively. It is clear that active regions seen in the continuum correspond to magnetic structures seen higher up in the solar atmosphere. Courtesy of NASA/SDO and the AIA, EVE, and HMI science teams

stars with outer convection zones appear to possess organised magnetic fields.

The ubiquity of magnetism in low-mass stars is in contrast to stars with masses larger than $\sim 1.5\,\mathrm{M}_\odot$ where the presence of magnetic fields is much rarer. Studies suggests that only $\sim 8\%$ of O and B stars possess magnetic fields (Grunhut et al., 2011). Since the outer layers of these stars are radiative rather than convective, the dynamo mechanisms responsible for generating magnetic fields on low-mass stars cannot operate. A number of theories have been proposed to explain the fields that have been observed on these stars such as dynamo action in the convective core (e.g. Charbonneau & MacGregor, 2001; Brun et al., 2005), field generation in the outer radiative layers (e.g. Mullan & MacDonald, 2005) or the fields being fossil in origin (e.g. Moss, 2001; Braithwaite & Spruit, 2004).

Stellar magnetism is an important topic to study because of the range of phenomena it is related to. At the photosphere, sun/starspots are caused by the suppression of convective motions by regions of strong magnetic flux (see left image of Fig. 1.1 as well as Borrero & Ichimoto (2011)). Higher up in the stellar atmosphere, magnetic fields are responsible for heating coronae to several million degrees (see middle and right images of Fig. 1.1), though the exact mechanisms involved are not currently clear (De Moortel & Browning, 2015). The magnetic energy deposited in the stellar atmosphere also drives various forms of mass-loss into the surrounding environment. These range from the steady outflowing of charged particles in the form of stellar winds (Wood, 2004) to transient events such as flares (Benz, 2008) and coronal mass ejections (Chen, 2011). The latter two occur on relatively short time-scales of minutes to hours and cause density enhancements to the background wind. On the other hand, magnetic activity cycles, which can be seen in activity tracers such as Ca II H & K lines (Baliunas et al., 1995), occur on longer time-scales of years to decades. At the longest time-scales, stellar rotational evolution is governed by magnetic fields via magnetospheric accretion on the pre-main sequence (Bouvier et al., 2007) and wind driven spin down over the main sequence life time (Weber & Davis, 1967; Mestel, 1968; Skumanich, 1972; Matt et al., 2012; Gallet & Bouvier, 2013; Réville et al., 2015). The influence of a star's magnetic field does not end at its atmosphere either. Further away from the star, stellar winds clear out bubbles in the surrounding interstellar medium and interact with any exoplanets that may be in orbit (e.g. Grießmeier et al., 2007a; Vidotto et al., 2013; Cohen et al., 2015).

It is clear that stellar magnetism is a topic of great import. In this thesis, I will discuss and investigate the magnetic activity of low-mass stars with outer convection zones. The goal is to gain a deeper understanding of their magnetic characteristics and the interactions of their activity with exoplanets. To begin, I will give an overview of stellar magnetism and activity in this introduction. I will split the discussion into five broad areas. These topics are as follows: a) the generation of stellar magnetic fields in section 1.2; b) observing stellar magnetic fields in section 1.3; c) stellar magnetic field properties in section 1.4; d) stellar winds in section 1.5 and e) interactions between exoplanets and their host stars in section 1.6. The ordering of these sections therefore roughly follows stellar activity from its generation inside the stellar interior, through the stellar surface as it emerges through the photosphere and out towards orbiting exoplanets.

1.2 Generating magnetic fields

The time evolution of magnetic fields is governed by the magnetic induction equation,

$$\frac{\partial \mathbf{B}}{\partial t} = \eta \nabla^2 \mathbf{B} + \nabla \times (\mathbf{v} \times \mathbf{B}), \tag{1.1}$$

where $\mathbf{B}$ is the the magnetic field vector, $\mathbf{v}$ is the velocity field vector, t is time and η is the magnetic diffusivity. Equation (1.1) can be derived from Faraday's law, Ampere's law and Ohm's law and describes the behaviour of a magnetic field in an electrically conductive plasma. The first term on the right hand side dominates in high resistivity plasmas and is known as the

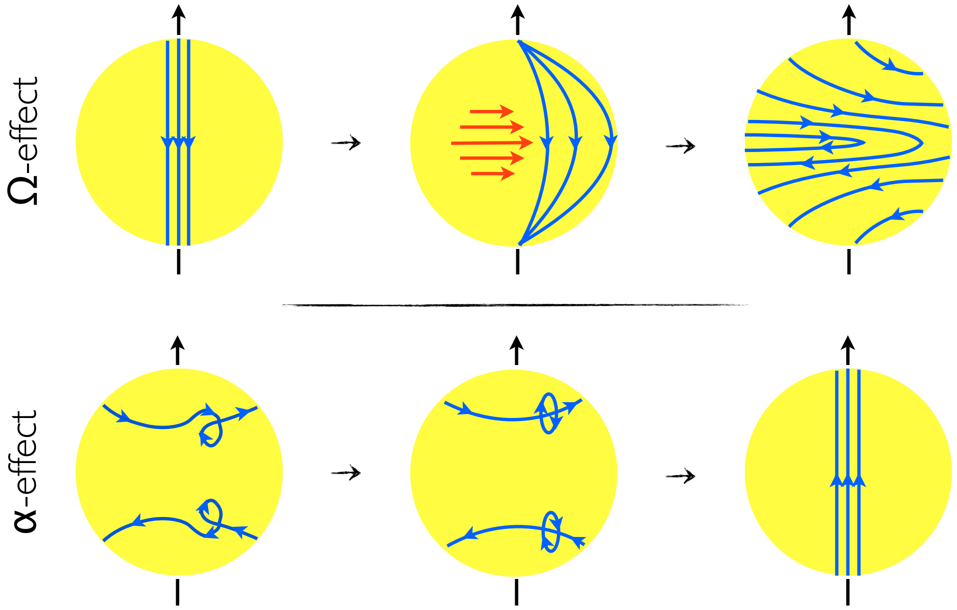

Figure 1.2: Illustrations of the Ω- and α-effects. The Ω-effect (top) winds up an initially poloidal field, via differential rotation, into a toroidal field. As flux tubes buoyantly rise through the convection zone, coriolis forces induces twists in the field lines causing loops to form. This regenerates the poloidal field from the toroidal field, i.e the α-effect (bottom).

diffusion term. In the absence of any field generation mechanisms, this term describes the dissipation of magnetic fields due to resistive decay. The second term is known as the advection term. This term dominates in highly conductive plasmas and describes situations where the magnetic field is carried along, or advected, with the bulk plasma motions.

One way to amplify a magnetic field is by shearing a seed field. Concentrating on the advection term of equation 1.1, positive values of $\frac{\partial \mathbf{B}}{\partial t}$, i.e. growth of the magnetic field, can be achieved if the magnetic field is sheared by plasma motions perpendicular to the magnetic field vector. This is the basic idea behind magnetic field generation on the Sun and other cool stars. Helioseismic studies have revealed that the angular velocity of the Sun varies as a function of depth and latitude (Thompson et al., 2003). This differential rotation provides the shearing required to amplify magnetic fields. In the Sun, it is thought that magnetic field generation occurs predominately at the interface between the inner radiative core and the outer convective layers, known as the tachocline, where the shearing is strongest (Howe et al., 2000). This process of converting poloidal to toroidal field (see section 2.2.2 for the mathematical definitions of poloidal and toroidal fields) is illustrated in Fig. 1.2 and is known as the Ω-effect.

The counterpart of the Ω-effect is the α-effect. Once magnetic fields are sufficiently strong, they become buoyantly unstable and rise to the stellar surface. As they rise through the convective region of the star, Coriolis forces induce twists in the flux tubes generating a poloidal field from the toroidal component (illustrated in Fig. 1.2). The α- and Ω-effects complete a loop whereby poloidal fields can be generated from toroidal fields and vice versa. Together, they describe a class of dynamos known as $\alpha\Omega$-dynamos (Parker, 1955).

While the $\alpha\Omega$-dynamo can operate on stars such as the Sun, it cannot do so in all stars. Stars below the fully convective limit ($M_\star \lesssim 0.35\,\mathrm{M}_\odot$) do not possess a tachocline (Chabrier & Baraffe, 1997) and, consequently, the Ω-effect cannot operate. On such stars, another mechanism must be responsible for generating toroidal fields. In fact, we have already come across such a mechanism. As well as generating poloidal fields, the α-effect can also generate toroidal fields. However, toroidal field generation from the Ω-effect is much more efficient than from the α-effect and so on stars where the former is possible, it will dominate over the latter. Stars where this is not possible must rely on other classes of dynamo, such as α^2-dynamos, in order to maintain their magnetic fields (e.g. Yadav et al., 2015).

1.3 Observing stellar magnetic fields

1.3.1 Absorption lines and the Zeeman effect

A variety of techniques exist to measure and characterise magnetic fields of stellar objects. Fundamental to them is the Zeeman effect. In the presence of a magnetic field, the energy levels of an atom are split resulting in the splitting of the associated spectral line. In order to determine the strength of the splitting, one must consider how the Hamiltonian of the system is perturbed by the magnetic field. It is given by

$$H = H_0 + H_\mathrm{B}, \tag{1.2}$$

where H is the total Hamiltonian of the system, H_0 is the unperturbed Hamiltonian of the atomic system and H_B is the magnetic Hamiltonian. Ignoring the so called ‘diamagnetic term’ that is usually small for cool dwarfs (Donati & Landstreet, 2009), the magnetic Hamiltonian is given by

$$H_{\mathrm{B}} = \mu_0(\mathbf{L} + 2\mathbf{S}) \cdot \mathbf{B}, \tag{1.3}$$

where μ_0 is the Bohr magneton, **L** is the orbital angular momentum operator and **S** is the electron spin operator. Associated with these operators are the orbital angular momentum quantum number, L, and the spin quantum number, S. From quantum mechanical perturbation theory, it is a well known result that the effect of H_{B} is to split the degenerate upper energy level into $2J + 1$ sublevels, where J is the total angular momentum quantum number with an associated operator defined as $\mathbf{J} = \mathbf{L} + \mathbf{S}$. The energy shifts of these sublevels, with respect to the central wavelength, are given by

$$\Delta E = \mu_0 g B M, \tag{1.4}$$

where g is the Landé factor and M is the magnetic quantum number which can take on the values $M = -J, -J+1, ..., J-1, J$. Under the assumption of LS coupling (a reasonable assumption for light atoms), the Landé factor is given by

$$g = 1 + \frac{J(J+1) + S(S+1) - L(L+1)}{2J(J+1)}. \tag{1.5}$$

It turns out that only certain transitions are allowed for any given pair of energy levels. For the electric dipole transition, the selection rule is $\Delta M = -1, 0, +1$. In general, this results in three sets of spectral lines called the π ($\Delta M = 0$), σ_{blue} ($\Delta M = -1$) and σ_{red} ($\Delta M = +1$) components. The π component lies unshifted, at the central wavelength of the spectral line, λ_0, while the σ_{blue} and σ_{red} components are shifted by $\pm\Delta\lambda_{\mathrm{zeeman}}$ (in pm) with respect to λ_0 (in μm), where $\Delta\lambda_{\mathrm{zeeman}}$ is given by

$$\Delta\lambda_{\mathrm{zeeman}} = 4.67\lambda_0^2 \bar{g} B. \tag{1.6}$$

Here, $\bar{g}$ is the effective Landé factor and B is the local magnetic field strength. Figure 1.3 (left) illustrates this splitting.

By measuring the spectral line broadening associated with the Zeeman effect, the strength of the magnetic field can be inferred. However, due to the lack of spatial resolution for stellar objects, only a disc averaged magnetic field strength can be obtained. The reduction of the

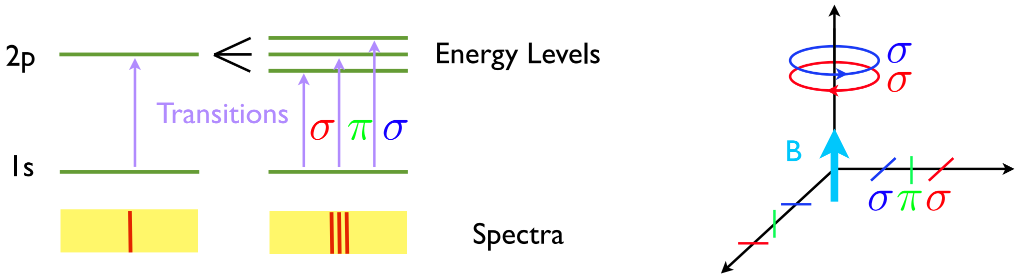

Figure 1.3: Left: a sketch of an energy level diagram for an atom and the associated spectrum. Only a single transition is usually possible. In the presence of a magnetic field however, the upper energy level splits. The corresponding spectrum is broadened into π, $\sigma_{\rm red}$ and $\sigma_{\rm blue}$ components. Right: the polarisation of the π, $\sigma_{\rm red}$ and $\sigma_{\rm blue}$ components as viewed from various orientations with respect to the magnetic field direction. In this example, the magnetic field orientation is in the z direction. When the observer's line of sight is parallel to the magnetic field (in the z direction), no π component is visible and the $\sigma_{\rm red}$ and $\sigma_{\rm blue}$ components are circularly polarised. When the observer's line of sight is perpendicular to the field line (in the x-y plane), all three components are linearly polarised though the π component is at 90 degrees to the other two components. Figure reproduced with permission from Reiners (2012).

field strength and geometry to a single value neglects variations in the field strength across the stellar surface and the field geometry. Additionally, the Zeeman effect competes with other sources of line broadening such as thermal and rotational broadening. The magnitude of these effects are given by $\Delta\lambda_{\rm thermal} \sim \lambda_0\sqrt{k_{\rm B}T/mc^2}$ and $\Delta\lambda_{\rm rot} \sim \lambda_0 v \sin i/c$ respectively, where $k_{\rm B}$ is the Boltzmann constant, T is the effective temperature, m is the average particle mass, v is the equatorial velocity and i is the stellar inclination. If the magnetic field is weak, the splitting in the spectral lines may not be large enough to be resolved in wavelength space resulting in no field detection at all. However, despite the drawbacks inherent in this technique, it is at least capable of providing a measure of the stellar magnetic field strength for stars with a sufficiently strong field.

1.3.2 Spectropolarimetry

Some of the deficiencies described in section 1.3.1 can be overcome by simultaneously observing the spectra and polarisation of the radiation from a star, i.e. spectropolarimetry. Each of the Zeeman components, π, $\sigma_{\rm blue}$ and $\sigma_{\rm red}$, show different polarisation states. Physically, the π component corresponds to an oscillation of the dipole moment along the magnetic field vector. The resulting radiation is linearly polarised with respect to the magnetic field vector. However, the radiation associated with the σ_{blue} and σ_{red} spectral lines are right- and left-circularly polarised with respect to the local magnetic field line. In this case, the dipole moment oscillation contains two components. These components are perpendicular to each other as well as to the local magnetic field vector. They are also out of phase by $\pi/2$ resulting in the circular polarisation.

Due to these different magnetic moment oscillations, the polarisation signature an observer detects is dependent on the orientation of the local field line with respect to the observer. When the line of sight is parallel to the field line, i.e. along the z axis in Fig. 1.3, the π component vanishes while the σ components appear circularly polarised. When the line of sight is transverse to the field line, i.e. in the x-y plane in Fig. 1.3, both the π component and the σ components are linearly polarised from the point of view of the observer (though at right angles to each other). Spectropolarimetry makes use of both spectral and polarisation information to recover information about the strength and geometry of stellar magnetic fields. The polarisation state is commonly described using Stokes vector notation, $[I, Q, U, V]$, where I is the unpolarised component of the radiation, Q and U are the linearly polarised components (with the U component orientated at 45° to the Q component) and V is the circularly polarised component. A visual representation of the Stokes vector is shown in Figure 1.4.

Most spectropolarimetric observations, in the context of stellar magnetism, are made with either ESPaDOnS, NARVAL or HARPSpol. These are spectropolarimeters mounted on the Canada-France-Hawaii Telescope, the Bernard Lyot Telescope and the 3.6m telescope at La Silla Observatory respectively. Spectropolarimeters can be broken down into a spectroscopic part and a polarimetric part. Polarimeters typically contain two main optical components, a set of waveplates and a beam splitter. Waveplates are made of birefringent materials which have different refractive indices for different polarisations of light. The most common types are the half-wave plate which can change the polarisation direction of linearly polarised light and the quarter-wave plate which can convert linearly polarised light into circularly polarised light and vice versa. A beam splitter, such as a Wollaston prism, is then used to separate the light into two beams with orthogonal polarisation states. The beams are then sent to the spectrograph where a diffraction grating will disperse the light into a wavelength spectrum.

One common method of using the polarisation data is to determine the longitudinal magnetic field averaged over the visible surface (e.g. Marsden et al., 2014; Jeffers et al., 2014;

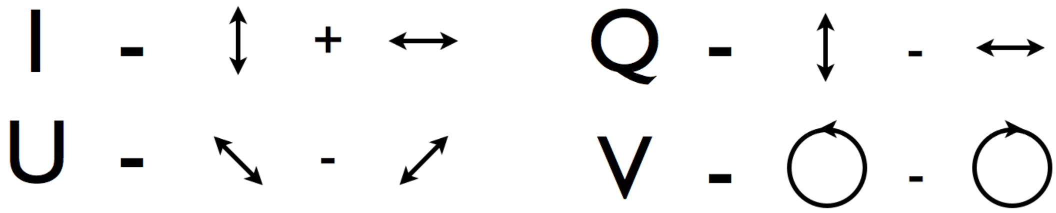

Figure 1.4: The filters required to measure each polarisation state in the Stokes vector. The four components of the Stokes vector are I - unpolarised light, Q - linearly polarised light, U - linearly polarised light (at 45° to Q) and V - circularly polarised light.

Boro Saikia et al., 2015). Donati et al. (1997) showed that this can be calculated from the Stokes vector:

$$B_\ell = -714 \frac{\int vV(v)\,dv}{\lambda_0 \bar{g} \int [1 - I(v)]\,dv} \tag{1.7}$$

where v is the velocity shift in $\mathrm{km\,s^{-1}}$ with respect to the central wavelength of the spectral line, λ_0, and $\bar{g}$ is the average Landau factor. Although B_ℓ characterises part of the field geometry, it is still a disc averaged quantity and does not capture the transverse component of the field.

1.3.3 Zeeman-Doppler imaging

To characterise the magnetic field geometry over the entire stellar surface, a technique known as Zeeman-Doppler imaging (ZDI) can be employed. It was first proposed by Semel (1989) and subsequently implemented by Brown et al. (1991) and Donati & Brown (1997a). To reconstruct a magnetic map, many measurements of the circularly polarised light (Stokes V) and spectra from a star are required, over the course of, at least, one stellar rotation period. It is worth noting that the magnitude of the polarisation in Stokes Q and Stokes U is typically much smaller than Stokes V which is why often only Stokes I and Stokes V are used. However, in some cases information from stokes Q and U can also be retrieved (Rosén et al., 2015). As a magnetic feature rotates across the visible hemisphere of the star, the amount of circularly polarised light we observe changes. This occurs because the longitudinal component of the magnetic field is modulated by the stellar rotation. ZDI retrieves the field geometry information from the polarisation data and hence, can reconstruct the surface magnetic field. In reality, the problem is degenerate with a large number of possible solutions for a given set of Zeeman signatures. To lift this degeneracy, the solution that minimises the energy in the magnetic field is chosen.

One of the problems associated with ZDI is its inability to resolve small-scale structure in the magnetic field. Flux cancellation within a resolution element means that only the large scale components of the field can be reconstructed. In general, the spatial resolution that can be attained is related to the rotational velocity of the star (Morin et al., 2010; Fares et al., 2012) and is roughly given by

$$l_{\rm max} \simeq \max\left(\frac{2\pi v \sin i}{\rm FWHM}; l_{\rm min}\right). \tag{1.8}$$

Here $l_{\rm max}$ is the highest order spherical harmonic mode (see section 2.1 for further discussion on spherical harmonic modes) that can be reconstructed, v is the equatorial velocity, i is the stellar inclination, FWHM is the full width half max of the intrinsic line profile, i.e. in the inertial frame of the star, and $l_{\rm min}$ is the minimum harmonic mode that can be reconstructed (usually $l = 4$). Typically, $l_{\rm max}$ values of 5-10 are possible although values as high as $l_{\rm max} = 25$ have been achieved for some of the most rapid rotators, e.g. AB Dor. Even though ZDI cannot resolve small-scale structure, its ability to spatially resolve the large-scale field structure means it is a large step forward in the mapping of stellar magnetic fields when compared with previous techniques.

1.4 Properties of stellar magnetic fields

Over the last decade and a half, ZDI has vastly improved our understanding of stellar magnetic fields. To date, over ∼100 stars have had their fields mapped with this technique. Although a great deal can be learnt about individual stars by studying the full magnetic map, when studying samples of stars, it is much more useful to reduce a magnetic map to a set of global characteristics. The main properties discussed in the literature are the magnetic field energy density averaged over the stellar surface, the poloidal/toroidal energy fraction and the field axisymmetry. Mathematical definitions of these properties can be found in section 2.2.2. As more stars have had their fields mapped, trends in stellar magnetism, as a function of fundamental stellar properties, have emerged and been identified.

Many of the trends in stellar magnetism are encapsulated by Fig 1.5 which has been reproduced from Donati & Landstreet (2009). This figure shows the magnetic field properties of a large number of stars that have had their surface fields mapped with ZDI plotted in stellar

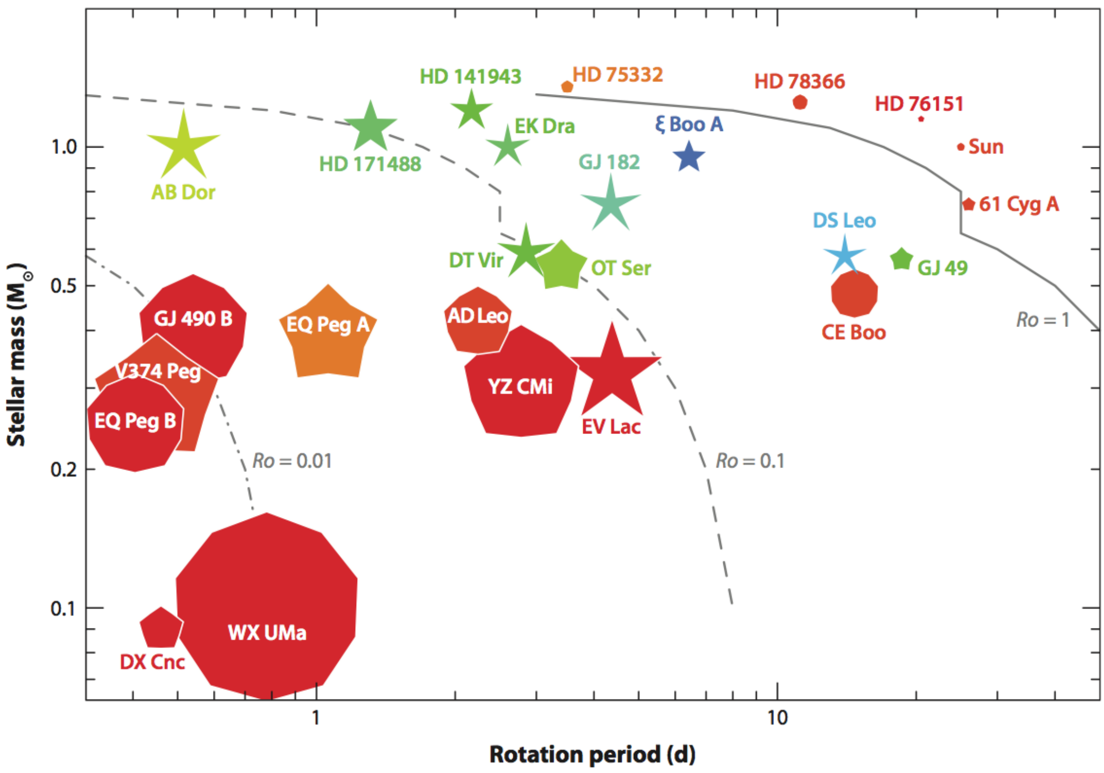

Figure 1.5: A sample of stars with ZDI maps plotted in mass - rotation period space. The size of each point corresponds to the average magnetic field energy density at the surface of the star, red/blue symbols correspond to stars that are strongly poloidal/toroidal and regular polygons/star shapes correspond to stars that have axisymmetric/non-axisymmetric fields. Mathematical definitions of these quantities can be found in section 2.2.2. Figure reproduced from Donati & Landstreet (2009) with permission.

mass - rotation period space. The average magnetic energy density, poloidal energy fraction and poloidal axisymmetric energy fraction of a star are represented by the symbol size, colour and shape respectively. Larger symbols indicate stronger magnetic fields, redder/bluer symbols indicate more poloidal/toroidal fields and polygons/star shapes indicate more/less axisymmetric fields. I will discuss some of the key results in the following paragraphs.

1.4.1 Effect of stellar mass

Stellar mass is one of the fundamental parameters of a star. In the context of stellar magnetism, the mass is important because it determines the internal structure of the star (Baraffe et al., 1998), and therefore the dynamo mechanisms that are able to operate. On the Sun, it is thought that magnetic fields are primarily generated in a thin layer between the radiative core and outer convective zone, known as the tachocline, where shearing is strongest (Charbon-

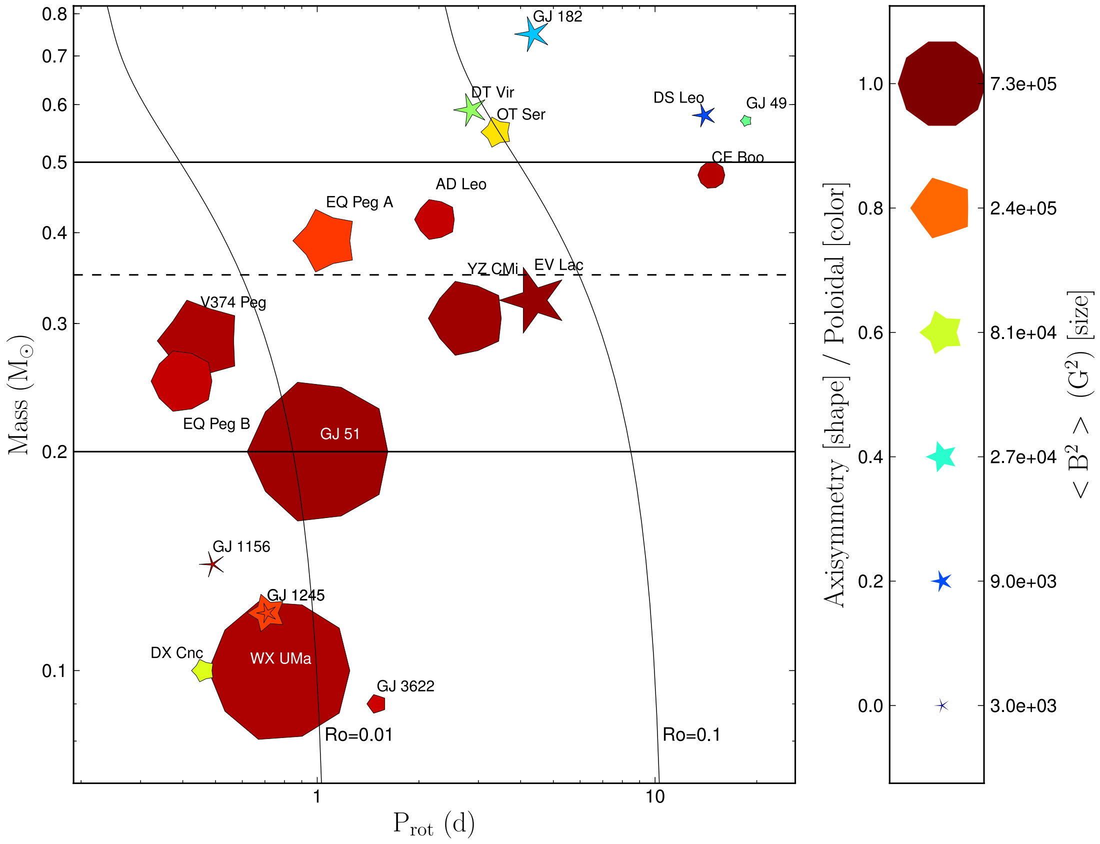

Figure 1.6: The magnetic characteristics of a sample of M dwarfs. The format is the same as Fig. 1.5. Above 0.5 M$_\odot$, stars show weak, non-axisymmetric fields and below this mass, stars show strong, poloidal and axisymmetric fields. Below 0.2 M$_\odot$, stars with both types of field coexist in a relatively small region of parameter space. Figure reproduced from Morin et al. (2010) with permission.

neau, 2010). On the other hand, low mass stars below the fully convective limit ($\lesssim 0.35\,\rm M_\odot$) cannot possess a tachocline due to the absence of a radiative core (Chabrier & Baraffe, 1997). However, both theoretical (e.g. Küker & Rüdiger, 1999; Chabrier & Küker, 2006) and observational studies (e.g. Morin et al., 2008a) have shown that these stars are able to sustain strong magnetic fields. Different dynamo mechanisms must therefore be present. Donati et al. (2008a), Morin et al. (2008b) and Morin et al. (2010) investigated the dependence of magnetic properties on stellar mass by imaging the magnetic fields of a set of stars that straddles the fully convective limit. These authors found a strong break in magnetic properties at $\rm M = 0.5\,M_\odot$ with the more massive stars displaying weak, non-axisymmetric, toroidal fields and the less massive ones displaying strong, axisymmetric, poloidal fields (see Fig. 1.6). Given that the mass at which the break occurs roughly coincides with the fully convective limit, the authors argue that it occurs as a result of the internal structure changes.

Unexpectedly, below $\mathrm{M} < 0.2\,\mathrm{M}_\odot$, stars begin to display weak non-axisymmetric fields again. Such stars coexist in this relatively small region of parameter space with stars with strong, axisymmetric, dipolar fields (Morin et al., 2010). This suggests that the magnetic fields of $\mathrm{M} < 0.2\,\mathrm{M}_\odot$ stars are bi-stable. The reason for such a bi-stability is unclear though numerical simulations suggest that it can be attributed to a Rossby number threshold (Gastine et al., 2013).

1.4.2 Effect of rotation period

It has long been known that the rotation period, P_{rot}, is an important parameter in the context of magnetic activity. Many studies have shown that various activity proxies increase in strength with faster rotation, and that saturation occurs for the fastest rotators (Vilhu, 1984; Noyes et al., 1984; Pizzolato et al., 2003; Mamajek & Hillenbrand, 2008; Wright et al., 2011). These results also hold true when we consider the large-scale magnetic fields reconstructed from ZDI. Petit et al. (2008) showed that, in solar mass stars, surface field strengths increase with increasing rotation (see Fig. 1.7). These authors also found that the poloidal energy fraction decreases with increasing rotation.

While the rotation period is important, there is evidence that the Rossby number (the rotation period normalised to the convective turnover time, i.e. $\mathrm{Ro} = \mathrm{P}_{\mathrm{rot}}/\tau_{\mathrm{c}}$) is the more fundamental parameter in the context of magnetic activity. Theoretically, it can be shown that the dynamo number, a measure of the effectiveness of field generation, has a inverse square dependence on the Rossby number, i.e. $N_{\mathrm{D}} \sim \mathrm{Ro}^{-2}$ (Noyes et al., 1984). Observationally, magnetic proxies show less scatter when plotted against Rossby number compared to rotation period. The most obvious example of this is the activity-rotation relation (Wright et al., 2011) where the ratio of X-ray to bolometric luminosity of stars, $R_{\mathrm{X}} = L_{\mathrm{X}}/L_{\mathrm{bol}}$, is shown to increase with decreasing Ro until $\mathrm{Ro} \sim 0.1$. Below this Rossby number, R_{X} saturates. There is no consensus on the reason for such a saturation though common explanations include saturation of the dynamo mechanism (Vilhu, 1984), saturation of the stellar surface preventing further flux from emerging (Vilhu, 1984) or centrifugal stripping of the corona (Jardine & Unruh, 1999). Vidotto et al. (2014) found that large-scale surface magnetic field strengths obtained from ZDI also follow the shape of the activity-rotation relation indicating a fundamental link between magnetic fields and X-ray emission. In chapter 3, I will present further and original

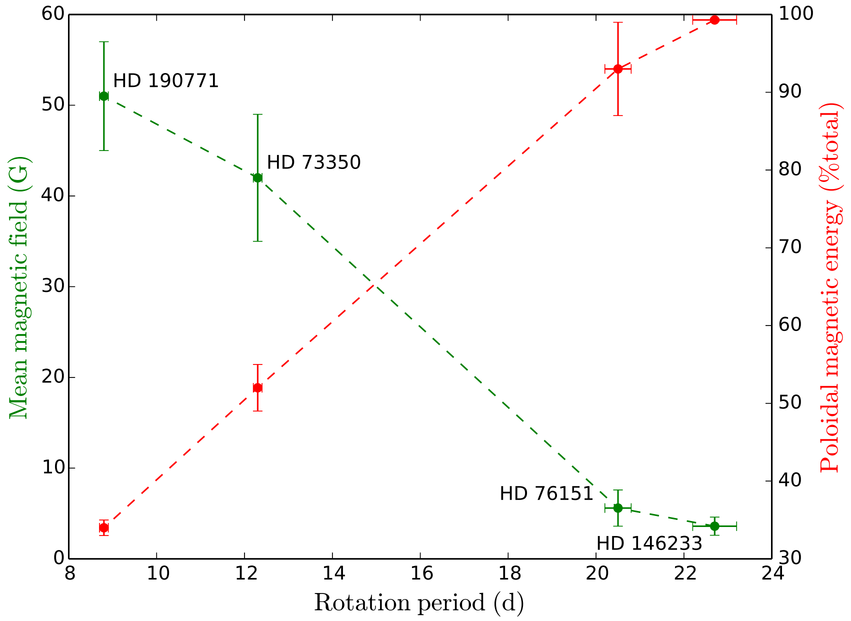

Figure 1.7: Average surface magnetic field strength (green) and percentage of fields that are poloidal (red) vs rotation rate for a sample of four solar mass stars. Figure reproduced with permission from Petit et al. (2008).

work relating to the magnetic characteristics of low mass stars.

1.4.3 Magnetic cycles

In addition to studying the magnetic fields of stars at one particular snap shot in time, it is also possible to study their temporal evolution via repeated ZDI mapping over multiple epochs. These types of studies have shown that the surface magnetic fields can evolve significantly over the time-scale of years (e.g. Catala et al., 2007; Donati et al., 2008b; Fares et al., 2009, 2013; Jeffers et al., 2014; Boro Saikia et al., 2015). However, in some cases, the surface fields show very little evolution (e.g. Morin et al., 2008a). In this latter case, this is likely due to the small magnitude of differential rotation of the star in question.

One type of temporal evolution seen is a reversal of the global polarity of the large-scale magnetic field (Donati et al., 2003b, 2008b; Fares et al., 2009; Petit et al., 2009; Morgenthaler et al., 2011; Fares et al., 2013). On the Sun, the polarity of the global field switches roughly every 11 years (e.g. DeRosa et al., 2012) and is one observable sign of the solar activity cycle. Fundamentally, this cycle occurs as a result of dynamo processes. Over the course of a cycle, an α-effect, e.g. cyclonic convection, generates a poloidal field from a toroidal one and an Ω-

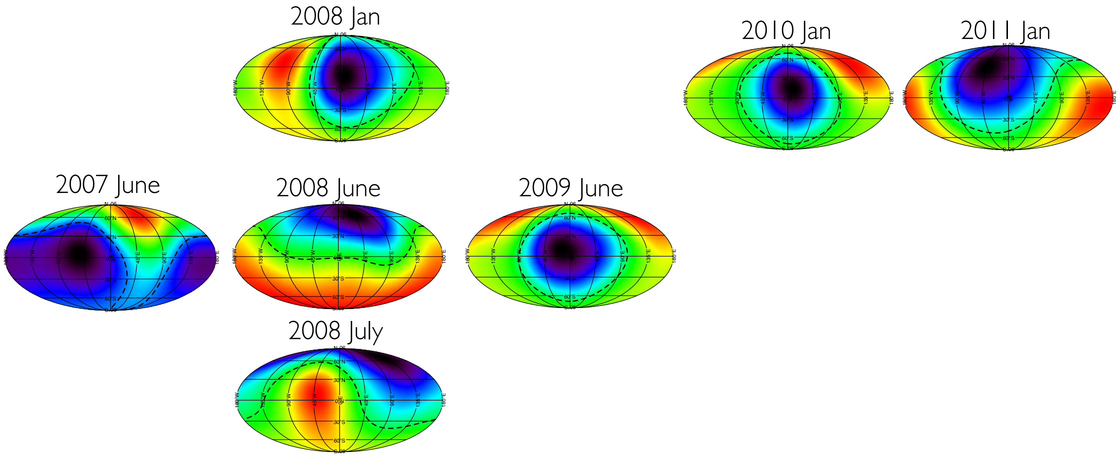

Figure 1.8: Magnetic field maps at the source surface (the limit of coronal confinement, see section 2.2.3) of τ Boo during seven different epochs. Maps are organised by year from left to right and by month from top to bottom. Global polarity switches occur with a $\sim$ 1 year period and can be most easily seen in the 2007 June → 2008 June → 2009 June maps and the 2010 January → 2011 January maps. The field extrapolations required to construct these source surface maps can be found in See et al. (2015a) using data from Donati et al. (2008b), Fares et al. (2009) & Fares et al. (2013).

effect, e.g. differential rotation, generates a toroidal field from a poloidal one (Charbonneau, 2010).

With regards to stellar magnetic cycles, the most well studied star is τ Boo, a rapidly rotating F7 dwarf star. Numerous authors have studied this star observing multiple polarity reversals which can be seen in Fig. 1.8 (Donati et al., 2008b; Fares et al., 2009, 2013). They determined that the most likely period of its polarity switches is either 8 months or 2 years. Curiously, this value is much shorter than the 11 year period of the Sun. However, given that the differential rotation of τ Boo is nearly an order of magnitude stronger than the Sun's, such a short period may not be as surprising as it first seems. Indeed a 2 year period is consistent if the cycle period scales roughly linearly with the strength of differential rotation (Donati et al., 2008b). In chapter 4, I will present new insights into stellar activity cycles by studying the large-scale magnetic fields of stars with known activity cycle periods.

1.5 Solar and stellar winds

1.5.1 Early models

The idea of a solar wind was first proposed by Biermann (1951) based on the observation that comet tails always point radially away from the Sun. The first formal investigation of this idea was conducted by Parker (1958) who called it the solar wind. In this paper, the author presents the first model of a wind by considering the consequences of having a several million degree corona. He found that this should, indeed, result in a significant outgassing from the Sun as a result of the large pressure gradient between the Sun and the interstellar medium. Even though the model is based on highly idealised assumptions (steady, isotropic and isothermal flows, a non-rotating star and neglecting magnetic fields), it has proven to be an extremely important piece of work and is still in regular use (e.g. Grießmeier et al., 2007a). Many authors have since modelled the solar wind, taking into account properties that Parker initially neglected. The wind model of Weber & Davis (1967) considered a rotating Sun with a magnetised wind, with Sakurai (1985) extending the 1D models of Weber & Davis (1967) to 2 dimensions.

1.5.2 Determining stellar wind properties

Measuring the properties of solar and stellar winds from Earth based facilities is extremely difficult due to the their sparse nature. For example, the Sun has a mass-loss rate of $\sim 10^{-14} M_{\odot}\mathrm{yr}^{-1}$ (Cranmer & Saar, 2011) resulting in a wind number density of only $5\mathrm{cm}^{-3}$ in the vicinity of Earth (Balikhin et al., 1993). In the solar case, we can overcome this difficulty by making in-situ measurements with satellites (e.g. Ebert et al., 2009) allowing us to determine properties such as wind, speed, density, temperature and magnetic field strength, as well as the overall mass-loss rate. However, such a strategy is clearly not possible for the winds emanating from other stars. Consequently, the majority of studies involving stellar winds are theoretical by necessity.

While direct measurement of stellar wind properties is not currently possible, an indirect determination of the global mass-loss rate of a star can be achieved via astrospheric Lyα absorption observations (see Wood et al. (2014) and references therein for full details). At the boundary of a star's astrosphere (the stellar equivalent of the heliosphere), its wind collides with the interstellar medium. Neutral hydrogen from the interstellar medium is heated up at

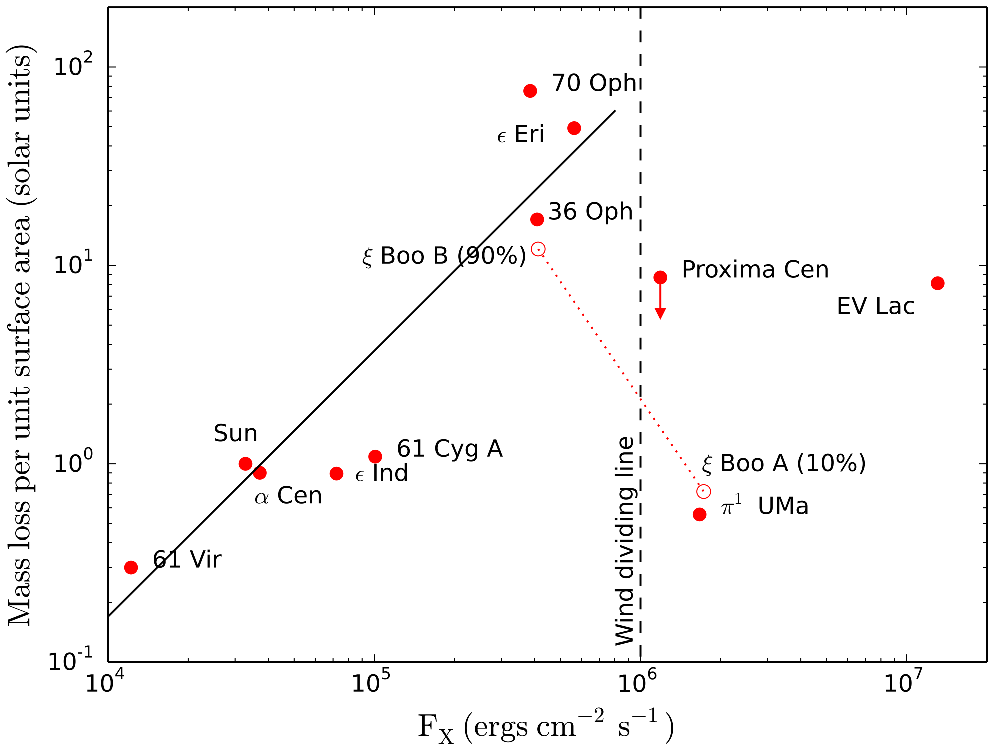

Figure 1.9: Mass-loss rates vs X-ray surface flux. Below the wind dividing line, $F_X \sim 10^6$ ergs cm^{-2} s^{-1}, the mass-loss rates are correlated with X-ray emission. However, this correlation breaks down for high activity stars. Figure reproduced with permission from Wood et al. (2014).

this interaction region. As light from the star passes through this population of hot hydrogen, the Lyα line is absorbed and by analysing the exact shape of the line profile, an estimate of the wind properties can be made.

Over the last decade, the mass-loss rates of roughly 10 stars have been estimated using this technique. Wood et al. (2014) found that below a surface X-ray flux of $F_X = 10^6$ ergs cm^{-2} s^{-1}, the mass-loss rate correlates well with X-ray emission (see Fig. 1.9). Above this value, which these authors call the wind dividing line, they find that mass-loss rates drop off sharply. The authors cite a change in magnetic field topology as a possible explanation for this reduced mass-loss rate. For example, the formation of polar starspots can be found in high activity stars (Schrijver & Title, 2001; Strassmeier, 2002) and may act to inhibit mass-loss. However, when studying the ZDI maps of a sample of stars with mass-loss estimates, Vidotto et al. (2016) does not find any systematic change in large-scale topology when crossing the wind dividing line. It is worth bearing in mind that the idea of a wind dividing line is based on a relatively small set of data points and may prove to be incorrect when additional data points are obtained.

1.5.3 Modern wind models and simulations

Modern efforts at modelling stellar winds are much improved compared with the earliest models. These improvements have chiefly occurred for two reasons. Firstly, our understanding of the mechanisms by which the winds are accelerated has progressed allowing for the construction of more physically motivated models. Early models simply admitted free parameters in the form of a wind temperature or a polytropic parameter (Keppens & Goedbloed, 1999), with values chosen such that results matched observations of the solar wind as closely as possible. This sort of approach folds our ignorance of the heating mechanisms into the free parameters and makes little attempt to identify the actual source of heating. Since then, wave heating has emerged as a leading candidate as a mechanism by which winds can be accelerated (e.g. Musielak & Ulmschneider, 2002). This is the idea that Alfvén waves will be driven upwards into the corona by convective motions below the stellar surface. Energy from these waves can then drive a stellar wind. Cranmer et al. (2007) conducted an extensive study on wave heating, concluding that wave heating can be used to explain the amount of heating in the solar wind. Following on from this work, Cranmer & Saar (2011) predicted the mass-loss rate of cool stars with better agreement to observations than the models of Reimers (1975, 1977) and Schröder & Cuntz (2005) which are based on scaling relations.

The second reason for advances in stellar wind modelling is the increase in computing power. With the advent of high performance computing, it is now possible to conduct multi-dimensional MHD simulations where the fluids and fields interact self-consistently. These types of simulations have been used to explore the parameters that are important in the context of stellar spin down as a result of stellar winds (Matt et al., 2012; Réville et al., 2015) allowing for the study of the rotational evolution of cool dwarf stars (Gallet & Bouvier, 2013, 2015). Perhaps the most realistic wind simulations are those that incorporate ZDI maps to constrain the magnetic field structure (e.g. Vidotto et al., 2009, 2011, see Fig. 1.10 for an example of such a simulation) rather than using idealised field modes, i.e. dipole, quadrupole, etc. While these simulations incorporate the most physics, they pay a corresponding price in terms of computational time. As a result, many authors still make use of static field extrapolations/wind models, such as the potential field source surface model (Jardine et al., 2002;

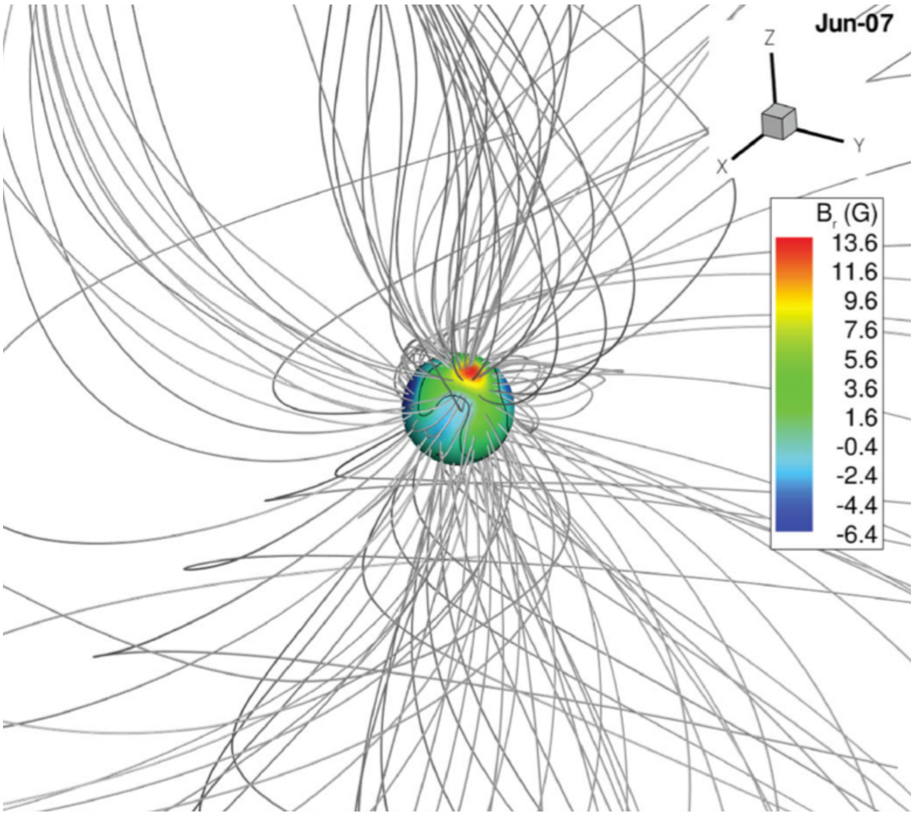

Figure 1.10: The 3D magnetic topology of τ Boo. This obtained from a 3D, self consistent simulation that uses a ZDI map as an inner boundary condition. Figure reproduced with permission from Vidotto et al. (2012).

Fares et al., 2010). While not self-consistent, these models do allow a rapid assessment of the gross details of a stellar system. Increasingly, simulations of the self-consistent and non self-consistent kind are being used to investigate the impact that the host stars have orbiting exoplanets (Fares et al., 2012; Vidotto et al., 2013; Cohen et al., 2015).

1.6 Exoplanets and their host stars

1.6.1 Searching for exoplanets

The search for planets around stars other than our own Sun has been ongoing for two decades (Mayor & Queloz, 1995; Marcy & Butler, 1996; Butler & Marcy, 1996) with over 1500 exoplanets found to date and over another 3500 candidates. Many techniques are utilised to search for planets around stars other than our own Sun with the transit and radial velocity methods proving to be the most successful. The transit method detects the characteristic periodic dip in the light curve of the host star when an exoplanet passes directly between it

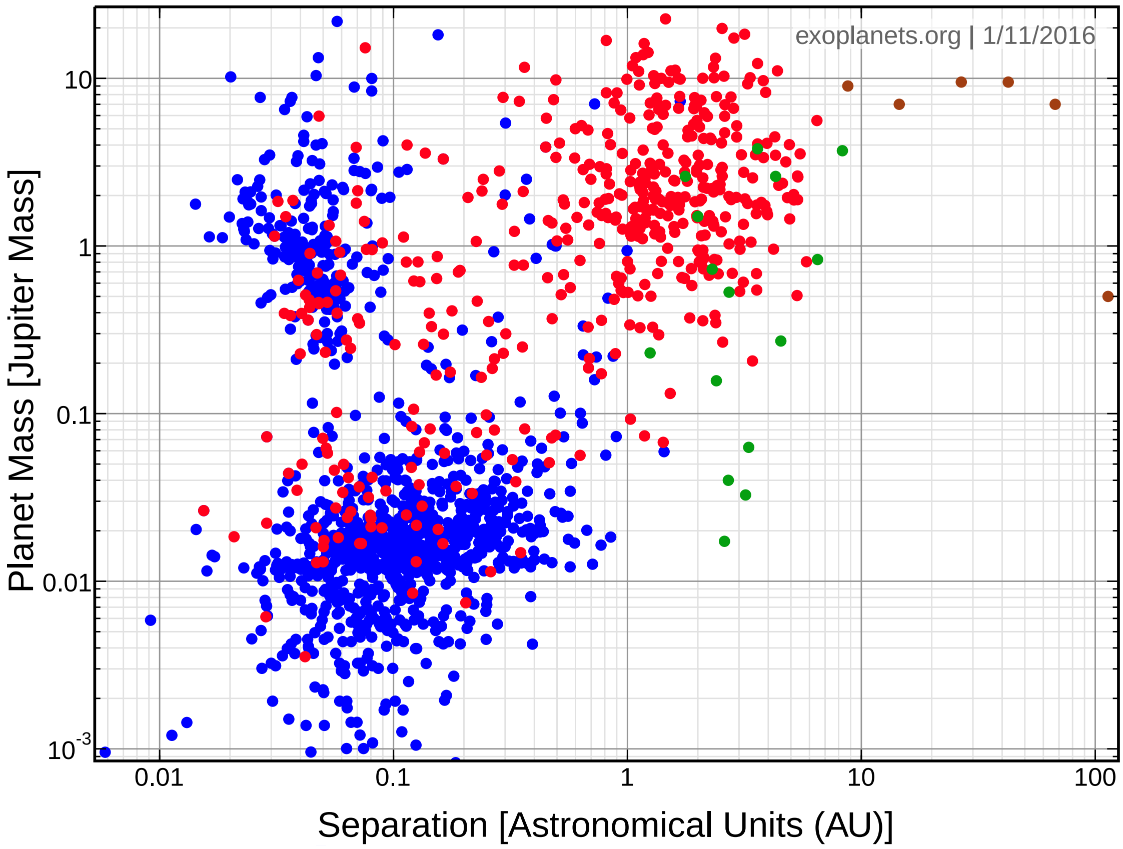

Figure 1.11: Mass vs separation from host star for all confirmed exoplanets as of 11th January 2016. The colour for each point represents the methods used to discover the exoplanet - blue, red, green and brown for the transit, radial velocity, microlensing and direct imaging techniques respectively. This plot was made using the publicly available tools at exoplanets.org/plots.

and observers on Earth. The radial velocity method relies on the wobble induced in the host star by an orbiting exoplanet causing them both to circle around their mutual center of mass. This wobble can cause detectable periodic Doppler shifts in the spectral lines of the stellar spectrum.

Due to the nature of these techniques, they have an intrinsic measurement bias. The transit method is much more likely to detect planets orbiting close to low luminosity stars since, for a given size of planet, the dip in the light curve will be wider & deeper and will occur more frequently. The radial velocity method is biased towards detecting more massive planets which will induce a larger wobble in their host star. These biases are clearly visible in Fig. 1.11 which shows that a majority of exoplanets detected by these methods are either close in, massive or both. Due to their proximity to their host star, the surface temperatures of these planets can be extremely high. Appropriately these planets have been called hot

Jupiters.

Although numerous hot Jupiters have been found, the goal has always been to find small and rocky planets with the hopes of eventually finding one of Earth mass that may be habitable. For the smallest planets, the planetary radial velocity signal is comparable to, or smaller than, the signals induced by stellar activity known as activity jitter (Barnes et al., 2011). Detecting these planets is therefore a significant task that involves disentangling the planetary and stellar signals. Various attempts have been made to do this from modelling the stellar activity as a Gaussian process (Haywood et al., 2014) to using information minimisation techniques (Donati et al., 2015) to determine the presence of a planet. These techniques highlight the importance of understanding stellar activity in the search for an Earth analogue.

1.6.2 Exoplanet characterisation from wind interactions

While the discovery of exoplanets is interesting and rewarding in and of itself, there are now significant efforts being made to characterise the properties of the vast number of exoplanets that have been discovered. For example, some topics that have received attention are the internal composition of exoplanets (e.g. Howard et al., 2013), their cloud structures (e.g. Lee et al., 2015) and their magnetospheric properties (Llama et al., 2013; Vidotto et al., 2010). This is, of course, only a flavour of the type of work being undertaken in the ongoing task of exoplanet characterisation.

In the previous section, I discussed the importance of characterising stellar activity when searching for exoplanets. However, understanding stellar activity is also important when it comes to characterising the properties of a planet and its surrounding environment. In particular, driven by knowledge from our own solar system, there has been significant work looking at how stellar winds interact with exoplanetary magnetospheres and atmospheres. The magnetised solar system planets (Earth, Jupiter, Saturn & Uranus) show significant non-thermal auroral emissions (e.g. Zarka, 1998) as a result of the solar wind being funneled into their auroral caps. It is thought that similar auroral emissions may be detectable from hot Jupiters (e.g. Zarka, 2007, see section chapter 6 for further discussion of exoplanetary radio emission). On the other hand Mars and Venus do not possess an intrinsic magnetic field. As a result, these planets suffer strong atmospheric mass loss (Edberg et al., 2010, 2011) since they lack any protection from the erosive effects of the solar wind. This highlights the impact that stellar activity can have on the habitability of a planet (see chapter 5 for further discussion on exoplanetary habitability).

1.7 Thesis outline

In this introduction, I have discussed a number of topics relating to the observation and our theoretical understanding of stellar magnetism and activity. This discussion has followed stellar activity from the stellar interior, through the stellar surface and out to orbiting exoplanets. The rest of this thesis will follow roughly the same structure as the introduction.

In chapter 2, I cover the mathematics required to describe stellar magnetic fields. In particular I present the equations used to represent the magnetic field maps derived from ZDI as well as 3D field extrapolation techniques.

In chapter 3, I expand on the discussion from section 1.4. I analyse the magnetic properties of a large sample of stars as a function of mass and rotation. I pay particular attention to their toroidal components to learn about the mechanisms by which they are generated and to constrain future dynamo models.

In chapter 4, I analyse a subset of the sample of ZDI maps used in chapter 3 focusing on stars that have activity cycle period determinations in the literature. I investigate the magnetic properties of stars on the so called active and inactive branches and present new insights on stellar activity cycles.

In chapter 5, I discuss the likely conditions required for an exoplanet to be habitable. In particular, I focus on the influence that host stars can have on habitability. Using a thermal wind model, I investigate the ability of magnetospheres to protect planetary atmospheres from the erosive effects of stellar winds.

In chapter 6, I investigate exoplanetary radio emissions. This is achieved using the ZDI maps of several stars known to be exoplanet hosts and 3D field extrapolation techniques. I show that it is possible to learn about the structure of the host star's magnetic field from the radio emission characteristics of the exoplanet.

In chapter 7, I present my concluding remarks for this thesis. Additionally, I present a brief discussion about the future prospects of the field of stellar magnetism and activity.

2

Field Modelling

In chapter 1, I discussed a variety of techniques used to observe and model stellar magnetic fields. Particularly important for this thesis are Zeeman-Doppler imaging (ZDI) and the potential field source surface (PFSS) model. ZDI is the use of spectropolarimetric observations to map the large-scale magnetic field of the stellar surface while the PFSS model is a 3D field extrapolation technique. In this chapter, I outline the mathematical framework that forms the basis of these techniques.

2.1 Spherical Harmonics

If a magnetic field is in a potential state, i.e. no currents, then Ampere's law is written as

$$\nabla \times \mathbf{B} = 0 \tag{2.1}$$

Since the identity, $\nabla \times (\nabla \Psi) = 0$, is true for any scalar field, Ψ, the magnetic field can be written as

$$\mathbf{B} = \text{-}\nabla \Psi, \tag{2.2}$$

where $\Psi(r, \theta, \phi)$ is a 3D scalar potential field. By substituting **B** into Gauss' law for magnetism, $\nabla \cdot \mathbf{B} = 0$, Laplace's equation, $\nabla^2 \Psi = 0$, can be obtained. The solution to Laplace's equation has a standard derivation that is available in many textbooks. I reproduce its derivation here for completeness.

In spherical coordinates, Laplace's equation is given by

$$\frac{1}{r^2}\frac{\partial}{\partial r}\left(r^2\frac{\partial \Psi}{\partial r}\right) + \frac{1}{r^2 \sin\theta}\frac{\partial}{\partial \theta}\left(\sin\theta\frac{\partial \Psi}{\partial \theta}\right) + \frac{1}{r^2 \sin^2\theta}\frac{\partial^2 \Psi}{\partial \phi^2} = 0. \tag{2.3}$$

It will be convenient to adopt a separable solution to this equation of the form

$$\Psi(r, \theta, \phi) = R(r)\Theta(\theta)\Phi(\phi). \tag{2.4}$$

Substituting this trial solution into equation (2.3), and performing some algebraic manipulations, one obtains

$$\left(\sin^2\theta\frac{r^2}{R}\frac{d^2R}{dr^2} + 2\sin^2\theta\frac{r}{R}\frac{dR}{dr}\right) + \left(\frac{\sin^2\theta}{\Theta}\frac{d^2\Theta}{d\theta^2} + \frac{\cos\theta\sin\theta}{\Theta}\frac{d\Theta}{d\theta}\right) + \frac{1}{\Phi}\frac{d^2\Phi}{d\phi^2} = 0. \tag{2.5}$$

Equation (2.5) must hold for all values of r, θ and ϕ. Additionally, the final term is a function of ϕ only. To satisfy both of these conditions, this term must be a constant. This constant is chosen to be $-m^2$ such that

$$\frac{d^2\Phi}{d\phi^2} = -m^2\Phi. \tag{2.6}$$

The solution to this is

$$\Phi = Ae^{im\phi}, \tag{2.7}$$

where A is a constant. By rotational symmetry arguments, the function, Φ, must be unchanged under a 2π rotation, i.e., $\Phi(\phi) = \Phi(\phi + 2\pi)$. This condition restricts m to integer values only.

Substituting equation (2.7) into equation (2.5) and dividing through by $\sin^2\theta$, one obtains

$$\left(\frac{r^2}{\mathrm{R}}\frac{d^2R}{dr^2} + \frac{2r}{R}\frac{dR}{dr}\right) + \frac{1}{\sin^2\theta}\left(\frac{\sin^2\theta}{\Theta}\frac{d^2\Theta}{d\theta^2} + \frac{\cos\theta\sin\theta}{\Theta}\frac{d\Theta}{d\theta} - m^2\right) = 0. \tag{2.8}$$

The terms in the first set of brackets are a function of r only. Using the same arguments used to solve for the function $\Phi(\phi)$, these terms must also be equal to a constant. This constant is chosen to be $l(l+1)$ such that

$$r^2\frac{d^2R}{dr^2}+2r\frac{dR}{dr}=l(l+1)R. \tag{2.9}$$

The solution to equation (2.9) turns out to be a trial series solution of the form $R=\sum_{n=0}^{\infty}a_n r^n$. In order for this solution to be valid for all r, only the $n=l$ and $n=-(l+1)$ terms are valid and so the solution for $R(r)$ takes the form of

$$R=Br^l+Cr^{-(l+1)}, \tag{2.10}$$

where B and C are constants.

Substituting equation (2.10) into equation (2.8) and simplifying, one obtains

$$\frac{d^2\Theta}{d\theta^2}+\frac{\cos\theta}{\sin\theta}\frac{d\Theta}{d\theta}+\left[l(l+1)-\frac{m^2}{\sin^2\theta}\right]\Theta=0. \tag{2.11}$$

Equation (2.11) is known as the associated Legendre equation. In terms of the variable $x=\cos\theta$, the solutions are the well known associated Legendre polynomials given by

$$\Theta=P_{lm}(x)=(1-x^2)^{m/2}\frac{d^m}{dx^m}P_l(x), \tag{2.12}$$

where $P_l(x)$ are the Legendre polynomials given by

$$P_l(x)=\frac{1}{2^l l!}\frac{d^l}{dx^l}(x^2-1)^l. \tag{2.13}$$

The full form of $\Theta=P_{lm}(x)$ is therefore

$$P_{lm}(x)=\frac{1}{2^l l!}(1-x^2)^{m/2}\frac{d^{l+m}}{dx^{l+m}}(x^2-1)^l. \tag{2.14}$$

These are all mutually orthogonal. The lowest order polynomials, in terms of $\cos\theta$, are given

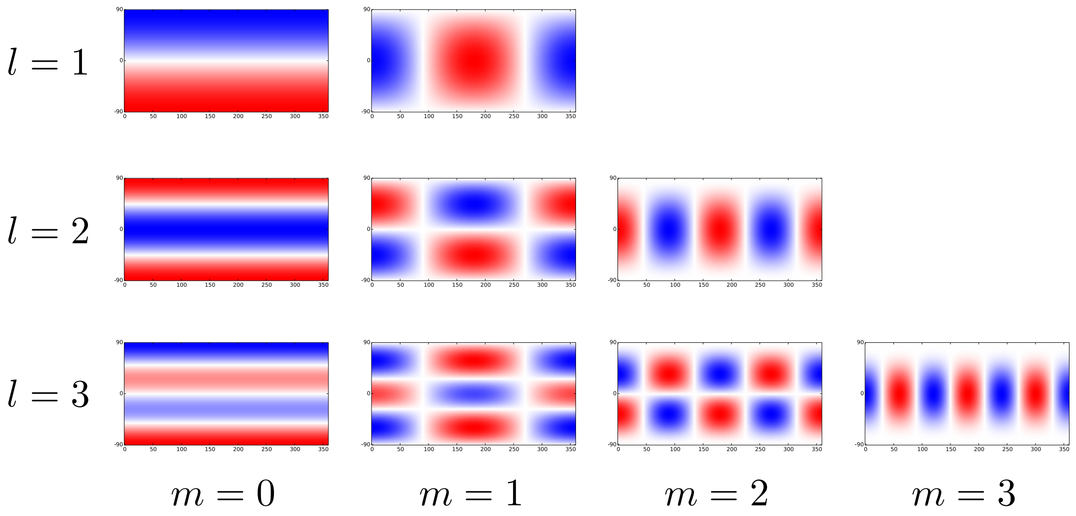

Figure 2.1: A visualisation of the real part of $P_{lm}e^{im\phi}$ for the lowest l and m values. Expressions for P_{lm} are given in equation (2.15). Red and blue regions correspond to opposite polarities. It can be seen that m defines the number of nodal crossings in the ϕ direction while $l - m$ defines the number of nodal crossings in the θ direction.

by

$$\begin{aligned}
P_{10} &= \cos\theta \\
P_{11} &= -\sin\theta \\
P_{20} &= \frac{1}{2}(3\cos^2\theta - 1) \\
P_{21} &= -3\cos\theta\sin\theta \\
P_{22} &= 3\sin^2\theta \\
P_{30} &= \frac{1}{2}(5\cos^3\theta - 3\cos\theta) \\
P_{31} &= -\frac{3}{2}(5\cos^2\theta - 1)\sin\theta \\
P_{32} &= 15\cos\theta\sin^2\theta \\
P_{33} &= -15\sin^3\theta
\end{aligned} \tag{2.15}$$

It is clear that the highest order of x inside the derivative of equation (2.14) is $2l$. The derivative is therefore restricted to orders where $m < l$ since $P_{lm}(x)$ will vanish at higher orders. The condition $m > -l$ is also imposed so that no negative order derivatives arise.

The full solution to Laplace's equation in spherical coordinates, expressed as a linear sum over all possible solutions of the azimuthal equation (equation 2.7), radial equation (equation 2.10) and polar equation (equation 2.14), is therefore

$$\Psi(r,\theta,\phi) = R(r)\Theta(\theta)\Phi(\phi) = \sum_{l=0}^{\infty}\sum_{m=-l}^{l}\left[a_{lm}r^{l} + b_{lm}r^{-(l+1)}\right]P_{lm}(\cos\theta)e^{im\phi}. \tag{2.16}$$

This solution is visualised in Fig. 2.1, where I have plotted the real part of the function $P_{lm}(\cos\theta)e^{im\phi}$, for the lowest values of l and m.

2.2 Representing magnetic fields

As noted at the beginning of section 2.1, a potential field can be represented as the gradient of the scalar field, **B** =-$\nabla\Psi$. Substituting for Ψ from equation (2.16), the three components of the magnetic field are therefore given by

$$B_r(r,\theta,\phi) = -\frac{\partial\Psi}{\partial r} = -\sum_{l=0}^{\infty}\sum_{m=-l}^{l}\left[a_{lm}lr^{l-1} - b_{lm}(l+1)r^{-(l+2)}\right]P_{lm}(\cos\theta)e^{im\phi}, \tag{2.17}$$

$$B_\theta(r,\theta,\phi) = -\frac{1}{r}\frac{\partial\Psi}{\partial\theta} = -\sum_{l=0}^{\infty}\sum_{m=-l}^{l}\left[a_{lm}r^{l-1} + b_{lm}r^{-(l+2)}\right]\frac{dP_{lm}(\cos\theta)}{d\theta}e^{im\phi}, \tag{2.18}$$

$$B_\phi(r,\theta,\phi) = -\frac{1}{r\sin\theta}\frac{\partial\Psi}{\partial\phi} = -\sum_{l=0}^{\infty}\sum_{m=-l}^{l}\left[a_{lm}r^{l-1} + b_{lm}r^{-(l+2)}\right]P_{lm}(\cos\theta)\frac{im}{\sin\theta}e^{im\phi}. \tag{2.19}$$

A few further simplifications can be made. Firstly, the $l = 0$ mode can be neglected since it represents a magnetic monopole which is unphysical. It also turns out that the negative m modes are equal, in amplitude, to the positive m modes. We can therefore rewrite equations (2.17), (2.18) and (2.19) as a summation over positive m modes only as follows:

$$B_r(r,\theta,\phi) = -\sum_{l=1}^{\infty}\sum_{m=0}^{l}(2-\delta_{m,0})\left[a_{lm}lr^{l-1} - b_{lm}(l+1)r^{-(l+2)}\right]P_{lm}(\cos\theta)e^{im\phi}, \tag{2.20}$$

$$B_\theta(r,\theta,\phi) = -\sum_{l=1}^{\infty}\sum_{m=0}^{l}(2-\delta_{m,0})\left[a_{lm}r^{l-1} + b_{lm}r^{-(l+2)}\right]\frac{dP_{lm}(\cos\theta)}{d\theta}e^{im\phi}, \tag{2.21}$$

$$B_\phi(r,\theta,\phi) = -\sum_{l=1}^{\infty}\sum_{m=0}^{l}(2-\delta_{m,0})\left[a_{lm}r^{l-1} + b_{lm}r^{-(l+2)}\right]P_{lm}(\cos\theta)\frac{im}{\sin\theta}e^{im\phi}, \tag{2.22}$$

where the Kronecker delta has a value of 1 if $m = 0$ and a value of 0 if $m \neq 0$. To represent the 3D coronal magnetic field, all we need do is specify the a_{lm} and b_{lm} coefficients. In principle, they would be chosen such that equations (2.20),(2.21) & (2.22) match the data obtained from spectropolarimetric observations. However, fitting a 3D global coronal field to the data proves to be difficult and leads to unphysical field geometries, possibly because not all of the field is observed due to, for example, flux cancellation within resolution elements. In practice, the full coronal field is modelled in two steps. Firstly, a magnetic map of the stellar surface is found by fitting equations (2.20),(2.21) & (2.22) to the data at $r = r_\star$. The global coronal field is then modelled using field extrapolating techniques, e.g. the PFSS model, with the magnetic map acting as an inner boundary condition. Each of these steps will be covered in the following sections.

2.2.1 Magnetic fields at the stellar surface

Surface fields can be represented under the assumption of zero field strength at infinity, i.e., $\mathbf{B} \to 0$ as $r \to \infty$. Looking at equations (2.20),(2.21) & (2.22), the a_{lm} coefficients must vanish to prevent the r^{l-1} terms from blowing up as $r \to \infty$. We also restrict ourselves to $r = r_\star$. Equations (2.20),(2.21) & (2.22) therefore become

$$B_r(\theta,\phi) = \sum_{l=1}^{\infty}\sum_{m=0}^{l}(2-\delta_{m,0})c_{lm}P_{lm}(\cos\theta)e^{im\phi}, \tag{2.23}$$

$$B_\theta(\theta,\phi) = -\sum_{l=1}^{\infty}\sum_{m=0}^{l}(2-\delta_{m,0})\frac{c_{lm}}{l+1}\frac{dP_{lm}(\cos\theta)}{d\theta}e^{im\phi}, \tag{2.24}$$

$$B_\phi(\theta,\phi) = -\sum_{l=1}^{\infty}\sum_{m=0}^{l}(2-\delta_{m,0})\frac{c_{lm}}{l+1}P(\cos\theta)\frac{im}{\sin\theta}e^{im\phi}. \tag{2.25}$$

where $c_{lm} = b_{lm}(l+1)r_\star^{-(l+2)}$.

In order to find the values for the c_{lm} coefficients, consider an expression of the form

$$\int_0^{2\pi}\int_0^{\pi} B_r(\theta,\phi)P_{l'm'}(\cos\theta)e^{-im'\phi}\sin\theta\, d\theta\, d\phi. \tag{2.26}$$

Substituting for $B_r(\theta,\phi)$ from equation (2.23), one obtains

$$\sum_{l=1}^{\infty}\sum_{m=0}^{l} c_{lm}(2-\delta_{m,0})\int_0^{2\pi} e^{im\phi}e^{-im'\phi}\,d\phi\int_0^{\pi} P_{lm}(\cos\theta)P_{l'm'}(\cos\theta)\sin\theta\, d\theta. \tag{2.27}$$

The only terms that are non-zero are those where l and m are simultaneously equal to l'

and m' respectively. Setting $l' = l$ & $m' = m$ and making use of the associated Legendre polynomial orthogonality condition,

$$\int_0^{\pi} P_{lm}(\cos\theta) P_{l'm'}(\cos\theta) \sin\theta d\theta = \frac{2\left[(l+m)!\right]}{(2l+1)\left[(l-m)!\right]}\delta_{l',l}, \tag{2.28}$$

we find that equation (2.27) reduces to

$$2\pi c_{lm}(2-\delta_{m,0})\frac{2\left[(l+m)!\right]}{(2l+1)\left[(l-m)!\right]}. \tag{2.29}$$

Equating this expression to equation (2.26) and rearranging for c_{lm}, one obtains

$$c_{lm} = \frac{(2l+1)\left[(l-m)!\right]}{4\pi(2-\delta_{m,0})\left[(l+m)!\right]} \int_0^{2\pi}\int_0^{\pi} B_r(\theta,\phi) P_{lm}.(\cos\theta) e^{-im\phi} \sin\theta d\theta d\phi \tag{2.30}$$

This expression tells us that only the radial field at the stellar surface needs to be known in order to determine the c_{lm} coefficients. These coefficients can then be used in conjunction with equations (2.23),(2.24) & (2.25) to fully specify the magnetic field at the stellar surface.

2.2.2 Non-potential surface fields

A general expression for surface fields in a potential state was presented in section 2.2.1. However, observations have shown that solar-type stars with non-potential surface fields are not uncommon (e.g. Jardine et al., 2013). Various authors (e.g. Donati et al., 2006b) incorporate the non-potential components of the surface fields using the expressions

$$B_r(\theta,\phi) = -\sum_{l=1}^{\infty}\sum_{m=0}^{l} \alpha_{lm} Y_{lm}(\theta,\phi), \tag{2.31}$$

$$B_\theta(\theta,\phi) = -\sum_{l=1}^{\infty}\sum_{m=0}^{l} [\beta_{lm} Z_{lm}(\theta,\phi) - \gamma_{lm} X_{lm}(\theta,\phi)], \tag{2.32}$$

$$B_\phi(\theta,\phi) = -\sum_{l=1}^{\infty}\sum_{m=0}^{l} [\beta_{lm} X_{lm}(\theta,\phi) + \gamma_{lm} Z_{lm}(\theta,\phi)], \tag{2.33}$$

where Y_{lm}, X_{lm} and Z_{lm} are given by

$$Y_{lm}(\theta,\phi) = \sqrt{\frac{(2l+1)}{4\pi}\frac{(l-m)!}{(l+m)!}} P_{lm}(\cos\theta) e^{im\phi}, \tag{2.34}$$

$$X_{lm}(\theta,\phi)=\frac{1}{l+1}\sqrt{\frac{(2l+1)}{4\pi}\frac{(l-m)!}{(l+m)!}}\frac{im}{\sin\theta}P_{lm}(\cos\theta)e^{im\phi}, \tag{2.35}$$

$$Z_{lm}(\theta,\phi)=\frac{1}{l+1}\sqrt{\frac{(2l+1)}{4\pi}\frac{(l-m)!}{(l+m)!}}\frac{dP_{lm}(\cos\theta)}{d\theta}e^{im\phi}. \tag{2.36}$$

Equations (2.31), (2.32) & (2.33) represent the magnetic field using a spherical harmonic decomposition (Chandrasekhar, 1961). These equations are the most general way of representing surface fields since there is no a priori assumption on the form of the magnetic field. Indeed, these equations are the most commonly used representation for maps reconstructed using the ZDI technique. By specifying the values of α_{lm}, β_{lm} & γ_{lm}, it is possible to represent any magnetic field. These coefficients are determined from ZDI by inverting a set of Stokes signatures (see section 1.3.2). Barring some normalisation factors, the potential case can be recovered by setting the coefficients to $\gamma_{lm}=0$ and $\beta_{lm}=-\alpha_{lm}=c_{lm}$.

In section 1.4, I discussed the various properties of magnetic fields that are often used in the literature and will also be used later on in this thesis. These properties can be expressed as a combination of various modes or components of equations (2.31), (2.32) & (2.33). The average surface magnetic energy is given by $\langle B^2\rangle = \langle B_r^2 + B_\phi^2 + B_\theta^2\rangle$, using the full forms of equations (2.31), (2.32) & (2.33), where the angled brackets denotes an average over the stellar surface. The poloidal part of the magnetic field, $\langle B^2_{\rm pol}\rangle$ is given by the α_{lm} and β_{lm} terms while the toroidal part, $\langle B^2_{\rm tor}\rangle$, is given by the γ_{lm} terms. Physically, the toroidal component represents field lines that lie on spheres concentric with the star. The poloidal component consists of magnetic field lines that cut through these concentric spheres and is defined such that its curl gives the toroidal component. For the axisymmetric component of the field, $\langle B^2_{\rm axi}\rangle$, only the $m=0$ modes are considered with non-axisymmetric component, $\langle B^2_{\rm non-axi}\rangle$ being comprised of the $m>0$ modes[1]. Combinations of these components are also used in the literature. For instance, the axisymmetric toroidal field is given by the γ_{0m} terms.

2.2.3 Extrapolating the 3D coronal field

In this section, I shall discuss how stellar magnetic fields can be represented in a 3D volume around the star. Similarly to surface fields in the preceding sections, 3D magnetic fields can be represented by spherical harmonics. Indeed, one possible way in which the 3D field can

---

[1] It is worth noting that some authors use $m < l/2$ as an alternative definition for axisymmetry. This definition only requires that the magnetic axis be less than 45° from the rotation axis to be considered axisymmetric, as opposed to the stricter definition I use, which requires that the magnetic and rotation axis be exactly aligned.

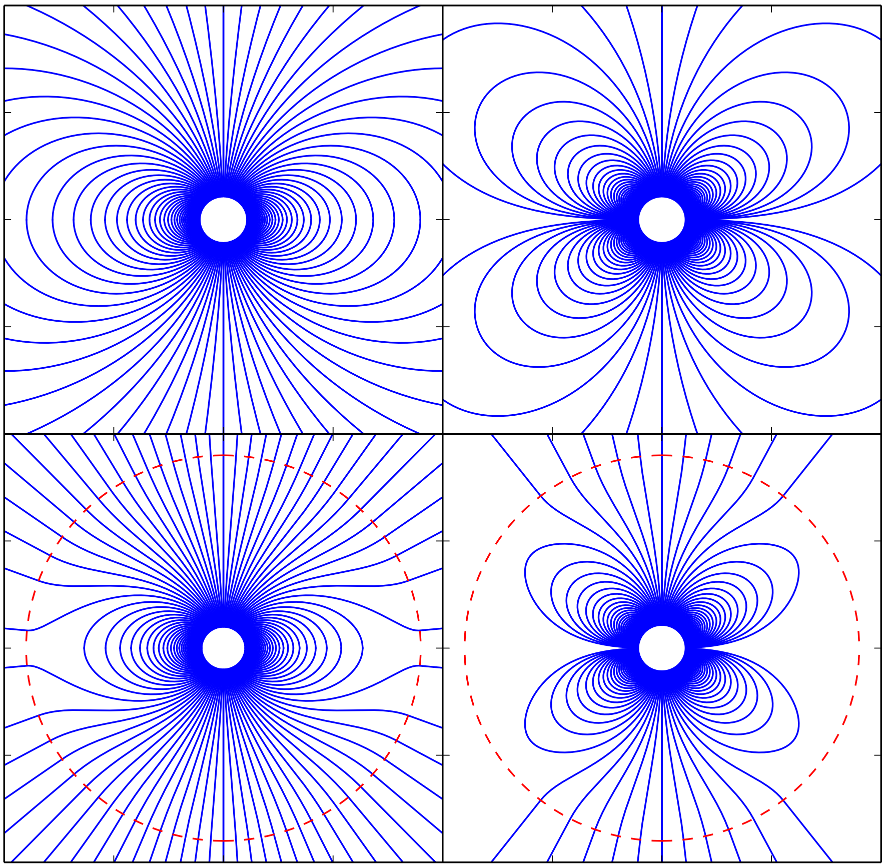

Figure 2.2: A visualisation of how various spherical harmonic modes are modified by the potential field source surface model. Shown are the field lines of a pure dipole (top left), pure quadrupole (top right) and their geometries under the PFSS model (bottom row). Each panel shows a 2D cut in the (r, θ) plane. The dashed red lines indicate the location of the source surface.

be represented was already previously demonstrated in. In section 2.2.1, a set of equations to represent magnetic fields on the surface of the star was derived under the assumption that $\mathbf{B} \rightarrow 0$ as $r \rightarrow \infty$. There is no reason why these equations cannot be generalised to represent the entire coronal field, at all radii above the stellar surface, by leaving the c_{lm} coefficients to be functions of r rather than forcing them to be constants evaluated at $r = r_{\star}$.

However, there is another, more physically motivated, assumption that we may wish to make. At large distances away from the star, the thermal plasma pressure is great enough to open up closed field lines into an approximately radial configuration. This idea can be modelled by imposing that the field geometry at some radius, r_{ss}, known as the source surface, becomes purely radial, i.e., $B_{\theta}(r_{ss}, \theta, \phi) = B_{\phi}(r_{ss}, \theta, \phi) = 0$, and is known as the potential field source surface model (PFSS; Altschuler & Newkirk, 1969). Examples of how the PFSS model affects various field modes are shown in Fig. 2.2. From equations (2.21) and (2.22), this condition requires that the a_{lm} and b_{lm} coefficients obey the relation

$$a_{lm} r_{ss}^{l-1} + b_{lm} r_{ss}^{-(l+2)} = 0 \tag{2.37}$$

or equivalently

$$\frac{a_{lm}}{b_{lm}} = -r_{ss}^{-(2l+1)}. \tag{2.38}$$

It is worth noting that B_θ and B_ϕ would also vanish when the a_{lm} and b_{lm} coefficients are both set to zero. However, this constraint has the undesirable effect of setting the B_r component to zero as well. Using equation (2.38), equations (2.17), (2.18) and (2.19) can be rewritten as

$$B_r(r,\theta,\phi) = -\sum_{l=1}^{\infty}\sum_{m=0}^{l}(2-\delta_{m,0})B_{lm} f_l(r) P_{lm}(\cos\theta) e^{im\phi}, \tag{2.39}$$

$$B_\theta(r,\theta,\phi) = -\sum_{l=1}^{\infty}\sum_{m=0}^{l}(2-\delta_{m,0})B_{lm} g_l(r) \frac{dP_{lm}(\cos\theta)}{d\theta} e^{im\phi}, \tag{2.40}$$

$$B_\phi(r,\theta,\phi) = -\sum_{l=1}^{\infty}\sum_{m=0}^{l}(2-\delta_{m,0})B_{lm} g_l(r) P_{lm}(\cos\theta) \frac{im}{\sin\theta} e^{im\phi}, \tag{2.41}$$

where B_{lm} is defined to be

$$B_{lm} = -a_{lm} l r_\star^{l-1} + b_{lm}(l+1) r_\star^{-(l+2)}, \tag{2.42}$$

and $f_l(r)$ and $g_l(r)$ are given by

$$f_l(r) = \left[\frac{(l+1)\left(\frac{r}{r_\star}\right)^{-(l+2)} + l\left(\frac{r_{ss}}{r_\star}\right)^{-(2l+1)}\left(\frac{r}{r_\star}\right)^{l-1}}{l\left(\frac{r_{ss}}{r_\star}\right)^{-(2l+1)} + (l+1)}\right], \tag{2.43}$$

$$g_l(r) = \left[\frac{\left(\frac{r}{r_\star}\right)^{l-1}\left(\frac{r_{ss}}{r_\star}\right)^{-(2l+1)} - \left(\frac{r}{r_\star}\right)^{-(l+2)}}{l\left(\frac{r_{ss}}{r_\star}\right)^{-(2l+1)} + (l+1)}\right]. \tag{2.44}$$

The equations derived in this section only apply to radial distances up to, and including, the source surface, $r < r_{ss}$. At greater distances, the magnetic field is completely radial and falls of as an inverse square law.

Following similar arguments to those used for the c_{lm} coefficients in the previous expression, it is possible to find an expression for the B_{lm} coefficients in terms of the radial field at the stellar surface, $B_r(r = r_\star, \theta, \phi)$. For $r = r_\star$, the function $f_l(r)$ is equal to one, and therefore equation (2.39) has the same form as equation (2.23) with B_{lm} in place of c_{lm}. By analogy with c_{lm} then, B_{lm} can be expressed as

$$B_{lm} = \frac{(2l+1)\,[(l-m)!]}{4\pi\,[(l+m)!]} \int_0^{2\pi} \int_0^{\pi} B_r(r_\star, \theta, \phi) P_{lm}(\cos\theta) e^{-im\phi} \sin\theta d\theta d\phi. \tag{2.45}$$

Since only the radial surface field is needed to determine the B_{lm} coefficients, and because all three components of the coronal field can be determined fully from B_{lm}, the full coronal field is determined by the radial field at the stellar surface alone.

3

The energy budget of stellar magnetic fields

This chapter is based on the work presented in See et al. (2015b).

3.1 Introduction

The Zeeman-Doppler imaging (ZDI) technique has greatly increased our understanding of stellar magnetic fields (Donati & Landstreet, 2009). In section 1.4, I gave a general overview of the results obtained with ZDI. In this chapter, I will discuss the properties of stellar magnetic fields in more depth and investigate how their components depend on fundamental stellar parameters such as mass or rotation period. In particular, I will focus on the toroidal component as described in section 2.2.2.

The toroidal component of these fields are interesting for a number of reasons. For instance, it can contain the free energy that, once liberated, is responsible for energetic events. Flares, coronal mass ejections and space weather in general have a large influence on the stellar environment, and can affect any planets orbiting the host star (Zarka, 2007; Grießmeier et al., 2007a; Llama et al., 2011; Vidotto et al., 2012, 2013, 2015; See et al., 2014, 2015a;

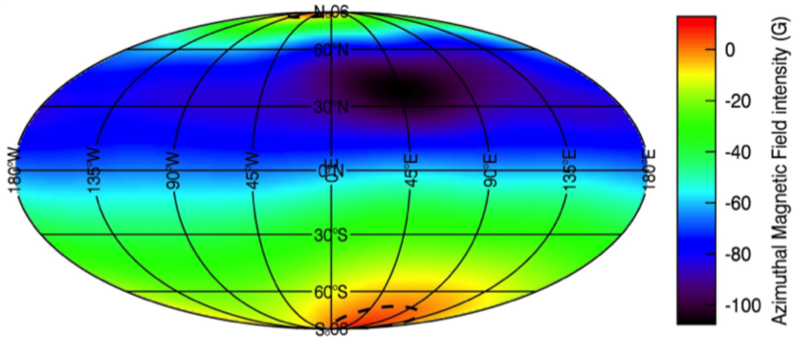

Figure 3.1: A map of the azimuthal toroidal field of ξ Boo A. A ring of uni-directional field can clearly be seen. Data provided by Petit et al. (in prep).

Cohen et al., 2015, see chapters 5 and 6 for further discussion). Numerical modelling has also shown that strong toroidal fields can be generated under certain circumstances (e.g. Browning et al., 2006; Brown et al., 2010).

Another point of interest is the presence of rings of toroidal azimuthal fields that have been observed on a range of stars of different spectral types (e.g. Donati et al., 1997; Donati, 1999; Petit et al., 2009; Morgenthaler et al., 2012; Jeffers et al., 2014; Boro Saikia et al., 2015, also, see Fig. 3.1). Such rings are not seen on the Sun and came as a surprise when they were first observed. As highlighted by Jardine et al. (2013), these bands can only exist if the magnetic field has been stressed above its lowest energy state. Additionally, these authors determine that stellar winds cannot be the source of these stresses. Other authors have suggested that such azimuthal fields are evidence of dynamos distributed throughout the convection zone (Donati et al., 1997, 2003a,b) rather than being confined to the tachocline as in the Sun. This view is supported by the work of Brown et al. (2010) who demonstrate that a tachocline is not required to generate strong bands of toroidal fields in rapidly rotating solar-like stars.

Presently, the toroidal component of stellar magnetic fields has only been studied in single, or small samples, of stars. Petit et al. (2008) studied a sample of four solar-like stars and noted that the stellar rotation period plays an important role in determining the fraction of magnetic energy in the toroidal component of the stellar field (see section 1.4.2). However, the rotation period cannot be the sole parameter that determines the toroidal energy fraction since stars with similar rotation periods show different toroidal energy fractions. Additionally, observations of individual stars, over multiple epochs, show that the toroidal energy fraction

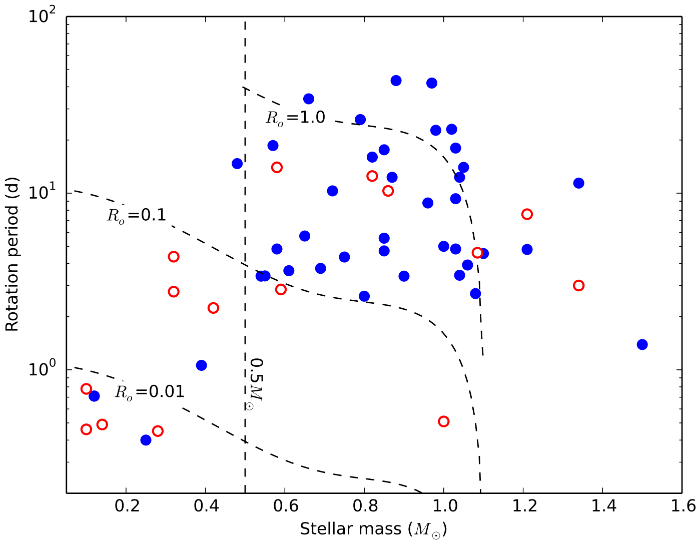

Figure 3.2: The rotation periods and masses of each star in the sample. Filled blue points indicate stars observed at one epoch while open red data points indicate stars observed over multiple epochs. Dashed lines are included showing a stellar mass of 0.5 $M_\odot$ and Rossby numbers of 0.01, 0.1 and 1.0.

can change significantly on the time-scale of years (Donati et al., 1997, 1999, 2003a; Petit et al., 2009; Fares et al., 2010; Morgenthaler et al., 2012; Fares et al., 2013; Jeffers et al., 2014; Boro Saikia et al., 2015). This indicates that stellar dynamos are dynamic and cannot be characterised by single time averaged parameters.

In this chapter, I conduct a statistical study of toroidal fields using a sample of 55 stars with ZDI maps. In section 3.2, I outline the properties of the sample used. In section 3.3, I present a number of results related to the toroidal fields of this sample. Concluding remarks follow in section 3.4.

3.2 Stellar sample

For this work, I employ 90 magnetic maps of 55 dwarf stars with spectral types spanning F, G, K and M. These maps were reconstructed by various authors using the ZDI technique as outlined in section 1.3.2. The original publications for each map are referenced in Table 3.1. Each map contains information about the large-scale magnetic field at the surface of the star. In this work I will make use of the magnetic energy density averaged across the stellar surface, $\langle B^2\rangle$, as well as the toroidal, $\langle B^2_{\mathrm{tor}}\rangle$, & poloidal, $\langle B^2_{\mathrm{pol}}\rangle$, components and the axisymmetric, $\langle B^2_{\mathrm{axi}}\rangle$, & non-axisymmetric, $\langle B^2_{\mathrm{non-axi}}\rangle$, components. These are characterised by the α_{lm}, β_{lm} & γ_{lm}

coefficients as described by (Donati et al., 2006a) and summarised in section 2.2.2. The numerical values for each of these components are given in Table 3.1.

Additional parameters for each star are also listed in Table 3.1. Fig. 3.2 shows the rotation periods and masses of the stars in this sample. Stars with a single map are plotted with filled blue points while stars with multiple maps over many epochs are plotted with open red points. Although I principally focus on mass and rotation rates in this work, there may be other parameters, such as stellar age (Folsom et al., 2016) or the presence of planets (Fares et al., 2013), that affect the magnetic properties of stars. The stellar masses range from $0.1\,\mathrm{M}_\odot$ to $1.5\,\mathrm{M}_\odot$ while the rotation rates range from 0.4 days to nearly 50 days. It is worth noting that there is a slight trend in this sample whereby the highest mass stars have the longest rotation periods. I will discuss this point further in section 3.3.3.

3.3 Results

3.3.1 Toroidal Fields

One of the principle ways to characterise the stellar magnetic energy is to study its poloidal and toroidal components (shown in Fig. 3.3). The top panel shows toroidal magnetic energy density against poloidal magnetic energy density while the bottom panel shows the toroidal energy fraction against stellar mass. Both panels are colour coded by stellar mass aiding comparison between them.

The top panel shows that the toroidal energy is an increasing function of poloidal energy. It should be possible to fit a power law of the form $\langle B_{\mathrm{tor}}^2\rangle \propto \langle B_{\mathrm{pol}}^2\rangle^a$ to these points. However, the sample seems to consist of two sub-samples. The stars with higher magnetic energy densities appear to have a smaller power index, a, than the lower energy stars. A priori, it is not clear which stars should be included in which sub-sample. In the bottom panel, a change of behaviour is evident at approximately $0.5\,\mathrm{M}_\odot$. Stars with a larger mass than this can have large toroidal energy fractions but lower mass stars cannot. Though the two panels show essentially the same information, this break in behaviour at $0.5\,\mathrm{M}_\odot$ is much clearer in the bottom panel. As discussed in section 1.4.1, a number of authors have previously discussed a sudden change in the magnetic properties of M dwarfs at roughly $0.5\,\mathrm{M}_\odot$ (Donati et al., 2008a; Morin et al., 2008b, 2010; Gregory et al., 2012). They note that this break is roughly coincident with the fully convective limit suggesting a link with the change in internal

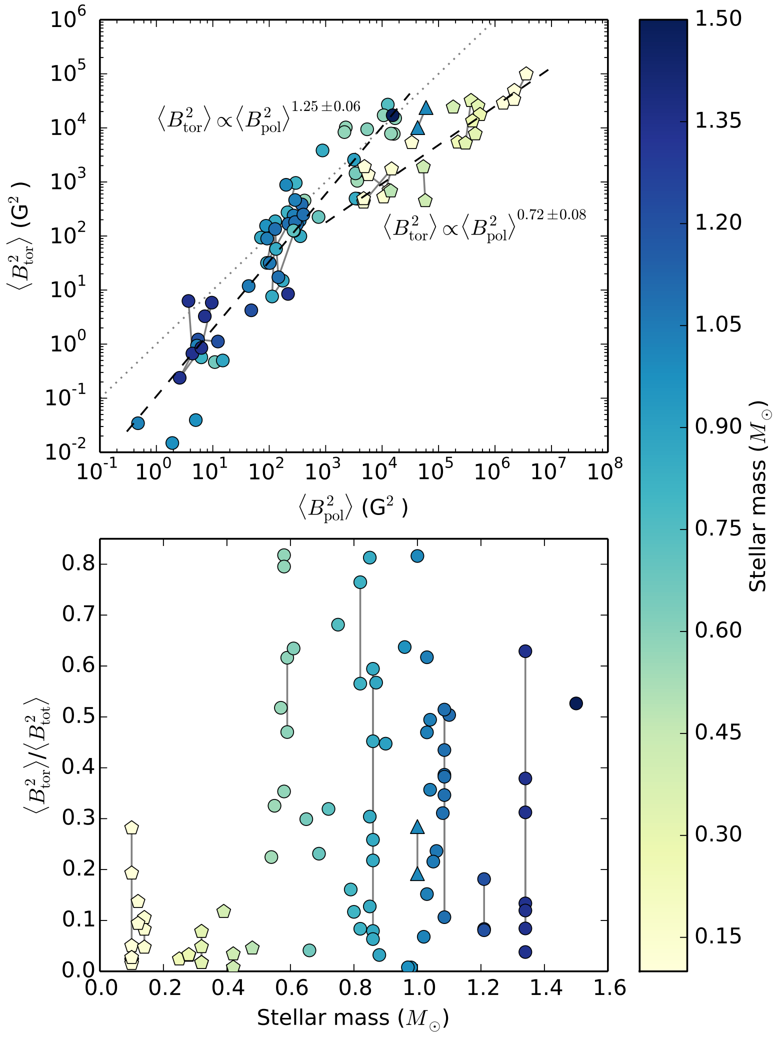

Figure 3.3: Top: toroidal magnetic energy against poloidal magnetic energy. Stars with multiple maps are connected by grey lines. The dotted line indicates $\langle B^2_{\rm tor}\rangle = \langle B^2_{\rm pol}\rangle$. The sample is split into stars less massive (pentagon markers) and more massive than $0.5\,{\rm M}_\odot$ (circle markers). See text for further discussion of how these sub-samples were chosen. The two dashed lines are best fit lines for these sub-samples; $\langle B^2_{\rm tor}\rangle \propto \langle B^2_{\rm pol}\rangle^a$ with $a = 0.72 \pm 0.08$ and $a = 1.25 \pm 0.06$ for ${\rm M} < 0.5\,{\rm M}_\odot$ and ${\rm M} > 0.5\,{\rm M}_\odot$ respectively. AB Dor is shown with triangles. Each point is colour coded by stellar mass. Bottom: toroidal energy fraction against stellar mass. Format is the same as the top panel. Data-points are also colour coded by stellar mass to aid comparison with the top panel. While the two panels show very similar information, the difference in behaviours of the two mass ranges is much clearer in the bottom panel.

structure. Dividing the sample on this basis, I find power index values of $a = 0.72 \pm 0.08$ and $a = 1.25 \pm 0.06$ for stars less and more massive than $0.5\,{\rm M}_\odot$ respectively. These power laws are plotted in the top panel with dashed lines. It is worth noting that, among the ${\rm M} < 0.5\,{\rm M}_\odot$ stars, it is the dipole-dominated stars that deviate the most from the higher index power law.

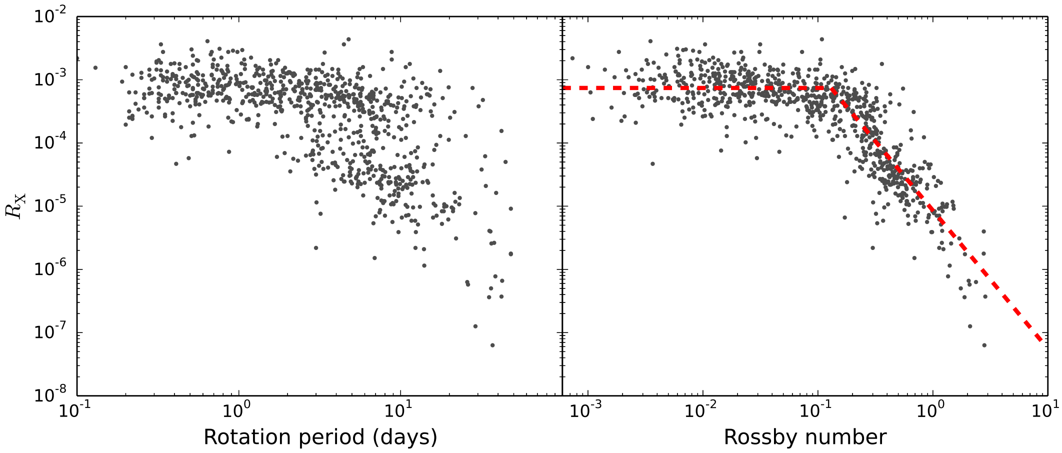

Figure 3.4: The ratio of X-ray to bolometric luminosity, $R_\mathrm{X} = L_\mathrm{X}/L_\mathrm{bol}$, against rotation period (left) and Rossby number (right). Both show increasing, and eventual saturation of, R_X with more rapid rotation. However, the scatter is vastly reduced when plotted as a function of Rossby number. Figure reproduced with permission from Wright et al. (2011).

The non-dipolar stars in the bistable regime, as discussed by Morin et al. (2010), are roughly compatible with the more shallow power law. Additionally, theoretical models predict that these non-dipolar stars can vary cyclically and are able to generate significant toroidal fields (e.g. Gastine et al., 2013).

As a brief aside, I discuss the possibility that the smaller toroidal energy fraction of stars less massive than $0.5\,\mathrm{M}_\odot$ is a result of the ZDI technique. ZDI captures the large-scale fields but is insensitive to small-scale fields due to flux cancellation effects. Reiners & Basri (2009) show that the majority of magnetic flux may be missed when the stellar field is reconstructed using only the Stokes V signal when compared to the Stokes I signal. If the lowest mass M dwarfs have a large fraction of their magnetic energy stored in small scale fields, in the form of star spots for example, these fields may not be reconstructed by the ZDI technique. However, there is no reason to expect ZDI to preferentially miss toroidal field over poloidal field.

3.3.2 Field saturation

It is a well known observational result that the ratio of X-ray to bolometric luminosity, $R_\mathrm{X} = L_\mathrm{X}/L_\mathrm{bol}$, increases with increasing rotation rates with saturation occurring for the most rapid rotators. This is demonstrated in Fig. 3.4 where R_X is plotted against rotation period and Rossby number. It is also clear that there is significantly less scatter for the Rossby number

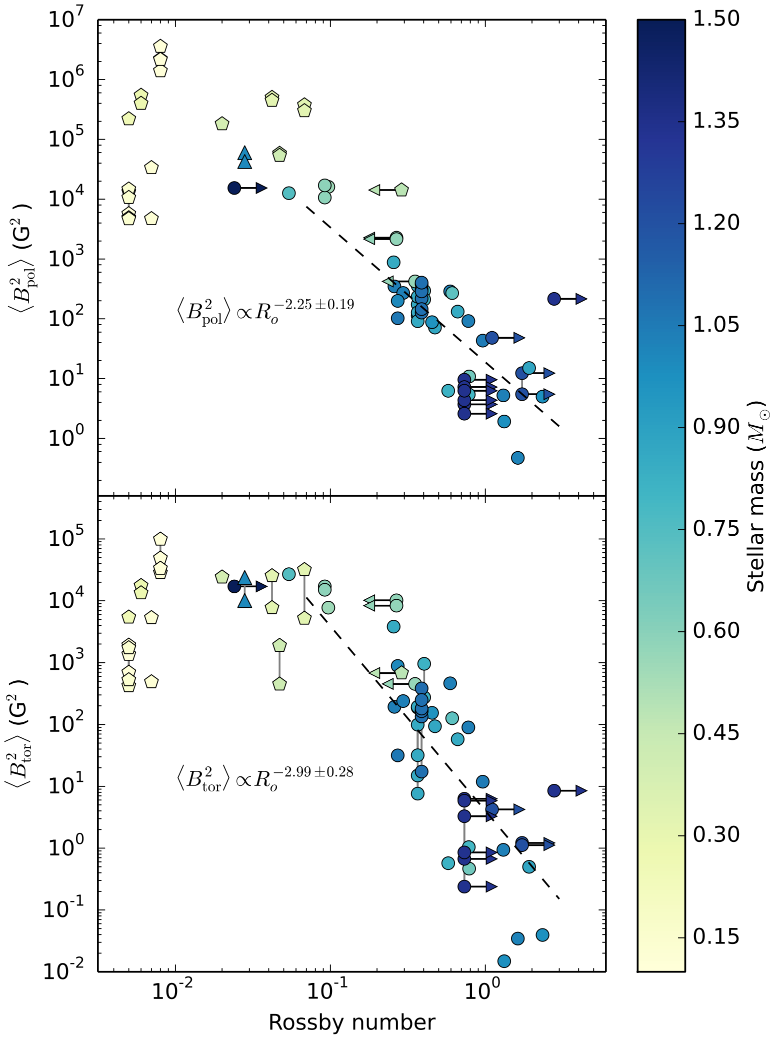

Figure 3.5: Poloidal (top) and toroidal (bottom) magnetic energy against Rossby number. The formatting is the same as Fig. 3.3. Right/left facing arrows indicate stars that only have lower/upper estimates for their Rossby numbers. The saturated and unsaturated regimes can be clearly seen with the transition occurring at a Rossby number of approximately 0.1. Fits to the stars in the unsaturated regime, $\langle B^2_{\rm pol} \rangle \propto {\rm Ro}^{-2.25\pm0.19}$ and $\langle B^2_{\rm tor} \rangle \propto {\rm Ro}^{-2.99\pm0.28}$, are shown with dashed lines. Note: the magnetic energy axes of the two plots are not the same.

suggesting that it is a more fundamental parameter than rotation period in the context of magnetic activity. A clear divide between the so called saturated and unsaturated regimes is evident at Ro $\sim$ 0.1 (Pizzolato et al., 2003; Wright et al., 2011). This behaviour is known as the activity-rotation relation.

Vidotto et al. (2014) showed that stellar magnetism has the same qualitative dependence on Rossby number. However, this result was derived using the radial component of the surface fields only, and hence does not consider the toroidal field. In Fig. 3.5, I plot the poloidal (top panel) and toroidal (bottom panel) magnetic energy densities as a function of Rossby number. I use the same Rossby number estimates as Vidotto et al. (2014), where further discussion of the estimates can be found. Left and right facing arrows indicate stars where the Rossby number estimate is only an upper or lower limit respectively.

It is clear to see that both components qualitatively follow the behaviour of the activity-rotation relation with some quantitative differences. In both cases, the cutoff between the saturated and unsaturated regimes occurs at Ro ~ 0.1. However, in the saturated regime, the average magnetic energy of the poloidal fields is higher than that of the toroidal fields by just over an order of magnitude. Additionally, in the unsaturated regime, the slope is steeper for the toroidal component. The similar behaviour indicates that the same mechanism is responsible for generating both components or that both components are generated from each other.

Wright et al. (2011) suggested that the difference in R_X behaviour in the saturated and unsaturated regimes can be attributed to different dynamo mechanisms operating in each of the regimes rather than any actual saturation effect. They argued this on the basis that the age at which stars transition from the rotational C sequence to the I sequence (Barnes, 2003) is coincident with the transition from saturated to unsaturated regimes at Ro ~ 0.1 (see their Fig. 4). It is interesting to note that the majority of the stars in the saturated regime in Fig. 3.5 have $\mathrm{M} < 0.5\,\mathrm{M}_\odot$ (pentagon symbols). Assuming that the unsaturated stars are those more massive than $0.5\,\mathrm{M}_\odot$, I find fits of $\langle B^2_{\mathrm{pol}}\rangle \propto Ro^{-2.25\pm0.19}$ and $\langle B^2_{\mathrm{tor}}\rangle \propto Ro^{-2.99\pm0.28}$ for the poloidal and toroidal fields respectively. These fits are plotted with dashed lines. It is worth noting that these two fits and the fit in Fig. 3.3 with the higher power index, $a = 1.25$, are the three possible 2D projections of the same relatively tight sequence of stars in $(\langle B^2_{\mathrm{pol}}\rangle, \langle B^2_{\mathrm{tor}}\rangle, \mathrm{Ro})$ parameter space.

3.3.3 Different dynamo modes?

If there is a physical basis for the saturated stars having masses less than $0.5\,\mathrm{M}_\odot$, the fact that they appear to have a different power index, a, to the rest of the stars, in Fig. 3.3, is further evidence for the suggestion of Wright et al. (2011). However, care must be taken with this interpretation. Fig. 3.2 shows that the majority of stars in the sample that are less than $0.5\,\mathrm{M}_\odot$ also have Rossby numbers less than 0.1. Therefore, the interpretation is not that stars in the saturated regime must be less massive than $0.5\,\mathrm{M}_\odot$. Rather, it is that stars in the saturated regime are those with Rossby numbers less than $\sim$0.1 which also happen to be stars less massive then $0.5\,\mathrm{M}_\odot$ in the sample used in this chapter. Noticeably, with the exception of AB Dor ($\mathrm{Ro} = 0.028$, $\mathrm{M} = 1.0\mathrm{M}_\odot$), there is a dearth of stars with Rossby numbers less than $\sim$0.1 and masses bigger than $0.5\,\mathrm{M}_\odot$ in the sample. That the lowest mass stars in the sample are also the fastest rotators is not surprising since these stars spin down less rapidly than higher mass stars (Mohanty & Basri, 2003; Gallet & Bouvier, 2015). Correspondingly $\mathrm{Ro} \lesssim 0.1$, $\mathrm{M}_\star > 0.5\,\mathrm{M}_\odot$ stars are harder to find and map. Indeed a number of authors have previously commented on the difficulty in separating stellar mass and Rossby number effects due to this bias (Donati et al., 2008a; Morin et al., 2008b, 2010; Reiners & Basri, 2009; Gastine et al., 2013). Even when AB Dor is considered (plotted with triangles in Figs. 3.3 and 3.5), which does fall into the $\mathrm{Ro} \lesssim 0.1$, $\mathrm{M}_\star > 0.5\,\mathrm{M}_\odot$ region of parameter space, the picture does not become any clearer. In the top panel of Fig. 3.3, AB Dor lies relatively close to both sub-samples such that it is difficult to tell which sub-sample it would be more appropriate for it to be in. Likewise, in Fig. 3.5, AB Dor falls in an intermediate region. On one hand, one might consider it a saturated star on the basis of its Rossby number which is smaller than $\mathrm{Ro} \sim 0.1$, the value typically used to delineate the saturated and unsaturated regimes. However, one might also consider it to be an unsaturated star on the basis that it follows the same trend as the other unsaturated stars, lying at the tail end of that sequence. If the hypothesis of Wright et al. (2011) is correct, one might expect the magnetic fields of the stars in this region of parameter space to obey the power law with the smaller index from Fig. 3.3.

A potential problem with this interpretation is that the two sub-samples were initially chosen on the basis of stellar mass, since this parameter better discriminates between the two power laws in Fig. 3.3, rather than Rossby number. It may be the case that the two power laws in Fig. 3.3 do not correspond to the saturated and unsaturated regimes. Indeed, until more stars in the $\mathrm{Ro} < 0.1$, $M_\star > 0.5\,\mathrm{M}_\odot$ region of parameter space (corresponding to stars of rotation periods of less than a few days - see Fig. 3.2) have their surface fields mapped, it will be difficult to conclusively confirm or reject this hypothesis.

Recently, Reiners et al. (2014) reinterpreted the data of Wright et al. (2011). These authors show that, in the unsaturated regime, $R_\mathrm{X} = L_\mathrm{X}/L_\mathrm{bol}$ shows less scatter when plotted against $R_*^{-4}P_\mathrm{rot}^{-2}$, where R_* and P_rot are the stellar radius and rotation period respectively, rather than Rossby number, as is traditional in these types of studies. This formulation is approximately equivalent to $L_\mathrm{X} \propto P_\mathrm{rot}^{-2}$, i.e. that X-ray luminosity depends only on the stellar rotation period, in the unsaturated regime. The authors make no claims as to whether R_X as a function of Ro or L_X as a function of P_rot is the more physically fundamental relationship. When plotting $\langle B_\mathrm{pol}^2 \rangle$ and $\langle B_\mathrm{tor}^2 \rangle$ against $R_*^{-4} P_\mathrm{rot}^{-2}$ (not shown), I once again find that the data separates into saturated and unsaturated regimes. Similarly to Fig. 3.5, the stars in the saturated regime are those that are less massive than $0.5\,\mathrm{M}_\odot$. The suggestion that different dynamo mechanisms are present in the saturated and unsaturated regimes is therefore not ruled out under either interpretation of the rotation-activity relation.

3.3.4 Band latitudes

In this section I determine the latitude and extent of azimuthal bands of toroidal field in the sample of stars. Firstly, by examining the magnetic maps, I eliminate those stars that show no evidence of strong bands by determining the fraction of latitudes with only a single polarity in the toroidal component of the azimuthal field. From a visual inspection, stars in which this fraction is less than 0.2 do not have clear bands and I do not attempt to find a band latitude for these stars. For the remaining 67 maps, I average the field strengths over every longitude to obtain an average field strength as a function of latitude and then take the absolute value, i.e. $|\langle B_{\mathrm{tor},\phi} \rangle|(\lambda)$ where λ is the latitude. I plot the latitude at which this function is maximal in Fig. 3.6 as a function of rotation period for each star. Stars with maps over multiple epochs are indicated by grey lines. An indication of the band width is given by the full-width half-maximum of the peak in $|\langle B_{\mathrm{tor},\phi} \rangle|(\lambda)$. The size of each data point is scaled by the full-width half maximum. All points are colour coded by stellar mass. Numerical values for this plot are included in Table 3.2. It is worth highlighting that multiple azimuthal bands of opposing polarity were seen in the rapid rotators HR 1099 and AB Dor (Donati et al., 2003a).

Several authors have noted that magnetic flux tends to emerge at higher latitudes on stars with shorter rotation periods as a result of a larger Coriolis force dominating over the magnetic buoyancy of the flux tubes (Schuessler & Solanki, 1992; Schuessler et al., 1996; Granzer, 2002, also, see Fig. 3.6). These results are in qualitative agreement of this statement, with the upper envelope of band latitudes in Fig. 3.6 showing a decreasing trend at longer rotation periods. However, the interplay between Coriolis and buoyancy forces alone cannot explain the large range of band latitudes seen at a given rotation period. This is especially true of stars with multiple maps that show the band latitude changing significantly over the course

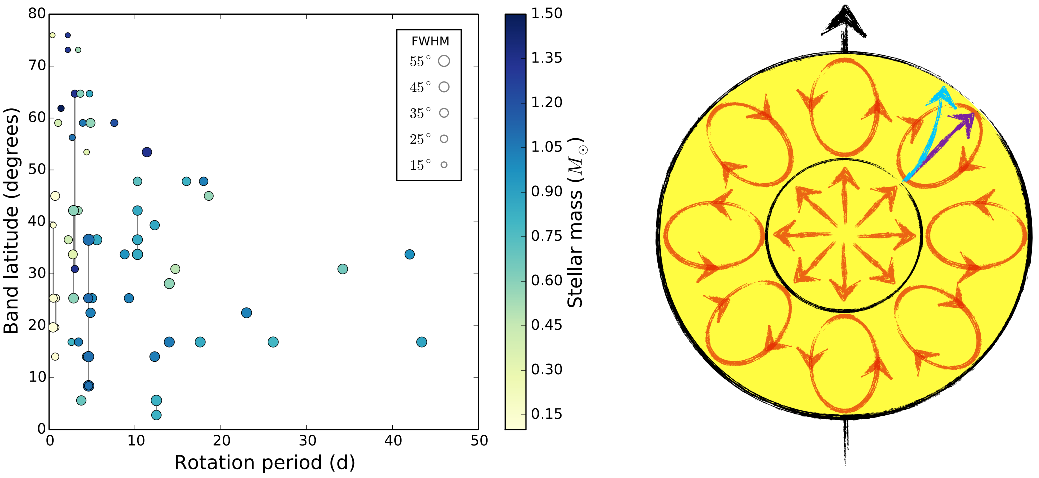

Figure 3.6: Left: the latitude at which the toroidal azimuthal field peaks for each star as a function of stellar rotation period. Each point is colour coded by stellar mass. The size of the points indicates the full-width half-maximum value for the band (see inset). Stars with multiple maps are connected by grey lines. Numerical values for the data points are included in Table 3.2. Right: a sketch of a solar type star showing the radiative core and convective outer layer. Arrows representing the buoyant rise of a flux tube from the tachocline is shown for a slowly rotating star (purple arrow) and a rapid rotator (blue arrow). Flux tubes are deflected to higher latitudes in more rapidly rotating stars.

of months/years. In some cases, the azimuthal bands even disappear and reappear between observation epochs.

3.3.5 Field orientation

From a visual inspection of the magnetic maps, toroidal azimuthal bands appear predominantly axisymmetrically (e.g. Jardine et al., 2013, and Fig. 3.1). Figure 3.7 shows the fraction of magnetic energy in axisymmetric modes against the fraction contained in the toroidal component of the field. Mathematically, these correspond to the energy in the $m = 0$ modes and the γ_{lm} coefficients respectively. Stars with multiple epochs of observations are connected by grey lines and each point is colour coded by stellar mass. The most striking feature is the dearth of toroidal non-axisymmetric stars, in the lower right corner of the plot. Additionally, there is no trend evident with stellar mass.

The striking trend in Fig. 3.7 warrants a check for potential biases in the ZDI technique. Crosstalk between the field components, especially the radial and meridional fields is well known and has been characterised (Donati & Brown, 1997b)[1]. In particular, it is leakage from

---

[1] In the tests presented by Donati & Brown (1997b), the individual field components are considered to be inde-

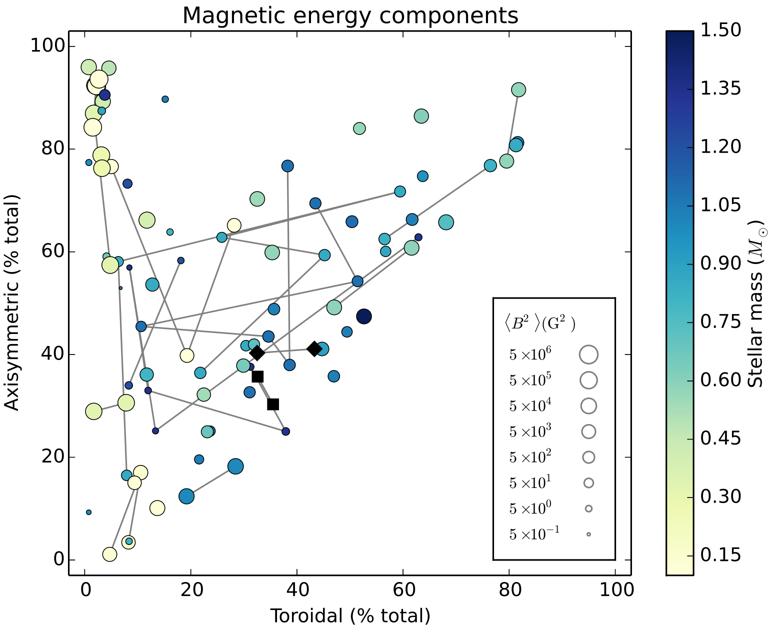

Figure 3.7: Percentage of total magnetic energy contained in the axisymmetric component of the field against percentage of total magnetic energy contained in toroidal field. Stars observed at multiple epochs are connected by grey lines. The data points are colour coded by stellar mass and scale with the total magnetic energy density, $\langle B^2 \rangle$ (see inset). Rosén et al. (2015) reconstructed the surface field of II Peg using Stokes IV (circularly polarised light) and also Stokes IQUV (circularly and linearly polarised light). These data points are shown by black diamond and square markers respectively.

the toroidal fields into the poloidal fields that would be problematic. To this end, a series of systematic tests were conducted. Specifically, a grid of synthetic Stokes profiles corresponding to magnetic field geometries where the axisymmetric and toroidal energy fractions ranged from zero to one were created. Magnetic maps were then reconstructed from these profiles and compared to the original maps that the synthetic profiles were created from. Full details of these tests can be found in Folsom et al. (in prep). Some energy leakage from toroidal into poloidal fields (and vice versa) were found as a result of these tests. This effect is largest for geometries where the order, l, is equal to the degree, m and smallest when there is a large difference between l and m. However, the effect is not large enough to explain the dearth of points in the lower right hand corner of Fig. 3.7.

The magnetic maps used in this study were all reconstructed using the Stokes I (unpolarised) and Stokes V (circularly polarised) profiles with one exception. Rosén et al. (2015)

---

pendent parameters. With the new spherical harmonic implementation, as described by Donati et al. (2006a), crosstalk is considerably reduced.

observed the star II Peg, during two epochs, in all four Stokes parameters ($IQUV$; unpolarised, linearly polarised and circularly polarised). They subsequently reconstructed magnetic maps using the more commonly used two Stokes profiles (IV) and again using all four. II Peg is plotted on Fig. 3.7 with black squares and diamonds indicating results obtained using Stokes $IQUV$ and Stokes IV respectively. Rosén et al. (2015) found that the toroidal and axisymmetric energy fractions are similar for both reconstructions though the maps constructed with Stokes $IQUV$ contained significantly more energy than the maps constructed from Stokes IV. The latter effect is unsurprising since one should expect more information to be reconstructed, and hence more fields, when using more data. The data points of Rosén et al. (2015) fall within the trend shown by the rest of the sample. II Peg follows this trend even though it is evolving off the main sequence whereas the rest of the sample are less evolved.

Further insights may be gained by splitting the axisymmetric energy into its poloidal and toroidal components. The top panel of Fig. 3.8 shows the fraction of poloidal energy that is axisymmetric, i.e. $E_{\text{mag}}(\alpha_{l,m=0}, \beta_{l,m=0})/E_{\text{mag}}(\alpha_{lm}, \beta_{lm})$, against the toroidal energy fraction. The bottom panel of Fig. 3.8 is similar but plots the fraction of toroidal energy that is axisymmetric, i.e. $E_{\text{mag}}(\gamma_{l,m=0})/E_{\text{mag}}(\gamma_{lm})$. The formatting is the same as that of Fig. 3.7. As before, the data points of Rosén et al. (2015) for II Peg are in agreement with the rest of the sample. It is clear that the poloidal and toroidal fields behave differently. While the axisymmetric poloidal energy does not show a clear trend, the axisymmetric toroidal energy does. The data show that toroidal fields are generated in a preferentially axisymmetric manner. This suggests that the toroidal field generation mechanism is sensitive to the rotation axis in a way that the poloidal field is not. Noticeably, there is a cluster of M dwarfs which have dipole dominated fields in the top left hand corner of the plot (these are also present in the top left of Fig. 3.7). Gastine et al. (2013) proposed that the strong dipolar component of these stars inhibits differential rotation and, hence, also the generation of strong toroidal fields through the Omega effect.

It is also useful to consider how the poloidal and toroidal fields are oriented with respect to each other. Figure 3.9 plots the fraction of poloidal energy that is axisymmetric against the fraction of toroidal energy that is axisymmetric, i.e. the ordinates of both panels in Fig. 3.8. The data points fill the entire available parameter space for this plot indicating that the poloidal and toroidal field orientations are not constrained by each other. Alternatively, their orientations may be related to each other but in a complex and non trivial way. It

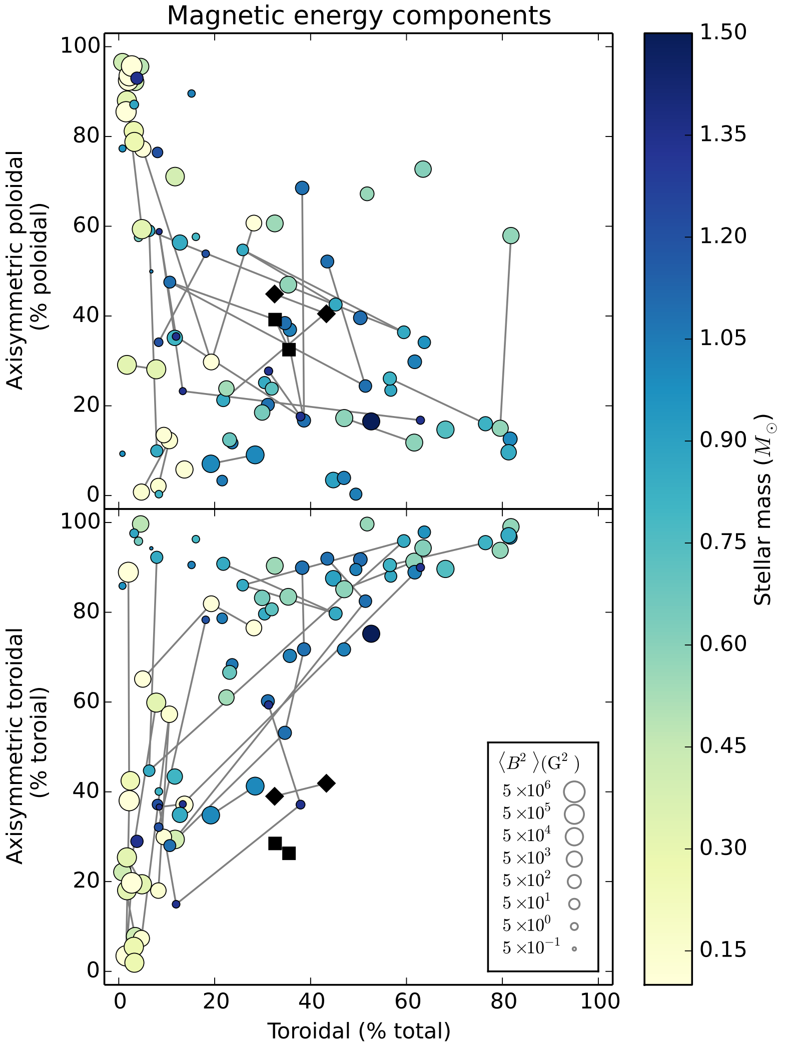

Figure 3.8: Axisymmetric poloidal energy as a percentage of total poloidal energy (top panel) and axisymmetric toroidal energy as a percentage of total toroidal energy (bottom panel) as a function of toroidal energy. Format is the same as Fig. 3.7

is particularly interesting that while the orientations of the poloidal and toroidal fields are uncorrelated, there is a relatively tight dependence of the toroidal energy density on the poloidal energy density (see Fig. 3.3).

3.4 Conclusion

Over the last decade, large strides have been made in characterising the strength, geometry and time evolution of cool star magnetic fields. Many stars display strong toroidal azimuthal bands, though currently there is no definitive explanation for their formation. In this chapter,

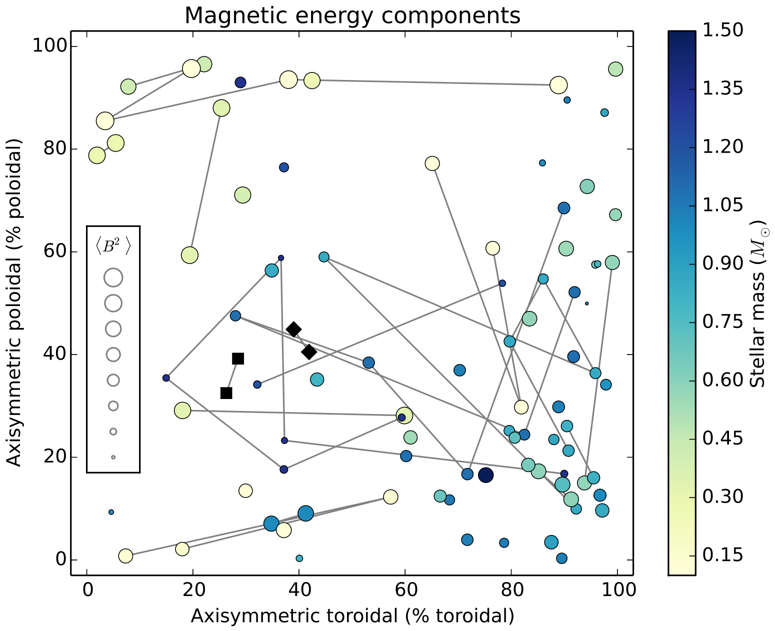

Figure 3.9: Axisymmetric poloidal energy as a percentage of total poloidal energy against axisymmetric toroidal energy as a percentage of total toroidal energy. Format is the same as Fig. 3.7. Similarly to Fig. 3.7, the inset shows $\langle B^2 \rangle$ values of 5×10^{-1}G^2 to 5×10^6G^2 in multiples of 10 for the smallest to biggest points. The numerical values are omitted due to lack of space.

an exploration of the strength and geometry of toroidal magnetic fields has been undertaken by analysing 55 stars that have had their surface magnetic fields mapped with ZDI. This is the first time toroidal fields have been studied in a large sample of stars. The results presented show clear constraints for future dynamo models and can be summarised as follows.

The sample shows that strong toroidal fields are strongly axisymmetric. Conversely, the orientation of poloidal fields are unconstrained with respect to the rotation axis. There is also evidence that the underlying dynamo type affects the relative strength of the poloidal and toroidal fields. Stars less massive than $0.5\,\mathrm{M}_\odot$ tend to have small toroidal energy fractions while more massive stars can have substantially higher toroidal energy fractions. Additionally, the toroidal field energies of the $\mathrm{M} > 0.5\,\mathrm{M}_\odot$ stars have a steeper power law dependence on the poloidal field energy than those of the $\mathrm{M} < 0.5\,\mathrm{M}_\odot$ stars. These results are in line with the results of Donati et al. (2008a), Morin et al. (2008b), Morin et al. (2010) & Gregory et al. (2012) who noted changes in magnetic properties at $0.5\,\mathrm{M}_\odot$, roughly coinciding with the fully convective limit. This suggests some link between the break in magnetic properties with the change in internal structure. These authors also note a strong break in the amount of differential rotation at $0.5\,\mathrm{M}_\odot$ with fully convective stars showing nearly solid body rotation. It is perhaps telling that the stars with the strongest toroidal fields are those that display differential rotation at their surface. On the other hand, the lowest mass stars, which do not have large toroidal energy fractions (see Fig. 3.3), display little to no differential rotation. This may be a hint that an Ω-effect, in the form of differential rotation, is responsible for generating axisymmetric toroidal fields. It would be interesting to compare these observational results to the theoretical dynamo simulations of Brown et al. (2010) and see if their axisymmetry and poloidal/toroidal energy fractions follow the same trends.

This study reveals that the latitude of the azimuthal bands depends, in part, on the stellar rotation period. On fast rotators, buoyant flux tubes feel a strong Coriolis force and are deflected polewards allowing flux emergence to occur at higher latitudes. Bands also exist at low to mid latitudes for all rotation periods. Therefore, rotation period cannot be the only parameter determining the latitude of flux emergence. However, at present, it is unclear what further parameters may be important.

Additionally, the poloidal and toroidal energies both follow the same qualitative behaviour with Rossby number. Both show saturation at low Rossby number with magnetic energies decreasing at higher Rossby number. This is also the qualitative behaviour that X-ray luminosity normalised to bolometric luminosity shows as a function of Rossby number, baring some quantitative differences such as the slope in the unsaturated regime. That the two field components behave similarly indicates that they share a common generation mechanism or that they are generated from each other. There is evidence that, in this sample, the $\mathrm{M} < 0.5\,\mathrm{M}_\odot$ stars correspond to stars in the saturated regime giving credence to the claim of Wright et al. (2011) that stars in the saturated and unsaturated regimes posses different dynamo mechanisms. However, it remains to be seen whether this is an effect of the bias in this sample. Future spectropolarimetric observations of cool stars with $\mathrm{Ro} \lesssim 0.1$, $\mathrm{M}_\star > 0.5\,\mathrm{M}_\odot$ will help confirm or disprove this hypothesis.

3.A Data tables

In this appendix, I present data tables relevant for the work in this chapter.

Table 3.1: Parameters of our sample: star ID, alternative name, stellar mass, rotation period, Rossby number, $\langle B^2 \rangle$ (which is proportional to the magnetic energy density), toroidal magnetic energy (as a percentage of total energy), axisymmetric magnetic energy (as a percentage of total energy), poloidal axisymmetric magnetic energy (as a percentage of poloidal energy), toroidal axisymmetric magnetic energy (as a percentage of toroidal energy) and the observation epoch. Similarly to Vidotto et al. (2014), we have grouped the stars into solar-like stars, young Suns, hot Jupiter hosts and M dwarfs. References indicate the paper where the magnetic map was originally published. For the remaining parameters, references can be found in Vidotto et al. (2014) and references therein.

Star ID	$M_\star$ [$M_\odot$]	$P_{\rm rot}$ [d]	Ro	$\log\left[\frac{\langle B^2\rangle}{G^2}\right]$	Tor [% total]	Axi [%total]	Pol Axi [%pol]	Tor Axi [%tor]	Obs epoch	Ref.
Solar-like stars										
HD 3651	0.88	43.4	1.916	1.19	3	87	87	98	-	2
HD 9986	1.02	23	1.621	-0.29	7	53	50	94	-	2
HD 10476	0.82	16	0.576	0.83	8	4	0	40	-	2
HD 20630	1.03	9.3	0.593	2.88	62	66	30	89	2012 Oct	6
HD 22049	0.86	10.3	0.366	2.27	8	16	10	92	2007 Jan	11
...	...	...	...	2.08	6	58	59	45	2008 Jan	11
...	...	...	...	2.50	59	72	36	96	2010 Jan	11
...	...	...	...	2.09	26	63	55	86	2011 Oct	11
...	...	...	...	2.63	45	59	43	80	2012 Oct	11
...	...	...	...	2.66	22	36	21	91	2013 Sep	11
HD 39587	1.03	4.83	0.295	2.71	47	36	4	72	-	2
HD 56124	1.03	18	1.307	0.79	15	90	90	91	-	2
HD 72905	1	5	0.272	3.03	82	81	13	97	-	2
HD 73350	1.04	12.3	0.777	2.26	49	44	0	90	-	2
HD 75332	1.21	4.8	>1.105	1.72	8	73	76	37	-	2
HD 78366	1.34	11.4	>2.781	2.35	4	91	93	29	-	2
HD 101501	0.85	17.6	0.663	2.28	30	42	25	80	-	2
HD 131156A	0.85	5.56	0.256	3.67	81	81	10	97	-	2
HD 131156B	0.72	10.3	0.611	2.60	32	42	24	81	-	2
HD 146233	0.98	22.7	1.324	0.29	1	9	9	5	2007 Aug	4
HD 166435	1.04	3.43	0.259	2.73	36	49	37	70	-	2
HD 175726	1.06	3.92	0.272	2.13	24	25	12	68	-	2
HD 190771	0.96	8.8	0.453	2.38	64	75	34	98	-	2
HD 201091A	0.66	34.2	0.786	1.05	4	59	58	96	-	2
HD 206860	1.1	4.55	0.388	2.88	50	66	40	92	-	2
...	...	...	...	2.59	43	69	52	92	2007 Jul	14
...	...	...	...	2.42	51	54	24	82	2008 Aug	14
...	...	...	...	2.21	11	45	48	28	2009 Jun	14
...	...	...	...	2.67	35	44	38	53	2010 Jul	14
...	...	...	...	2.67	39	38	17	72	2011 Jul	14
...	...	...	...	2.81	38	77	69	90	2013 Jul	14
Young Suns										
Ab Doradus	0.76	0.5	0.026	4.92	28	18	9	41	2001 Dec	6
...	...	...	...	4.72	19	12	7	35	2002 Dec	6
BD-16 351	0.9	3.39	-	3.76	45	41	3	88	2012 Sep	7
HD 106506	1.5	1.39	>0.024	4.51	53	47	17	75	2007 Apr	8
HII 296	0.8	2.61	-	3.62	12	36	35	43	2009 Oct	7
HII 739	1.08	2.7	-	2.60	31	33	20	60	2009 Oct	7
HIP 12545	0.58	4.83	-	4.35	35	60	47	83	2012 Sep	7
HIP 76768	0.61	3.64	-	4.17	63	86	73	94	2013 May	7
TYC0486-4943-1	0.69	3.75	-	2.99	23	25	12	67	2013 Jun	7
TYC5164-567-1	0.85	4.71	-	3.59	13	54	56	35	2013 Jun	7
TYC6349-0200-1	0.54	3.39	-	3.67	22	32	24	61	2013 Jun	7
TYC6878-0195-1	0.65	5.72	-	3.68	30	38	19	83	2013 Jun	7

Table 3.1: continued...

Star ID	$M_\star$ [$M_\odot$]	$P_{\rm rot}$ [d]	Ro	$\log\left[\frac{\langle B^2\rangle}{G^2}\right]$	Tor [% total]	Axi [%total]	Pol Axi [%pol]	Tor Axi [%tor]	Obs epoch	Ref.
Hot Jupiter hosts										
τ Boo	1.34	3	>0.732	1.00	63	63	17	90	2008 Jan	8
...	...	...	...	0.70	8	57	59	37	2008 Jun	8
...	...	...	...	0.45	13	25	23	37	2008 Jul	8
...	...	...	...	0.85	12	33	35	15	2009 May	9
...	...	...	...	1.19	38	25	18	37	2010 Jan	9
...	...	...	...	1.02	31	38	28	59	2011 Jan	9
HD 46375	0.97	42	2.34	0.70	1	77	77	86	2008 Jan	9
HD 73256	1.05	14	0.962	1.74	22	20	3	79	2008 Jan	9
HD 102195	0.87	12.3	0.473	2.22	57	60	23	88	2008 Jan	9
HD 130322	0.79	26.1	0.782	0.81	16	64	58	96	2008 Jan	9
HD 179949	1.21	7.6	>1.726	0.83	18	58	54	78	2007 Jun	12
...	...	...	...	1.13	8	34	34	32	2009 Sep	12
HD 189733	0.82	12.5	0.403	2.69	57	62	26	91	2007 Jun	13
...	...	...	...	3.10	76	77	16	96	2008 Jul	13
M dwarf stars										
GJ 569A	0.48	14.7	<0.288	4.17	5	96	96	100	2008 Jan	14
GJ 410	0.58	14	<0.267	4.10	82	92	58	99	2007 Jan	14
...	...	...	...	4.02	80	78	15	94	2007 Dec	14
GJ 182	0.75	4.35	0.054	4.60	68	66	15	90	2007 Jan	14
GJ 49	0.57	18.6	<0.352	2.94	52	84	67	100	2007 Jul	14
GJ 388	0.42	2.24	0.047	4.77	1	96	97	22	2007 Jan	15
...	...	...	...	4.75	3	89	92	8	2008 Jan	15
GJ 494A	0.59	2.85	0.092	4.44	62	61	12	91	2007 Jan	14
...	...	...	...	4.51	47	49	17	85	2007 Dec	14
GJ 896 A	0.39	1.06	0.02	5.31	12	66	71	29	2006 Aug	15
GJ 896 B	0.25	0.4	0.005	5.35	2	92	93	42	2006 Aug	15
GJ 873	0.32	4.37	0.068	5.61	8	31	28	60	2006 Aug	15
...	...	...	...	5.48	2	29	29	18	2007 July	15
GJ 1111	0.1	0.46	0.005	4.14	5	77	77	65	2007	16
...	...	...	...	3.85	19	40	30	82	2008	16
...	...	...	...	3.83	28	65	61	77	2009	16
GJ 1156	0.14	0.49	0.005	3.71	8	3	2	18	2007	16
...	...	...	...	4.21	11	17	12	57	2008	16
...	...	...	...	4.05	5	1	1	7	2009	16
GJ 1245B	0.12	0.71	0.007	4.59	14	10	6	37	2006	16
...	...	...	...	3.72	9	15	13	30	2008	16
GJ 9520	0.55	3.4	0.097	4.38	33	70	61	90	2008 Feb	14
V374 Peg	0.28	0.45	0.006	5.75	3	79	81	5	2005 Aug	17
...	...	...	...	5.61	3	76	79	2	2006 Aug	17
GJ 412B	0.1	0.78	0.008	6.16	2	92	92	89	2006	16
...	...	...	...	6.35	2	92	94	38	2007	16
...	...	...	...	6.34	2	84	86	3	2008	16
...	...	...	...	6.56	3	94	96	20	2009	16
GJ 285	0.32	2.77	0.04	5.72	5	57	59	19	2007 Jan	15
...	...	...	...	5.66	2	87	88	25	2008 Jan	15

1: Petit et al. (2015); 2: do Nascimento et al. (2014); 3: Jeffers et al. (2014); 4: Petit et al. (2008); 5: Boro Saikia et al. (2015); 6: Donati et al. (2003b); 7: Folsom et al. (2016); 8: Waite et al. (2011); 9: Marsden et al. (2011); 10: Fares et al. (2009); 11: Fares et al. (2013); 12: Fares et al. (2012); 13: Fares et al. (2010); 14: Donati et al. (2008a); 15: Morin et al. (2008b); 16: Morin et al. (2010); 17: Morin et al. (2008a)

Table 3.2: Numerical values for Fig. 3.6. For each star the rotation period, latitude of the band and the full-width half-maximum of the band are listed.

Star ID	P_{rot} [d]	Latitude [degrees]	FWHM [degrees]	Star ID	P_{rot} [d]	Latitude [degrees]	FWHM [degrees]
HD 3651	43.4	16.9	47.8	TYC5164-567-1	4.71	64.7	21.1
HD 9986	23	22.5	47.8	TYC6349-0200-1	3.39	73.1	14.1
HD 10476	16	47.8	35.2	τ Boo (2009 May)	3	64.7	25.3
HD 20630	9.3	25.3	40.8	τ boo (2010 Jan)	3	30.9	25.3
HD 22049 (2007 Jan)	10.3	42.2	42.2	HD 46375	42	33.8	42.2
HD 22049 (2010 Jan)	10.3	33.8	49.2	HD 73256	14	16.9	47.8
HD 22049 (2011 Oct)	10.3	36.6	42.2	HD 102195	12.3	39.4	42.2
HD 22049 (2012 Oct)	10.3	33.8	49.2	HD 130322	26.1	16.9	49.2
HD 22049 (2013 Oct)	10.3	36.6	46.4	HD 179949 (2009 Sep)	7.6	59.1	25.3
HD 39587	4.83	22.5	42.2	HD 189733 (2007 Jun)	12.5	2.8	43.6
HD 56124	18	47.8	35.2	HD 189733 (2008 Jul)	12.5	5.6	52
HD 72905	5	25.3	40.8	GJ 569A	14.7	30.9	39.4
HD 73350	12.3	14.1	45	GJ 410 (2007 Jan)	14	28.1	47.8
HD 78366	11.4	53.4	42.2	GJ 410 (2007 Dec)	14	28.1	46.4
HD 101501	17.6	16.9	47.8	GJ 182	4.35	14.1	32.3
HD 131156A	5.56	36.6	47.8	GJ 49	18.6	45	38
HD 131156B	10.3	47.8	35.2	GJ 388 (2007 Jan)	2.24	36.6	32.3
HD 166435	3.43	16.9	32.3	GJ 494A (2007 Jan)	2.85	25.3	45
HD 175726	3.92	59.1	22.5	GJ 494A (2007 Dec)	2.85	42.2	47.8
HD 190771	8.8	33.8	39.4	GJ 896 A	1.06	59.1	23.9
HD 201091	34.2	30.9	45	GJ 896 B	0.4	75.9	12.7
HD 206860	4.55	25.3	39.4	GJ 873 (2007 July)	4.37	53.4	15.5
HD 206860 (2007 Jul)	4.6	36.6	57.7	GJ 1111 (2007)	0.46	19.7	28.1
HD 206860 (2008 Aug)	4.6	8.4	32.3	GJ 1111 (2008)	0.46	19.7	42.2
HD 206860 (2010 Jul)	4.6	8.4	25.3	GJ 1156 (2007)	0.49	25.3	30.9
HD 206860 (2011 Jul)	4.6	8.4	53.4	GJ 1156 (2009)	0.49	39.4	16.9
HD 206860 (2013 Jul)	4.6	14.1	50.6	GJ 9520	3.4	42.2	30.9
HD 106506	1.39	61.9	19.7	GJ 1245B (2006)	0.71	14.1	25.3
HII 296	2.61	16.9	23.9	GJ 1245B (2008)	0.71	45	38
HII 739	2.7	56.2	18.3	GJ 412B (2006)	0.78	25.3	28.1
HIP 12545	4.83	59.1	38	GJ 412B (2009)	0.78	19.7	19.7
HIP 76768	3.64	64.7	25.3	GJ 285 (2008 Jan)	2.77	33.8	38
TYC0486-4943-1	3.75	5.6	42.2				

4

The connection between stellar activity cycles and magnetic field geometry

This chapter is based on the work presented in See et al. (submitted).

4.1 Introduction

4.1.1 Solar and stellar activity cycles

On the Sun, tracers of magnetic activity are known to vary cyclically (Hathaway, 2015). One of the most obvious manifestations of the solar cycle is the behaviour of sunspots as they emerge on the photosphere. Long term observations show that sunspots appear in two latitude bands, symmetric about the equator, at roughly ±30°. Over the course of a solar cycle, these bands migrate towards the equator forming the so called butterfly diagram (top of Fig. 4.1). Additionally, the fractional sunspot coverage of the visible disc varies periodically, with successive minima occurring $\sim$11 years apart (bottom of Fig. 4.1).

Similar activity cycles are also thought to exist in other stars with outer convection zones.

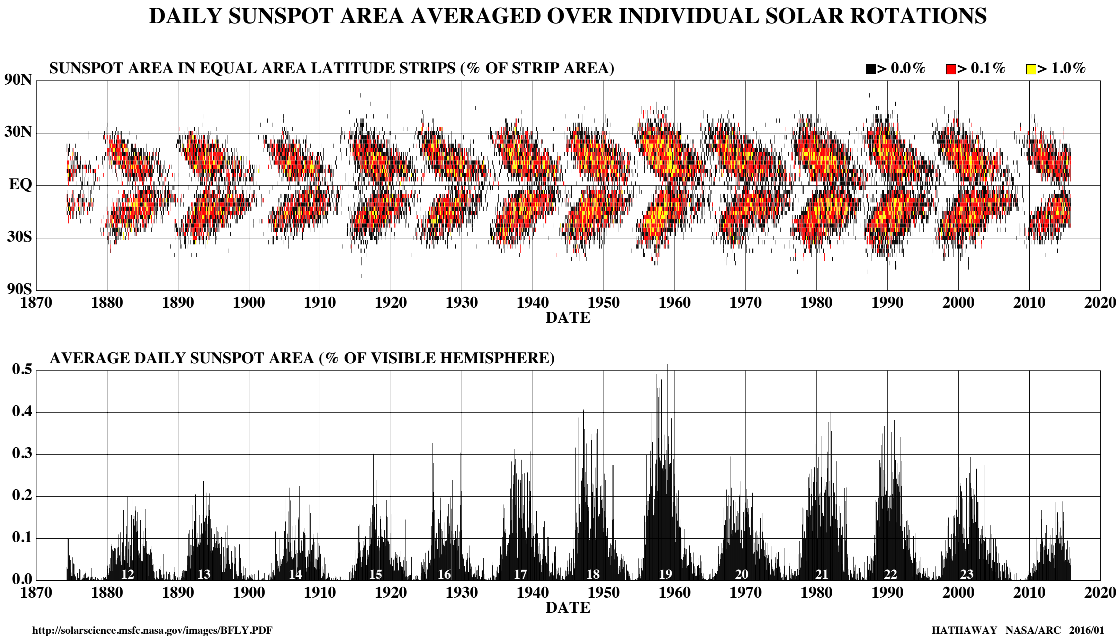

Figure 4.1: The sunspot record since 1874 as collected by the Royal Greenwich Observatory. Top: the latitude of sunspots is plotted as a function of time. The spots appear in two bands that move towards the equator as the solar cycle progresses forming the so called butterfly diagram. Bottom: the percentage of the visible hemisphere of the Sun that is covered in sunspots as a function of time. Both panels show that sunspots behave periodically with a time-scale of ~11 years. Image used from NASA in accordance with their media usage guidelines.

However, it is not possible to count starspots since stellar discs are spatially unresolved. One option is to measure the disc integrated emission in calcium lines as a function of time. Since sun/starspots are magnetic in nature and Ca II H & K emissions are known to increase with increasing magnetic field strength (Schrijver et al., 1989), Ca II H & K emissions can be used as a proxy for starspot coverage.

In this regard, the Mount wilson Observatory has played an instrumental role in advancing knowledge of stellar cycles via multi-decade chromospheric observations of Solar-like stars (Wilson, 1978; Baliunas et al., 1995). In particular, it is responsible for identifying activity cycles on numerous stars and measuring their periods. Further observational campaigns have since been conducted, building on the work done at the Mount Wilson Observatory (e.g. Hall et al., 2007). Various studies into the behaviour of chromospheric activity have resulted from these campaigns including chromospheric and photometric variability (Lockwood et al., 2007) and the use of activity proxies as age indicators (Mamajek & Hillenbrand, 2008; Pace, 2013).

One intriguing avenue of investigation that has emerged is the relationship between the activity cycle period and various other stellar parameters. Brandenburg et al. (1998) and Saar & Brandenburg (1999) suggested that stars lie on several branches when the ratio of their cycle frequency to the angular rotational frequency, $\omega_{\rm cyc}/\Omega$, is plotted against inverse Rossby number, $\mathrm{Ro}^{-1} = \tau/P_{\rm rot}$, where τ is the convective turnover time and $P_{\rm rot}$ is the rotation period. It appears that the most rapidly rotating stars exist on the so called "superactive" branch before transitioning onto the "active" and "inactive" branches as they age and spin down. Subsequent literature, e.g. Böhm-Vitense (2007), has focused on the active and inactive branches. This author noted that stars on the active and inactive branches undergo a roughly fixed number of rotation periods per activity cycle period but that this number was different for the two branches; $P_{\rm cyc} \sim 400 P_{\rm rot}$ along the active branch and $P_{\rm cyc} \sim 90 P_{\rm rot}$ along the inactive branch.

4.1.2 Solar and stellar magnetic cycles

Fundamentally, the solar cycle exists because of the underlying dynamo. Over the course of a cycle, the Sun's magnetic field changes from poloidal to toroidal via an Ω-effect and then back to poloidal via an α-effect (Charbonneau, 2010, see section 1.2). While the physical mechanisms behind the Ω- and α-effects are not precisely known, it seems likely that the interface between the radiative core and convective outer layer, known as the tachocline, is the dominant source of azimuthal shear required by the Ω-effect.

Although the tachocline is thought to be the dominant source of shear in the Sun, studies have shown that a tachocline is not required in order to generate organised large-scale magnetic fields (Brown et al., 2010). Indeed Böhm-Vitense (2007) suggests that the reason multiple branches exist is due to different dynamos operating along each branch. Under this interpretation, the tachocline is the main source of shear on inactive branch stars and the near-surface shear layer is the main source of shear in active branch stars.

As well as sunspots, another physical manifestation of the solar dynamo and cycle is the periodic polarity flips that the global magnetic field undergoes. As shown in Fig. 4.2, the solar dipole component switches polarity roughly every 11 years. After $\sim$22 years, the Sun has undergone two such polarity flips to return to its original magnetic configuration. Therefore, on the Sun, the magnetic cycle comprises two 11 year activity cycles as measured in activity tracers such as Ca II emission.

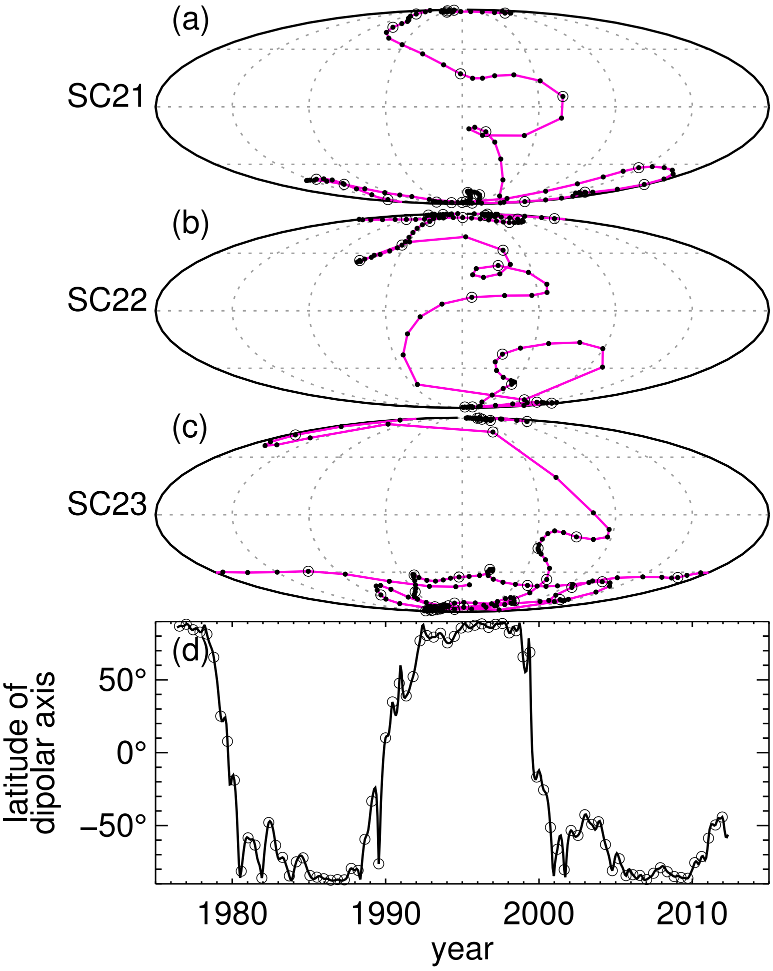

Figure 4.2: Panel (a) - (c): the axis of the dipole component of the solar magnetic field is plotted for solar cycles 21-23. Panel (d): The latitude of the dipole axis is plotted as a function of time. The solar magnetic dipole is mostly aligned or anti-aligned with the solar rotation axis. However, roughly every 11 years, it undergoes a polarity flip in a comparatively short amount of time. Figure reproduced from DeRosa et al. (2012) with permission, ©AAS.

Using Zeeman-Doppler imaging (ZDI; see section 1.3.2), polarity flips have also been seen in other stars such as HD 78366 (Morgenthaler et al., 2011) or 61 Cyg A (Boro Saikia et al., submitted). As mentioned in section 1.4.3, τ Boo is the most well-studied star in terms of magnetic cycles. Fares et al. (2009) determine that the most likely magnetic cycle period for this star is either 8 months or 2 years, i.e. polarity flips occurring every 4 months or 1 year.

Reconstructing the magnetic field using ZDI is a useful way of studying magnetic cycles, as τ Boo has demonstrated. However, due to the amount of observation time required to reconstruct even just one map, determining the magnetic field topology of a star over its entire cycle is a lengthy and difficult task. Consequently, most stars that have been mapped with ZDI, have only been mapped during one epoch. On the other hand, individual maps still provide useful information (see section 1.4), that can be used to learn about the activity cycles of stars.

In this chapter, I assemble a sample of stars that have a chromospherically determined activity cycle period as well as at least one ZDI map. I will discuss the magnetic properties of the sample, focusing on the magnetic topologies of stars along the active and inactive branches. Due to the relatively small size of this sample, I will also discuss previous magnetic activity and ZDI studies to give greater context to this work. In section 4.2, I present the sample of stars used. In section 4.3, I consider the sample within the context of previous studies. A discussion of the results and their implications is presented in section 4.4 with conclusions following up in section 4.5.

4.2 Sample selection

The sample used in this study consists of stars that have both a magnetic map determined from ZDI and a chromospherically determined cycle period in the literature. Their physical parameters are listed in table 4.1. Figure 4.3 shows the rotation periods (between 3 and 45 days) and masses (between $0.6\,\mathrm{M}_\odot$ and $1.4\,\mathrm{M}_\odot$) of the sample. Stars in this mass range are thought to have solar-like internal structures, i.e a radiative core and outer convection zone (van Saders & Pinsonneault, 2012). To calculate Rossby numbers, I use the rotation periods as listed by Vidotto et al. (2014) and convective turnover times were calculated using the method described by Saar & Brandenburg (1999). Values for the X-ray luminosity normalised to the bolometric luminosity, $R_\mathrm{X} = L_\mathrm{X}/L_\mathrm{bol}$, are taken from Vidotto et al. (2014) and references therein.

As well as a reconstruction of the overall magnetic field at the stellar surface, different components of the field can also be recovered by ZDI as described in section 2.2.2. In this chapter, I will focus on the magnetic energy density averaged over the stellar surface, $\langle B^2 \rangle$, the toroidal energy fraction, $f_\mathrm{tor} = \langle B^2_\mathrm{tor} \rangle / \langle B^2 \rangle$, the axisymmetric energy fraction, $f_\mathrm{axi} = \langle B^2_\mathrm{axi} \rangle / \langle B^2 \rangle$ and the axisymmetric fraction of the poloidal component only, $f_\mathrm{axi,pol} = \langle B^2_\mathrm{axi,pol} \rangle / \langle B^2_\mathrm{pol} \rangle$. The original paper that each ZDI map is published in is listed in table 4.1.

A large number of the chromospheric cycle determinations come from Baliunas et al. (1995) though some come from other sources, the references for which are listed in table

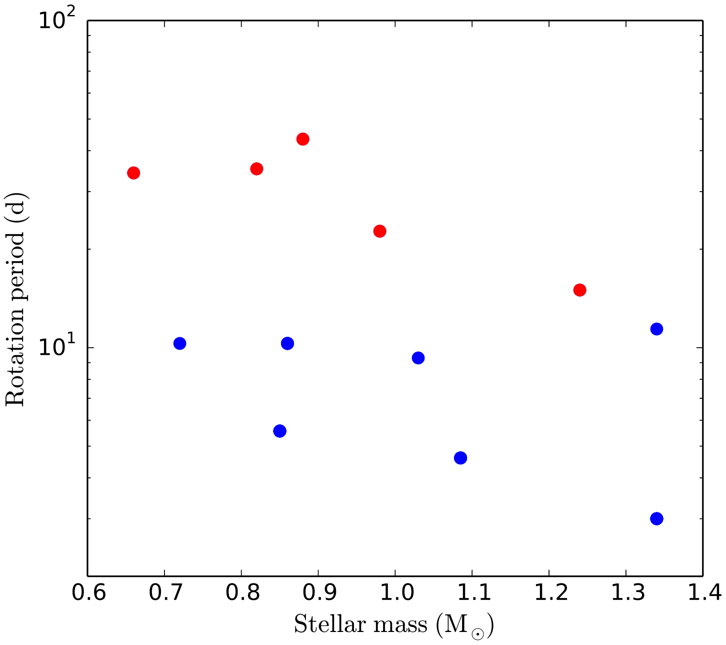

Figure 4.3: The rotation periods and masses of the stars presented in table 4.1. Blue and red markers correspond to stars on the active and inactive branches respectively (see section 4.3).

4.1. I have included a number of cycle periods that have been classified as 'poor' or 'fair' by Baliunas et al. (1995) under their false alarm probably grading scheme in order to improve the number of objects in this study (these are noted in table 4.1). Accordingly, when interpreting the results, these objects may need to be treated more cautiously. However, they do not seem to be discrepant with the rest of the sample. I discuss some individual cases here:

61 Cyg A: 61 Cyg A is a mature K dwarf with a well known chromospheric activity cycle of approximately 7 years (Baliunas et al., 1995). From observations taken at the NARVAL spectropolarimeter on the Telescope Bernard Lyot, together with old archival data, Boro Saikia et al., (submitted) determine a chromospheric cycle of 7.2±1.3 years which is also in agreement with the long cycle found by Oláh et al. (2009). Oláh et al. (2009) also found a secondary chromospheric period of 3.6 years in part of their data. However, Boro Saikia et al., (submitted) find no evidence of this shorter period and so we will only use the 7.2 year period. 61 Cyg A is also known to exhibit an X-ray activity cycle which is in phase with the chromospheric activity cycle (Robrade et al., 2012). Long term spectropolarimetric monitoring of this star has also revealed a solar-like magnetic cycle (Boro Saikia et al. submitted), which makes it the first cool star apart from the Sun where the magnetic and activity cycles are in phase.

τ **Boo**: Baliunas et al. (1995) found a 11.6 year period but assign it a poor grade in their false alarm probably classification scheme calling into question the reliability of this period determination. However, I still include this object in the sample since it is interesting in the context of magnetic activity cycles (see section 4.4.2). Additionally, Baliunas et al. (1997) and Mengel et al. (2016) both report a chromospheric cycle period of around 116 days.

HN Peg: This star was also assigned a poor grade by Baliunas et al. (1995) who found a period of 6.2 years. Messina & Guinan (2002) found a 5.5 year period from an analysis based on photometric data and I use this value due to the smaller false alarm probability that these authors find. Both values are compatible with the inactive branch of stars.

4.3 Results

4.3.1 Field properties

In Fig. 4.4a, I plot the magnetic properties of the sample of stars used in chapter 3 in stellar mass-rotation period space similarly to Fig. 3 of Donati & Landstreet (2009, also see Fig. 1.5). The symbol colour scales with the poloidal energy fraction, $f_{\rm pol} = 1 - f_{\rm tor}$, and the symbol shape scales with the axisymmetry of the poloidal component, $f_{\rm axi,pol}$. Numerous authors have used this method of representing magnetic field characteristics in various different parameter spaces (Donati et al., 2008a; Morin et al., 2008b; Donati & Landstreet, 2009; Morin et al., 2010; Vidotto et al., 2016; Folsom et al., 2016). Usually, the symbol size scales with $\log\langle B^2\rangle$ on this type of plot. However, due to the large number of stars in this sample, I have chosen not to do so here for clarity. For stars with multiple ZDI maps, I have only plotted the epoch with the largest $f_{\rm tor}$ value. Additionally, I have restricted the parameter space to stars more massive than $0.5{\rm M}_\odot$ since less massive stars likely have different dynamo mechanisms to the stars I analyse in this study (Donati et al., 2008a; Morin et al., 2008b, 2010; Gregory et al., 2012). As outlined by Donati & Landstreet (2009), the Rossby number is important in the context of magnetic field topologies. A clear transition at a Rossby number of $\sim$1 (dotted line) can be seen in the field topologies. Stars with Ro $\gtrsim$ 1 (top right of plot) mostly show dominantly poloidal and axisymmetric fields whereas Ro $\lesssim$ 1 stars (bottom left of plot) are capable of generating significant or even dominantly toroidal fields that are non-axisymmetric.

In the context of stellar activity, the preference of Rossby number over rotation period alone is motivated from both empirical (Wright et al., 2011, see also section 3.3.2) and the-

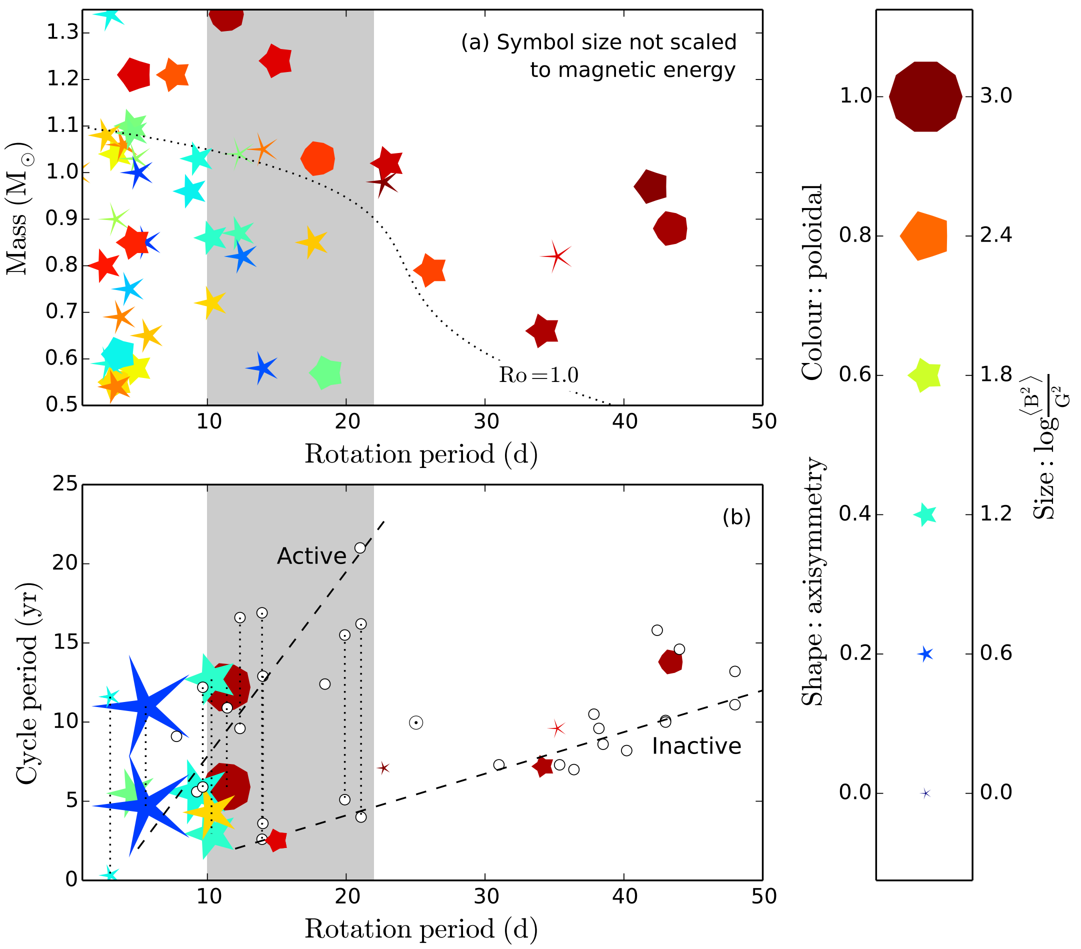

Figure 4.4: Panel a: the sample of stars used in chapter 3 plotted in stellar mass-rotation period space. This is a similar plot to Fig. 3 of Donati & Landstreet (2009). The symbol colour represents the toroidal energy fraction (ranging from red for purely poloidal, i.e. $f_{\text{pol}} = 1$, to blue for purely toroidal, i.e. $f_{\text{pol}} = 0$) and symbol shape represents how axisymmetric the poloidal component of the field is (ranging from decagons for a purely axisymmetric poloidal field, i.e. $f_{\text{axi,pol}} = 1$, to pointed stars for a purely non-axisymmetric field, i.e. $f_{\text{axi,pol}} = 0$). Due to the large number of stars in the sample, symbol sizes have been kept the same for clarity and do not scale with $\log\langle B^2 \rangle$ as is usual with this type of plot. A dotted line indicates Ro = 1. Panel b: chromospheric activity cycle period against rotation period for the sample of Böhm-Vitense (2007) plotted with open circles (see their Fig. 1). Dashed lines indicate the active and inactive branches. Overplotted is the sample outlined in section 4.2 where symbol colour and shape have the same meaning as panel a. In this panel, symbol size does scale with $\log\langle B^2 \rangle$ as indicated by the key. Stars with multiple cycle periods are connected with a dashed line. On both panels the shaded region indicates the range of rotation periods where the active and inactive branches overlap.

oretical considerations (Noyes et al., 1984). In Fig. 4.5a, I plot the toroidal energy fraction, f_{tor}, of the sample from table 4.1 directly against Rossby number with red and blue circles (these colours correspond to inactive and active branch stars respectively; see section 4.3.3).

Stars that have been observed at multiple epochs are connected by solid lines. Additionally, I also plot the stars in the larger sample used in chapter 3 with open square markers. This plot is similar to Fig. 6 of Petit et al. (2008, also see Fig. 1.7). These authors studied four stars that were roughly one solar mass each and showed that the poloidal energy fraction, $f_{\rm pol}$, increases with rotation period. A similar behaviour is seen here whereby the stars with the longest rotation periods (largest Ro) display dominantly poloidal fields. Conversely, the most rapidly rotating stars (smallest Ro) show large $f_{\rm tor}$ variations and are capable of developing dominantly toroidal fields. As in Fig. 4.4a, the transition between these two regimes occurs at Ro $\sim$ 1.0. This behaviour has also been noted by Donati & Landstreet (2009) and Folsom et al. (2016). Comparing with the expanded sample in Fig. 4.5a, the four stars of Petit et al. (2008) trace the upper envelope of points shown here.

4.3.2 Activity-rotation relation

Another tracer of magnetic activity is coronal X-ray emission. The relationship between the ratio of X-ray to bolometric luminosity, $R_{\rm X} = L_{\rm X}/L_{\rm bol}$ and Rossby number is known as the activity-rotation relation and is well studied (Noyes et al., 1984; Pizzolato et al., 2003; Wright et al., 2011). As discussed in section 3.3.2, stars in the so-called unsaturated regime show increasing $R_{\rm X}$ values with decreasing Rossby number until a critical Rossby number of Ro $\sim$ 0.1. At smaller Rossby numbers, in the so called saturated regime, X-ray emissions saturate at roughly $R_{\rm X} \sim 10^{-3}$. Recent studies have shown that the energy stored in large-scale magnetic fields also display the same behaviour as $R_{\rm X}$, separating into the saturated and unsaturated regimes (Vidotto et al., 2014, chapter 3). In Fig. 4.5b, I plot $R_{\rm X}$ against Rossby number for both the sample from this chapter (red and blue markers) and the sample of Wright et al. (2011) (grey dots) for context. The coloured points lie in the unsaturated regime of the activity-rotation relation. Interestingly, there is no break in the activity-rotation relation at Ro $\sim$ 1.0 as there is for $f_{\rm tor}$. Given that magnetic field generation and coronal X-ray emission are both a result of dynamo activity, this is perhaps surprising.

4.3.3 Activity cycle branches

Many studies have examined the possibility that activity cycle periods may lie on multiple branches. Brandenburg et al. (1998) and Saar & Brandenburg (1999) investigated this phe-

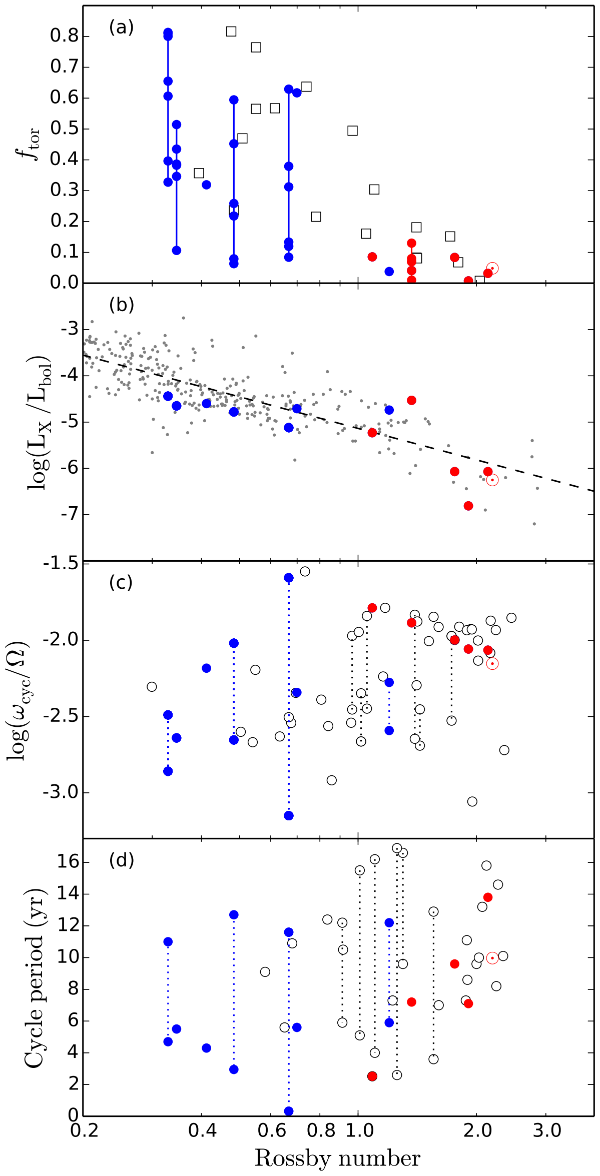

Figure 4.5: Panel a: toroidal energy fraction against Rossby number for the sample of stars used chapter 3 (open square symbols). Stars observed at multiple epochs are joined by solid lines. Panel b: the ratio of X-ray to bolometric luminosity against Rossby number reproduced from Wright et al. (2011) (grey dots; see their Fig. 2). Panel c: the ratio of chromospheric cycle frequency to rotational frequency against Rossby number reproduced from Saar & Brandenburg (1999) (open circle symbols; see their Fig. 1). Panel d: chromospheric cycle period against Rossby number using the sample of Böhm-Vitense (2007). In panels c and d, stars with multiple cycles are connected by dashed lines. In each panel, the sample presented in table 4.1 is plotted with blue and red circles denoting active and inactive branch stars respectively.

nomenon in the $\omega_{\rm cyc}/\Omega$ vs $\rm Ro^{-1}$ parameter space[1]. These authors suggested that a given star can lie on one of two branches, or on both if it has two cycle periods, and labelled these branches as ‘active’ or ‘inactive’. In Fig. 4.5c, I reproduce Fig. 1 of Saar & Brandenburg (1999) with open circle markers. Stars with two cycle period determinations are joined with a dashed line. It is worth noting that this plot is reversed compared with the plot of Saar & Brandenburg (1999) because I have plotted against Rossby number rather than inverse Rossby number. I over plot the sample from table 4.1 using red and blue circles to represent stars on the inactive and active branches respectively. The decision of which branch a given star is assigned to is made by eye based on their position in $\omega_{\text{cyc}}/\Omega$ vs Ro space. This colour scheme is also used for Figs. 4.5a and 4.5b. Saar & Brandenburg (1999) also discuss the possibility of a third branch of very rapid rotators (Ro $\lesssim 0.1$). Since the sample used in this work lacks Ro $\lesssim 0.1$ stars, I will not consider this branch in the current analysis.

---

[1] Saar & Brandenburg (1999) use an alternative Rossby number definition to the one given here; $\rm Ro_{SB} = \mathit{P}_{rot}/4\pi\tau = Ro/4\pi$. In this chapter, I will use the definition outlined in the main body of text, i.e. $P_{\rm rot}/\tau$, and convert values quoted by Saar & Brandenburg (1999) to this definition when necessary.

Böhm-Vitense (2007) also considered the possibility that activity cycle periods may lie on multiple branches. This author studied the stars from Baliunas et al. (1995) with the most reliable chromospheric cycle period determinations. I reproduce their plot of cycle period against rotation period with open circles in Fig. 4.4b (c.f. with Fig. 1 of Böhm-Vitense (2007)) with the sample from this work overplotted. The symbol colour and shape have the same format as Fig. 4.4a. Additionally the symbol sizes scale with $\log\langle B^2\rangle$ unlike in Fig. 4.4a.

Böhm-Vitense (2007) deliberately chose to avoid special numbers from dynamo theory, including the Rossby number in her study. However, given the importance of this parameter to magnetic topologies and activity, it also worth investigating how it affects activity cycle periods. Fig. 4.5d shows the sample of Böhm-Vitense (2007) plotted in activity cycle period-Rossby number space (open circles). Additionally the sample of table 4.1 is also plotted in red and blue circles. These colours have the same meaning as in the rest of Fig. 4.5. The inactive branch can be seen as a sequence extending down the right hand side of the plot (most easily seen by following the red points). The active branch is less obvious but can still be seen in this plot.

4.4 Discussion

4.4.1 Large-scale field geometry along activity branches

Fig. 4.4b shows that all the inactive branch stars are strongly poloidal while the active branch stars can have strong toroidal fields. This is also evident from Fig. 4.5a where the inactive stars (red circles) are all dominantly poloidal while the active branch stars (blue markers) show large f_{tor} variations. In Fig. 4.4b, the active branch star, HD 78366, look as if it might be discrepant due to its strongly poloidal fields. However, this star has only been observed at one epoch. Without further observations, it is not possible to tell whether it is truly discrepant or whether it was just coincidentally observed during a part of the its cycle when it was in a poloidal state. I therefore propose the hypothesis that stars on the two branches have distinct magnetic field topologies - dominantly poloidal fields on the inactive branch while active branch stars display significant toroidal fields with large temporal variations in the toroidal energy fraction. I will discuss potential problems with this hypothesis in section 4.4.3.

Given that there are only five inactive stars, four of which have only been observed during one epoch each, one might question whether these stars would display large f_{tor} variations over a cycle. However, 61 Cyg A has been observed at five epochs over the course of its seven year cycle and showed minimal f_{tor} variations (Boro Saikia et al., submitted). This suggests that inactive branch stars remain largely poloidal even after considering activity cycle variations.

An explanation for the differing magnetic topologies on each branch may lie in the dynamos of these stars. It is thought that strong shearing, i.e. an Ω-effect, can generate toroidal field from a poloidal field. Böhm-Vitense (2007) propose that the dominant shear layer for inactive branch stars is the interface between the radiative core and the outer convective layer, i.e. the tachocline, while rotational shear in near surface layers is dominant for the active branch stars. For stars with periods on both branches, both shear layers would contribute significantly. Since the tachocline lies at a greater fractional depth, flux generated there takes longer to rise and emerge at the stellar surface. In contrast, flux generated in near surface shear layers takes less time and is more likely to emerge in a stressed or toroidal state. This may explain why it is only the active branch stars that are able to possess dominantly toroidal fields. Under this interpretation, one would expect stars with cycle periods on both branches to display large f_{tor} variations throughout their cycles since both shear layers would be contributing to dynamo action. This is the behaviour shown by ϵ Eri and τ Boo, which are the only two stars that has been mapped by ZDI that have cycle periods on both branches. However, there is evidence from helioseismology that the opposite is true in the Solar case (Broomhall et al., 2012), i.e. that the longer/shorter cycle period should be attributed with the tachocline/near surface shear layer. Metcalfe et al. (2013) speculates that the rotational history of Sun makes it an outlier while the preliminary analysis of do Nascimento et al. (2015) suggests that the Sun might be part of a previously unrecognised branch.

Further insight can be gained from the observations by comparing Figs. 4.4a and 4.4b. These figures are split into three regions as indicated by the shaded background. To the left of the shaded region, only active branch stars are found. Conversely, to the right of the shaded region, all the stars lie on the inactive branch. These regions correspond to $P_{\rm rot} \lesssim 10$ days and $P_{\rm rot} \gtrsim 22$ days. Within the shaded region, the active and inactive branches overlap. Looking at Fig. 4.4a, the shape of the $\rm Ro = 1$ curve in stellar mass-rotation period space dictates the magnetic geometry along each of the branches. To the right of the shaded region, most of the stars have $\rm Ro \gtrsim 1$ and hence are dominantly poloidal explaining why poloidal stars are found on the inactive branch. Conversely, to the left of the shaded region, most of the stars have $\rm Ro \lesssim 1$ and hence are capable of generating strong toroidal fields explaining the toroidal stars found on the inactive branch. In the intermediate region, a mix of $\rm Ro \gtrsim 1$ and $\rm Ro \lesssim 1$ stars are found and hence a mix of poloidal and toroidal stars. These may correspond to stars on the inactive and active branches respectively though currently, it is not possible to tell due to the lack of stars with both a ZDI map and a chromospheric activity cycle period determination in this intermediate region.

4.4.2 Magnetic vs chromospheric cycles

Long term ZDI observations have shown that stellar magnetic fields are inherently variable (e.g. Donati et al., 2003b; Petit et al., 2009). Of particular interest are stars that show polarity reversals analogous to the ∼22 year magnetic cycle of the Sun. Morgenthaler et al. (2011) suggested that HD 78366 has a magnetic cycle of ∼3 years while several authors have studied τ Boo determining that the most probable value for its magnetic cycle period is 2 years or 8 months (Donati et al., 2008a; Fares et al., 2009, 2013). Poppenhaeger et al. (2012) were unable to find indications of this short activity cycle in X-ray observations though this may be due to the sparse sampling of their data or the fact that X-ray cycles are difficult to detect in very active stars (McIvor et al., 2006). Three dimensional magnetohydrodynamic simulations of τ Boo by Vidotto et al. (2012) also suggest that the X-ray cycle would be difficult to detect.

The short magnetic cycle of HD 78366 appears to be at odds with the much longer cycle period determined from chromospheric activity observations (Baliunas et al., 1995). However, there may be no discrepancy between the two sets of values. In the Solar case, the chromospheric cycle period is half the length of the magnetic cycle period. Assuming that this is also the case for the short magnetic cycle periods, I predict $\log \omega_{\rm cyc}/\Omega = \log P_{\rm rot}/P_{\rm cyc} = \log \frac{11.4\rm days}{1.5\rm years} = -1.68$ for HD 78366. Looking with Fig. 4.5, this value roughly coincide with the inactive branch. It seems that the magnetic cycle periods determined from ZDI for these stars may be characteristic of the inactive branch while the chromospherically determined periods are characteristic of the active branch. If this is true, then one would expect chromospheric observations with a time sampling of sufficient density to find an additional chromospheric cycle period of roughly 1.5 years for HD 78366. The data for τ Boo, which has a similar spectral type to HD 78366, would also seem to favour such an interpretation. Just like HD 78366, τ Boo also has a long chromospheric cycle (11.6 years Baliunas et al., 1995) and a short magnetic cycle (2 years or 8 months). However, in this case a shorter chromospheric cyce that is associated with the magnetic cycle has also been detected (116 day Baliunas et al., 1997; Mengel et al., 2016). If this is indeed the case, HD 78366 finds itself in a curious position of having three cycle periods (two chromospherically determined cycles (Baliunas et al., 1995) and a short magnetic cycle (Morgenthaler et al., 2011)) that cannot be explained by two dynamo modes as Böhm-Vitense (2007) suggests. It is worth noting that the shorter chromospherically determined cycle period is only assigned a false alarm probability of ‘fair’ by Baliunas et al. (1995). Additional, Baliunas et al. (1995) also assigned a false alarm probability of ‘poor’ to the 11.6 year chromospheric cycle period that they determined for τ Boo. Of course, the apparent conflict with the short magnetic cycle period would also be resolved if the longer chromospheric cycle period turned out to be unreliable.

Currently, there are very few stars on which regular polarity reversals have been observed. Looking at the stars in the sample of Saar & Brandenburg (1999), it is possible to identify the best objects to target in future ZDI observing campaigns. HD 100180 and HD 190406 both have relatively short chromospheric cycles (3.6 years and 2.6 years respectively). If the fields of these stars do undergo regular polarity reversals, their relatively short period makes them attractive targets.

4.4.3 Breaking the degeneracy in rotation period/Rossby number

The sample of stars with measured magnetic field geometries and chromospheric activity cycle periods is currently relatively small. Within this sample, all the stars on the inactive branch (marked red in Fig. 4.5) have $\mathrm{Ro} > 1$, while, with the exception of HD 78366, all those on the active branch (marked blue) have Ro < 1. As shown in Fig 4.4a, the value of Ro ~ 1 also seems to separate stars with little toroidal field (Ro $\gtrsim 1$) and those that can generate significant toroidal fields (Ro $\lesssim 1$). It is therefore tempting to associate the active branch with toroidal fields and the inactive branch with poloidal fields. This would be a very powerful result as it would allow some information about the nature of the magnetic cycle to be deduced from a measurement of the field geometry. However, caution should be exercised so as to not over interpret the data.

Currently, no active branch stars with Ro $\gtrsim 1$ have been mapped with ZDI and hence no information about their field topologies is available. If these stars are able to generate significant toroidal fields, this would be strong evidence in favour of the hypothesis presented here. However, if these stars turn out to be dominantly poloidal, the interpretation of the data would need to be reconsidered. It is therefore important to map the surface fields of active branch stars with Ro $\gtrsim 1$ using ZDI over their entire cycle. Within the sample of Saar & Brandenburg (1999), there are a number of stars with Ro $\gtrsim 1$ that lie exclusively on the active branch, e.g. HD 18256 & HD 136202, or have cycle periods on both the active and inactive branches, e.g. HD 100180, HD 165341A & HD 190406. Under the proposed interpretation, these stars would be expected to show large $f_{\rm tor}$ variations over their activity cycle despite having Ro $\gtrsim 1$. As discussed in section 4.4.2, HD 100180 and HD 190406 also have relatively short cycle periods making them even more attractive as observational targets.

Similarly, in Fig. 4.4b, for the sample of stars presented in table 4.1, the two branches are almost entirely segregated by rotation period with the transition occurring at rotation periods of roughly 15 days. Petit et al. (2008) have already shown that rotation period is an important parameter determining the toroidal energy fraction. Do stars capable of generating large $f_{\rm tor}$ values only appear on the active branch because these are the fastest rotators or is there genuinely something physically significant about the dynamos of active branch stars such that they are capable of generating large toroidal energy fractions in their surface fields? A method of breaking this degeneracy would be to map the fields of stars in the intermediate shaded regime where the branches overlap. If the hypothesis is correct, one would expect active branch stars in this region, e.g. HD 156026 ($P_{\rm cyc} = 21\ years, P_{\rm rot} = 21\ days$), to display large toroidal energy fractions while inactive branch stars with similar rotation periods would display only poloidal fields. It is clear that more ZDI maps and activity cycle period determinations, especially determinations of true magnetic cycle periods, will be needed before the hypothesis can be confirmed or rejected.

4.5 Conclusions

Progress can be made in understanding stellar activity cycles by studying them in tandem with large-scale stellar magnetic field characteristics. In this chapter, I have studied a sample of stars that have both (a) their large-scale magnetic fields reconstructed with Zeeman-Doppler imaging and (b) a chromospheric cycle period determination in the literature. I propose that active branch stars are able to maintain significant toroidal energy fractions with large epoch to epoch variations over the course of their activity cycle while stars that lie solely on the inactive branch remain dominantly poloidal. The reason for this behaviour may be due to different dynamo modes operating along the active and inactive branches as proposed by Böhm-Vitense (2007). If this is indeed the case, it could provide a way to determine which branch a cycling star lies on, and hence a method of estimating a cycle period, before a cycle period determination is made.

Despite the progress made, there are still outstanding questions. For example, why are discontinuous branches observed in the context of cycle periods but not in the activity-rotation relation? Both are manifestations of the underlying dynamo so one might naively expect them to follow similar behaviours. One possibility is that the cycle branches and the gap between them are not as distinct as currently thought (do Nascimento et al., 2015, Boro-Saikia & Jefffers et al., in prep). Related to this is the question of why magnetic energy shows a different behaviour to toroidal energy fraction. The former displays the same behaviour as the activity-rotation relation (Vidotto et al., 2014; See et al., 2015b) while the latter may be an observable manifestation of cycle branches. Any forthcoming answers will most likely be found via theoretical simulation informed by observable constraints.

4.A Data tables

In this appendix, I present data tables relevant for the work in this chapter.

Table 4.1: Parameters for the stars used in this study, ordered by Rossby number: spectral type, rotation period, convective turnover time, Rossby number, primary and secondary cycle period (if one exists), X-ray to bolometric luminosity ratio, toroidal energy fraction and the epoch of the observations from which each ZDI map was reconstructed. Each star is categorised as an active (A) or inactive (I) branch star corresponding to the blue and red points in Fig. 4.5. The paper from which cycle periods are taken are referenced with a superscript on each cycle period value. Similarly, the paper where each magnetic map was originally published is referenced with a superscript in the observation epoch column. Cycle periods listed as fair or poor under the false alarm probability scheme of Baliunas et al. (1995) are shown in brackets. For the remaining parameters, references can be found in Vidotto et al. (2014).

Star ID	Spec. type	$P_{\rm rot}$ [d]	$\tau_{\rm c}$ [d]	Ro	$P_{\rm cyc}$ [yr]	$P_{\rm cyc,2}$ [yr]	$\log R_{\rm X}$	$f_{\rm tor}$	ZDI Obs Epoch	Branch
HD 3651	K0V	43.4	20.3	2.14	13.8$^{(1)}$	-	-6.07	0.03	-$^{(2)}$	I
18 Sco	G2V	22.7	11.9	1.91	7.1$^{(3)}$	-	-6.81	0.01	2007 Aug$^{(4)}$	I
HD 10476	K1V	35.2	20	1.76	9.6$^{(1)}$	-	-6.07	0.08	-$^{(2)}$	I
61 Cyg A	K5V	34.2	25	1.37	7.2$^{(5)}$		-4.53	0.04	-$^{(2)}$	I
...	...	...	...	...	...	...	...		2007$^{(5)}$	...
...	...	...	...	...	...	...	...		2008$^{(5)}$	...
...	...	...	...	...	...	...	...		2010$^{5()}$	...
...	...	...	...	...	...	...	...		2013$^{(5)}$	...
...	...	...	...	...	...	...	...		2014$^{(5)}$	...
HD 78366	F9V	11.4	9.5	1.20	12.2$^{(1)}$	(5.9)$^{(1)}$	-4.74	0.04	-$^{(2)}$	A
HD 76151	G3V	15	13.8	1.09	(2.52)$^{(1)}$	-	-5.23	0.07	2007 Feb$^{(2)}$	I
κ Ceti	G5V	9.3	13.3	0.70	(5.6)$^{(1)}$	-	-4.71	0.62	2012 Oct$^{(6)}$	A
τ Boo	F7V	3	4.5	0.67	(11.6)$^{(1)}$	0.32$^{(7)}$	-5.12	0.63	2008 Jan$^{(8)}$	A
...	...	...	...	...	...	...	...	0.08	2008 Jun$^{(8)}$	...
...	...	...	...	...	...	...	...	0.13	2008 Jul$^{(8)}$	...
...	...	...	...	...	...	...	...	0.12	2009 May$^{(9)}$	...
...	...	...	...	...	...	...	...	0.38	2010 Jan$^{(9)}$	...
...	...	...	...	...	...	...	...	0.31	2011 Jan$^{(9)}$	...
ϵ Eri	K2V	10.3	21.3	0.48	2.95$^{(10)}$	12.7$^{(10)}$	-4.78	0.08	2007 Jan$^{(11)}$	A
...	...	...	...	...	...	...	...	0.06	2008 Jan$^{(11)}$	...
...	...	...	...	...	...	...	...	0.59	2010 Jan$^{(11)}$	...
...	...	...	...	...	...	...	...	0.26	2011 Oct$^{(11)}$	...
...	...	...	...	...	...	...	...	0.45	2012 Oct$^{(11)}$	...
...	...	...	...	...	...	...	...	0.22	2013 Sep$^{(11)}$	...
ξ Boo B	K4V	10.3	25	0.41	4.3$^{(12)}$	-	-4.6	0.32	-$^{(2)}$	A
HN Peg	G0V	4.55	13.3	0.34	5.5$^{(13)}$	-	-4.65	0.5	-$^{(2)}$	A
...	...	...	...	...	...	...	...	0.51	2008 Aug$^{(14)}$	...
...	...	...	...	...	...	...	...	0.11	2009 Jun$^{(14)}$	...
...	...	...	...	...	...	...	...	0.35	2010 Jul$^{(14)}$	...
...	...	...	...	...	...	...	...	0.39	2011 Jul$^{(14)}$	...
...	...	...	...	...	...	...	...	0.38	2013 Jul$^{(14)}$	...

Table 4.1: continued...

Star ID	Spec. type	$P_{\rm rot}$ [d]	$\tau_{\rm c}$ [d]	Ro	$P_{\rm cyc}$ [yr]	$P_{\rm cyc,2}$ [yr]	$\log R_{\rm X}$	$f_{\rm tor}$	ZDI Obs Epoch	Branch
ξ Boo A	G8V	5.56	16.9	0.33	$4.7^{(12)}$	$11^{(12)}$	-4.44	0.81	$-^{(2)}$	A
...	...	...	...	...	...	...	...	0.4	2008 Feb$^{(2)}$	...
...	...	...	...	...	...	...	...	0.61	2009 July$^{(2)}$	...
...	...	...	...	...	...	...	...	0.66	2010 Jan$^{(2)}$	...
...	...	...	...	...	...	...	...	0.33	$-^{(2)}$	...
...	...	...	...	...	...	...	...	0.81	2010 Aug$^{(2)}$	...
...	...	...	...	...	...	...	...	0.8	2011 Feb$^{(2)}$	...

1: Baliunas et al. (1995); 2: Petit et al. (in prep); 3: Hall et al. (2007); 4: Petit et al. (2008); 5: Boro Saikia et al. (submitted); 6: do Nascimento et al. (2014); 7: Baliunas et al. (1997); 8: Fares et al. (2009); 9: Fares et al. (2013); 10: Metcalfe et al. (2013); 11: Jeffers et al. (2014); 12: Oláh et al. (2009); 13: Messina & Guinan (2002); 14: Boro Saikia et al. (2015)

5

The effects of stellar winds on the magnetospheres and potential habitability of exoplanets

This chapter is based on the work presented in See et al. (2014).

5.1 Introduction

As outlined in section 1.6, the number of exoplanets discovered currently lies in the thousands. Indeed it seems that there may be almost one planet, of roughly Earth mass, per star in our galaxy (Dressing & Charbonneau, 2013). Efforts are now expanding from exoplanet detection to exoplanet characterisation. One key question researchers are attempting to answer is what ingredients are required in order for an exoplanet to be habitable and where are these planets most likely to be found (Kaltenegger & Traub, 2009; Fressin et al., 2012; Borucki et al., 2012)?

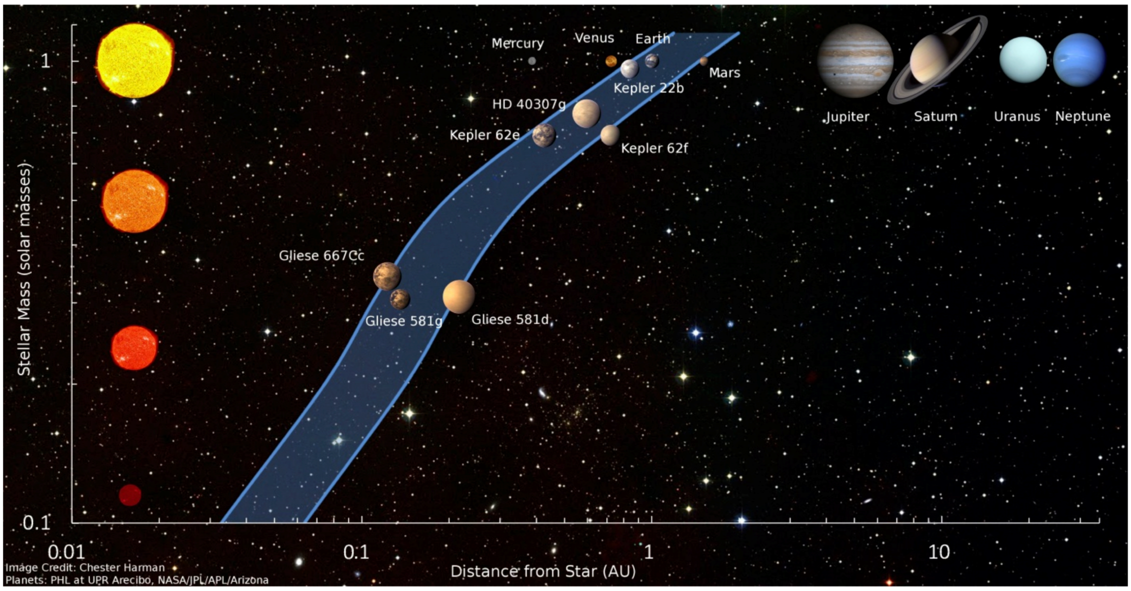

Figure 5.1: The habitable zone distances (blue shaded region) shown as a function of host star mass. Overplotted are the solar system planets as well as a number of exoplanets that have been discovered in the habitable zones of their host stars. The habitable zones of lower mass stars that are cooler lie at smaller orbital distances compared to those of higher mass stars. Used with permission from Kasting et al. (2014).

5.1.1 The habitable zone

On Earth, liquid water appears to be a basic requirement of all life. For this reason, the ability for an exoplanet to maintain liquid water on its surface is the most commonly used criterion in assessing habitability. However, determining if there is liquid water at the surface of an exoplanet is a non-trivial task. From a practical point of view, it is much simpler to determine whether a planet lies in the habitable zone (henceforth HZ) of its host star. This is the range of orbital distances where a planet is likely to have a surface temperature appropriate for liquid water (see Fig. 5.1; Huang, 1960; Hart, 1978; Kasting et al., 1993; Kopparapu et al., 2013).

In order to calculate the HZ boundaries for a planetary system, information about the central star and the planetary atmosphere is needed. The stellar luminosity, which depends on both stellar mass and age, and the orbital distance of the planet determine how much radiated energy will be incident onto the atmosphere of the planet. The thermodynamic properties of the planetary atmosphere, in conjunction with the magnitude of the incident energy, will therefore determine the temperature at the surface of the planet.

The inner edge of the habitable zone can be defined as the orbital distance at which the runaway greenhouse effect occurs. At the surface of a planet, light in the visible part of the spectrum is re-emitted by the ground in the infrared. Greenhouse gases, such as CO_2 or water vapor, present in the atmosphere absorb this radiation. Since greenhouse gases are transparent to visible light, their presence causes the atmosphere to heat up to a higher equilibrium temperature compared to an equivalent atmosphere with no greenhouse gases. A positive feedback loop can occur if the increased temperatures approach the boiling point of water. Should this happen, more water vapor is added to the atmosphere increasing the strength of the greenhouse effect. Under this scenario, the rate at which global temperatures increase begins to accelerate and a new equilibrium temperature cannot be reached. Eventually, all liquid water would evaporate into vapor - a situation not conducive to life. Indeed, the runaway greenhouse is thought to have occurred on Venus at some point in its past resulting in its current high surface temperatures (Kasting et al., 1993).

The outer edge of the habitable zone can be determined by the temperature at which CO_2 condenses out of the atmosphere. This causes the formation of CO_2 clouds. These clouds increase the albedo of the planet and decrease the amount of radiation that can penetrate into the atmosphere resulting in further atmospheric cooling (Kasting et al., 1993).

5.1.2 Other factors that affect habitability

While liquid water is undoubtedly an important factor when determining the habitability of a planet, there are other factors that must also be considered (e.g. Lammer et al., 2009; Armstrong et al., 2016). For instance, the planetary mass (Kopparapu et al., 2014), the presence of tectonic activity (Jellinek & Jackson, 2015) and the presence of a gas giant within the planetary system (Laakso et al., 2006) may all affect the development of life on any given planet. Of course, this is by no means an exhaustive list of factors affecting planetary habitability.

In the previous section, I discussed the role that the planetary atmosphere plays in regulating surface temperatures. It is clear that the ability for a planet to retain an atmosphere is key to habitability. One method by which atmospheric loss can occur is hydrodynamic escape (e.g. Murray-Clay et al., 2009). Another method is erosion of the atmosphere by sufficiently strong stellar winds, flares and coronal mass ejections (Khodachenko et al., 2007; Lammer et al., 2007; Zendejas et al., 2010; Vidotto et al., 2011; Lammer et al., 2012). If enough of the planetary atmosphere is eroded away, the planet would be rendered uninhabitable. Earth has retained its atmosphere thanks to the shielding provided by its magnetosphere. In contrast,

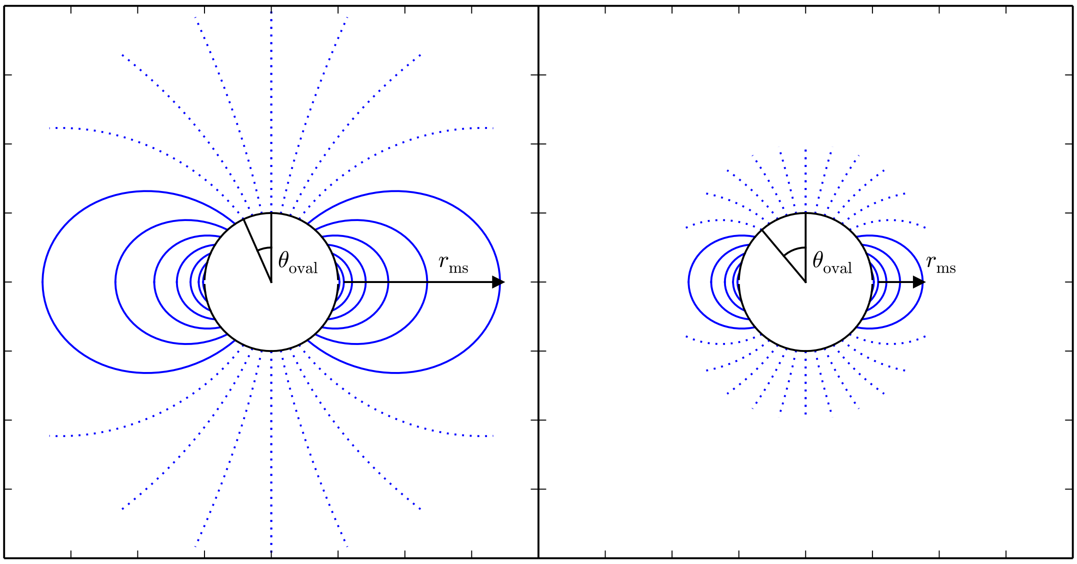

Figure 5.2: An illustration of how the auroral oval angle of a planet (the angle between the pole and the last open field line), $\theta_{\rm oval}$, is affected by magnetosphere size, $r_{\rm ms}$. As a crude first order estimate, $\theta_{\rm oval}$ can be approximated by truncating a dipole to the size of the magnetosphere. In the figure, closed field lines are shown with solid lines while open field lines are shown with dotted lines. The figure clearly shows smaller values of $\theta_{\rm oval}$ for larger magnetospheres.

Mars and Venus both currently lack a substantial intrinsic magnetic field. As a result, both suffer significant atmospheric losses with Mars having a much thinner atmosphere (Wood, 2006; Edberg et al., 2010, 2011). As a general rule, larger magnetospheres offer better atmospheric protection for two reasons. Firstly, it is more difficult for stellar winds to penetrate into the atmosphere at the substellar point, or “nose", of the magnetosphere. Secondly, the auroral oval, through which mass-loss can always occur is minimised for larger magnetosphere sizes (see Fig. 5.2).

In this chapter, I assess the ability of exoplanets, around solar-type stars, to maintain magnetospheres similar in size to both the present day and early Earth’s magnetospheres. The thermal plasma pressure, wind ram pressure, and stellar magnetic pressure all act to compress the exoplanetary magnetosphere. Vidotto et al. (2013) have studied how the stellar magnetic pressure affects hypothetical Earth analogues around M dwarfs. Compared to solar-type stars, M dwarfs have close-in HZs and can possess much stronger magnetic field strengths (Donati et al., 2008a; Morin et al., 2008b, 2010). The stellar magnetic pressure is therefore the dominant pressure term of the wind in the HZ. In contrast, the ram pressure dominates in the HZ of solar-type stars (Zarka et al., 2001; Zarka, 2007; Jardine & Collier Cameron, 2008) and so I only study the stellar wind ram pressure term in this chapter.

In order to study the interaction between stellar winds and exoplanets, I use a survey of 167 stars observed by the Bcool collaboration (Marsden et al., 2014). After excluding the subgiants and any stars that did not have all the data required for the wind models I employ, 124 solar-type stars remained, mostly with masses between $0.8M_{\odot}$ and $1.4M_{\odot}$. I refer the reader to Marsden et al. (2014) for full details of the sample. I will assume the existence of a fictitious exoplanet orbiting in the HZ of each star in this sample. Unfortunately, typical exoplanetary magnetic field strengths are not known since there have been no direct observations of exoplanetary magnetic fields to date, although Vidotto et al. (2010) and Llama et al. (2011) hint at a possible indirect detection. In light of this, I assume that the fictitious planets have the same properties as Earth, i.e. same mass, radius, and magnetic field strength. For each Earth analogue, I calculate the ram pressure exerted on it and determine if it can maintain a present day Earth-sized magnetosphere.

Lammer et al. (2007) suggest that smaller magnetospheres may still offer adequate protection and it is thought the Earth had a smaller magnetosphere in its past as a result of higher solar activity (Sterenborg et al., 2011). Tarduno et al. (2010) report that the Earth had a geodynamo around 3.4 Gyr ago, during the Paleoarchean, which generated a magnetic field that was roughly 50% weaker than the present day's. Using this field strength and the empirical wind model of Wood (2006), Tarduno et al. (2010) estimate a magnetosphere size of around 5 R_E. Since the Earth was able to retain its atmosphere, it is reasonable to assume that a Paleoarchean sized magnetosphere would sufficiently protect an Earth analogue. However, the magnetospheric size estimate of Tarduno et al. (2010) is dependent on the wind model adopted. I discuss the range of possible Paleoarchean magnetosphere sizes using different models in section 5.3.

The rest of this chapter is structured as follows. Section 5.2 covers the details of the wind models used. Section 5.3 covers the results obtained using the models outlined in the previous section and their broader implications within the context of other works. A discussion and concluding remarks follow in Sect. 5.4.

5.2 Stellar wind models

As discussed in section 1.5, theoretical modelling stellar winds is a difficult task. Within the literature, there is a wide range of approaches each with advantages and disadvantages. For this work, I employ the Parker wind model (Parker, 1958) and the Cranmer & Saar (henceforth CS) model of mass loss (Cranmer & Saar, 2011) which are both one-dimensional models. I favour these simpler models over the more sophisticated alternatives mentioned in section 1.5.3 for several reasons. Chiefly, it would take a prohibitively long time to process a sample of this size with a full MHD code. Additionally, the full set of input parameters that these models require, e.g. magnetic maps of the stellar surface, does not exist for more than a few stars in this sample. An additional benefit is the ease with which these models can be implemented. This equips the community with a tool to quickly estimate the magnetospheric size of any given exoplanet in future habitability studies.

5.2.1 Parker wind model

The Parker wind model (Parker, 1958) assumes a steady, isothermal, and spherically symmetric wind. The velocity is given by integrating the momentum equation,

$$\rho m v \frac{\partial v}{\partial r} = -\frac{\partial}{\partial r}(\rho k_{\mathrm{B}} T) - \rho m \frac{G\mathrm{M}_\star}{r^2}, \tag{5.1}$$

where ρ, v, and T are the mass density, velocity and temperature respectively, r is the radial distance from the stellar object, m is the mean particle mass, taken to be 0.6 times the proton mass, and $\mathrm{M}_\star$ is the stellar mass. I look for solutions that are subsonic at small radii and supersonic at large radii with the transition between the two regimes occurring at the sonic point, $r_s = G\mathrm{M}_\star/2c_s^2$ where c_s is the isothermal sound speed. The density profile is then obtained from mass conservation,

$$\tilde{\rho} = \frac{\rho}{\rho_0} = \frac{v_0 r_0^2}{v r^2}, \tag{5.2}$$

where $\tilde{\rho}$ is the density normalised to ρ_0, the density at an arbitrary position, r_0. The velocity has a corresponding value v_0 at r_0. I choose r_0 to be the stellar radius, i.e. $r_0 = r_\star$. The density at the stellar surface can be estimated from the chromospheric activity using a relation for the X-ray luminosity, $L_{\mathrm{X}} = \Lambda(T) EM$, where EM is the emission measure and $\Lambda(T)$ is the radiative loss function, and an empirically obtained relation between stellar chromospheric activity and

X-ray luminosity (Mamajek & Hillenbrand, 2008),

$$\log R_{\rm X} = (-4.90 \pm 0.04) + (3.46 \pm 0.18)(\log R'_{\rm HK} + 4.53). \tag{5.3}$$

Here, $R_X = L_{\rm X}/L_{\rm bol}$, is the X-ray luminosity normalised to the bolometric luminosity and $R'_{\rm HK} = L_{\rm HK}/L_{\rm bol}$ is the chromospheric activity measured in Ca II H & K lines. The emission measure is a quantity that characterises the amount of free-free emission originating from a volume of electrons and is given by

$$EM = \int n_{\rm ec}^2 dV \simeq \bar{n}_{\rm ec}^2 \cdot \frac{4}{3}\pi r_\star^3 \left(\frac{r_{\rm ss}^3}{r_\star^3} - 1\right), \tag{5.4}$$

where n_{ec} is the closed coronal electron number density and $\bar{n}_{ec}$ is the coronal electron number density averaged over the emitting region. This region is assumed to be a shell of uniform density extending from the stellar surface, $r_\star$, to an outer surface known as the source surface, r_{ss} (Altschuler & Newkirk, 1969; Jardine et al., 2002). The source surface represents the limit of confinement of the corona, beyond which the pressure of the hot coronal gas opens up the magnetic field lines. Normalised to solar values, the X-ray luminosity is therefore given by

$$\frac{L_{\rm X\star}}{L_{\rm X\odot}} = \left(\frac{\bar{n}_{\rm ec\star}}{\bar{n}_{\rm ec\odot}}\right)^2 \left(\frac{r_\star}{r_\odot}\right)^3 = \left(\frac{\rho_{\rm c\star}}{\rho_{\rm c\odot}}\right)^2 \left(\frac{r_\star}{r_\odot}\right)^3, \tag{5.5}$$

where $\rho_{\rm c\odot} = m\bar{n}_{\rm c\odot}$. I have assumed that the radiative loss function will take on similar values over the range of temperatures present in the Bcool sample of stars and that $r_{\rm ss}/r_\star$ is roughly constant. Quasi-neutrality has been assumed to obtain the final equality. The subscripts $\star$ and $\odot$ indicate stellar and solar parameters respectively and the subscript c attached to the densities in equation (5.5) indicate these are densities in the closed corona. Substituting equation (5.5) into equation (5.3) for $L_{\rm X\star}$ and re-arranging, I obtain an estimate of the closed coronal density. Omitting the errors from equation (5.3) for clarity, this is given by

$$\rho_{\rm c\star} = \rho_{\rm c\odot} \left(\frac{r_\odot^3}{r_\star^3}\frac{L_{\rm bol\star}}{L_{\rm X\odot}} 10^{-4.90+3.46(\log R'_{\rm HK}+4.53)}\right)^{\frac{1}{2}}. \tag{5.6}$$

On the Sun, the densities of coronal holes and the closed corona are known to differ. For the density at the base of the wind, I scale the coronal density calculated in equation (5.6) by a factor, f, and adopt a value of $f = 0.1$ (Guhathakurta et al., 1996). The ram pressure of the stellar wind at a given radial distance from the host star can therefore be determined by Eqs.

Table 5.1: The numerical values used in this study for the present day Earth's magnetic moment (Tarduno et al., 2010), solar coronal number density (Guhathakurta et al., 1996), luminosity (Harmanec & Prša, 2011), X-ray luminosity (Judge et al., 2003), chromospheric activity (Mamajek & Hillenbrand, 2008), and mass loss rate (Cranmer & Saar, 2011). In addition, the values for the velocity (chosen to be roughly the escape velocity), number density (Balikhin et al., 1993), and ram pressure ($P^{\rm E}_{\rm ram} = mn^{\rm E}_{\rm sw}(v^{\rm E}_{\rm sw})^2$) of the solar wind in the vicinity of the Earth are also listed.

$M_{\rm E}[{\rm Am}^2]$	$8{\times}10^{22}$
$\bar{n}_{{\rm c}\odot}[{\rm cm}^{-3}]$	10^8
$L_\odot[{\rm erg\ s}^{-1}]$	3.85×10^{33}
$L_{{\rm X}\odot}[{\rm erg\ s}^{-1}]$	2.24×10^{27}
$\log R'_{{\rm HK}\odot}[{\rm dex}]$	-4.905
$\dot{M}_\odot[{\rm M}_\odot{\rm yr}^{-1}]$	1.90×10^{-14}
$v^{\rm E}_{\rm sw}[{\rm km\ s}^{-1}]$	600
$n^{\rm E}_{\rm sw}[{\rm cm}^{-3}]$	5
$P^{\rm E}_{\rm ram}[{\rm nPa}]$	1.8

(5.1), (5.2), & (5.6) and is given by

$$P_{\rm ram}(r) = \rho(r)v^2(r) = \rho_{{\rm c}\star} f\,\tilde{\rho}(r)v^2(r). \tag{5.7}$$

The only variable in equation (5.7) that is unconstrained by the model I have presented is the wind temperature. I adopt a temperature of 2.1MK since this reproduces the solar wind parameters at Earth to a good degree within this model: $v = 1.15\ v^{\rm E}_{\rm sw}$, $n = 0.74\ n^{\rm E}_{\rm sw}$. Table 5.1 contains the numerical values for various parameters used in this study.

5.2.2 Cranmer and Saar model

Cranmer & Saar (2011) calculate mass-loss rates by considering the basal Alfvén wave energy flux emerging through the photosphere. The Alfvén waves either turbulently heat the corona sufficiently for a gas pressure wind to be driven or drive a wind directly by wave action. The total mass-loss rate is calculated with contributions from both mechanisms.

The advantage of this model is that all the parameters required (stellar mass, radius, luminosity, metallicity, and rotation period) can be observationally obtained. The first four are determined in the Bcool sample but rotation periods are unknown. In order to estimate the rotation periods, I first estimate the Rossby number, Ro, from the chromospheric activity relation of (Mamajek & Hillenbrand, 2008) which is given by

$$\begin{aligned} \mathrm{Ro} &= (0.808 \pm 0.014) - (2.966 \pm 0.098) \left(\log R'_{\mathrm{HK}} + 4.52 \right) \\ \mathrm{Ro} &= (0.233 \pm 0.015) - (0.689 \pm 0.063) \left(\log R'_{\mathrm{HK}} + 4.23 \right). \end{aligned} \tag{5.8}$$

The upper equation applies for $-5 \leq \log R'_{\mathrm{HK}} < -4.3$ and the lower equation for $\log R'_{\mathrm{HK}} \geq -4.3$. I then run the CS model (for which Rossby number is an output) for a range of rotation periods and pick the one that produces a Rossby number consistent with this estimate. As a result of the presence of low activity stars in the Bcool sample, I extend the upper relation into the $\log R'_{\mathrm{HK}} < -5$ regime. Although it may be advisable to treat the $\log R'_{\mathrm{HK}} < -5$ results with slightly more skepticism, I note that they do not differ greatly from the results obtained using the Parker model for the stellar wind. Ram pressures can then be calculated using

$$P_{\mathrm{ram}}(r) = \frac{\dot{M} v_{\mathrm{esc}}}{4\pi r^2}, \tag{5.9}$$

where $\dot{M}$ is the mass loss rate calculated using the Cranmer & Saar model and v_{esc} is the escape velocity of the star which the model uses as an estimate of the terminal wind velocity.

5.3 Results and discussion

5.3.1 Magnetospheric extent within the habitable zone

If the ram pressure acting against an Earth-like magnetosphere is known, then its size can be calculated by balancing the wind pressure with the planetary magnetospheric pressure (Grießmeier et al., 2004), i.e.

$$r_{\mathrm{ms}} = \left(\frac{\mu_0 f_0^2 M_{\mathrm{E}}^2}{8\pi^2 P_{\mathrm{ram}}} \right)^{1/6}, \tag{5.10}$$

where f_0, taken to be 1.16, is a form factor included to account for the non-spherical shape of Earth's magnetosphere, and M_E is the Earth's magnetic moment, taken to be $8 \times 10^{22}\mathrm{Am}^2$. In Fig. 5.3 I show the magnetospheric size of each planet when located at the centre of the HZ (circular points), calculated using the Parker model (left panel) and the CS model (right panel). The HZ boundaries are calculated using the formulation of Kasting et al. (1993) with the water loss and first condensation limits defining the inner and outer edges respectively. Practically, this corresponds to determining the orbital distances where $S_{\mathrm{eff}} = 1.1$ and $S_{\mathrm{eff}} = 0.53$ respectively, where S_{eff} is the flux at the planet normalised to the flux received at Earth

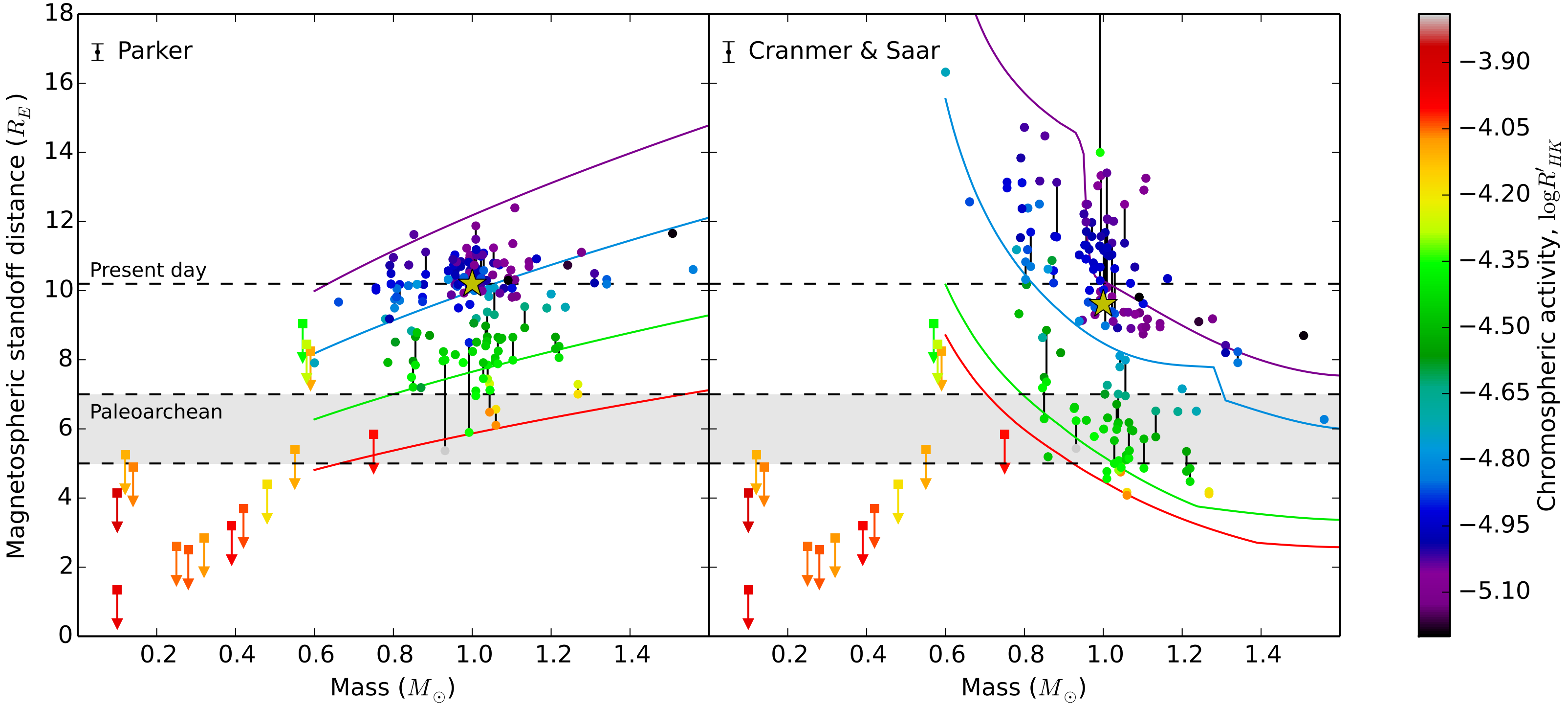

Figure 5.3: Magnetospheric size as a function of host star mass for the Parker (left) and CS (right) wind models. The Bcool sample of solar-type stars is plotted with circles and the Sun is indicated by a star symbol. Values for these standoff distances can be found in App. A. Typical errorbars for this sample are indicated in the upper left of each panel. Magnetospheric sizes computed assuming constant activity, $\log R'_{\rm HK} = -5.1, -4.8, -4.4, -4.0$, are plotted as solid lines. These correspond to chromospheric ages of 8.4, 3.2, 0.3, 0.008 Gyr respectively. It is worth noting that the Earth developed an oxygen rich atmosphere near 1.5 Gyr which corresponds to a solar chromospheric activity of $\log R'_{\rm HK} = -4.6$. The upper limit for magnetospheric sizes as calculated by Vidotto et al. (2013), for a sample of M dwarfs, are plotted with squares. All points and curves are colour coded by chromospheric activity. The upper dashed line indicates the present day magnetosphere size and the shaded area indicates a range of possible Paleoarchean magnetosphere sizes.

Table 5.2: Magnetospheric standoff distances, r_{ms} for the five fictitious planets with the largest values of r_{ms} in the Parker (top 5 results) and CS (bottom 5 results) models. Superscripts indicate the model used. Stars with large activity ranges have minimum and maximum magnetospheric sizes listed. Ram pressure and magnetospheric sizes for the entire sample are shown in appendix 5.A

Star ID	r_{ms}^{P} $[R_{\mathrm{E}}]$	r_{ms}^{CS} $[R_{\mathrm{E}}]$
HD 217107	12.39	13.25
HD 98618	11.87/11.49	10.08/13.41
HD 107213	11.65	8.7
HD 3765	11.62	14.48
HD 28005	11.36	12.91
ξ Boo B	8.50/5.90	31.76/14.00
HD 88230	7.91	16.32
HD 122064	10.96	14.72
HD 3765	11.62	14.48
HD 166620	10.73	13.84

from the Sun. Typical error bars for the magnetospheric sizes, calculated by propagating through the errors in Eqs. (5.3) and (5.8), are shown in the upper left corner. They are relatively small and I simply note that the scatter in Eqs. (5.3) and (5.8) has little impact on the conclusions. Additionally, stars with a large range of activities have upper and lower limits connected by a line. The numerical values of the five fictitious planets with the largest magnetospheric sizes, in both models, can be found in Table 5.2. Magnetosphere sizes, as well as the ram pressures at the planets, mass-loss rates and HZ locations, for the rest of the sample are available in 5.A. Also plotted are several theoretical magnetospheric standoff curves as a function of stellar mass, each at a constant chromospheric activity. These are numerically calculated using the models presented in Sect. 5.2, assuming the scaling relations $r_\star \propto \mathrm{M}_\star^{0.8}$ and $L_\star \propto \mathrm{M}_\star^{4}$. Metallicities are all set to solar levels in the CS model. I limit these curves to the stellar masses present in the Bcool sample. Both the data points and curves are colour coded by host star chromospheric activity.

In both models, the magnetospheric size increases with decreasing activity. The data points follow the curves, albeit with some scatter due to departures from the radius and luminosity scaling relations. For this modest sample of stars, a fraction of the planets can maintain present-day sized magnetospheres for both models. Many more of the planets can maintain a Paleoarchean sized magnetosphere. Using the wind model of Wood (2006) and a reduced terrestrial magnetic moment of 4.8×10^{22} Am^2, Tarduno et al. (2010) estimate the Earth's magnetosphere size to be 5 R_{E} during the Paleoarchean when the Sun was 1.2 Gyr old.

However, this magnetospheric size estimate is dependent on the wind model. At this age, the Sun would have had a chromospheric activity of -4.6 according to the activity-age relation of Mamajek & Hillenbrand (2008). Using this activity level and the reduced magnetic moment, I estimate the Paleoarchean terrestrial magnetosphere size to be 7.0 R_E and 5.3 R_E for the Parker and CS models respectively. A plausible range of values for the magnetospheric size during the Paleoarchean is therefore 5 R_E to 7 R_E. While most of the planets have magnetospheres larger than this range of Paleoarchean magnetosphere sizes in the Parker model, a significant number of them, in the CS model, fall in or below it. The level of chromospheric activity is therefore important in determining whether a magnetosphere larger than that of the young Earth can be sustained. Additionally, this highlights the impact that a different wind model can have.

Stellar activity is believed to be a function of stellar age (Skumanich, 1972; Soderblom et al., 1991; Donahue, 1998; Mamajek & Hillenbrand, 2008; Vidotto et al., 2014). As stars spin down with age, their chromospheric activity, as well as magnetic activity in general, falls, resulting in larger planetary magnetospheres. Using the chromospheric age-activity relation given by Mamajek & Hillenbrand (2008), it is possible to gain a sense of the time evolution over the Bcool sample. I note that chromospheric ages are only indicative of the true age and that stellar ages are, in general, difficult to determine. Most stars have activities between -4.4 (green curve) and -5.1 (purple curve) which correspond to ages of 0.3 Gyr and 8.4 Gyr respectively. In order to place this in context, I consider an age of 1.5 Gyr, i.e. 3 Gyr ago, close to the age at which the Earth developed an oxygen-rich atmosphere (Crowe et al., 2013). This corresponds to a chromospheric activity of -4.6 which puts it roughly midway between the blue and green curves. At this age, the CS model suggests that Earth-like planets should have a minimum magnetospheric size of 5 R_E in the mass range 0.6 $\mathrm{M}_\odot$ - 1.6 $\mathrm{M}_\odot$. Standoff distances are larger for the Parker model at this age with a minimum size of 7 R_E in the same mass range. Both models agree that stars do not have to be very old before any Earth-like planets, that they are hosting, are able to maintain, at least, a 5 R_E magnetosphere. For the CS model, this is around 1.5 Gyr and for the Parker model, it is likely to be almost immediately after the star enters the main sequence. In order for a planet orbiting in the HZ of a 1.5 Gyr old star to maintain a 7 R_E magnetosphere under the CS model, the host star needs to be less than 1.0 $\mathrm{M}_\odot$.

The main difference between the two models presented in this paper is the mass dependent behaviour. The CS model shows decreasing standoff distances with mass which is the opposite behaviour in the Parker model. It is always possible to reconcile the two models by adjusting the wind temperature adopted in the Parker model. More massive, and hence hotter, stars have higher convective velocities resulting in a higher wave energy flux emerging through the photosphere (Musielak & Ulmschneider, 2002). More energy is therefore available to drive the wind within the CS model. This increased wave energy flux would lead to higher coronal temperatures and could be mimicked in a Parker-type model by assuming a mass-dependent coronal temperature. However, most of the stars in the sample do not have observational constraints of their wind properties (e.g. using the technique of Wood (2006)). As a result, it is difficult to determine whether the Parker or CS model is the more appropriate one.

5.3.2 Comparison with other work

In this section, I compare the mass-loss rates that result from the Parker and CS models with ones obtained indirectly from observations of astrospheric Lyα absorption (see Wood et al. (2014) and the discussion in section 1.5.2). Of their stars, three are also present in the Bcool sample: ϵ Eri with a mass-loss rate of $30\dot{M}_\odot$ (Wood et al., 2002) and the ξ Boo binary system with a combined mass-loss rate of $5\dot{M}_\odot$ (Wood et al., 2005). For ϵ Eri, I obtain mass-loss rates of $0.70\dot{M}_\odot$ - $1.27\dot{M}_\odot$ (Parker) and $0.63\dot{M}_\odot$ - $1.91\dot{M}_\odot$ (CS). For ξ Boo A, I obtain mass-loss rates of $1.76\dot{M}_\odot$ - $19.3\dot{M}_\odot$ (Parker) and $8.25\dot{M}_\odot$ - $18.8\dot{M}_\odot$ (CS) while for ξ Boo B I obtain $0.26\dot{M}_\odot$ - $2.35\dot{M}_\odot$ (Parker) and $9.7\times10^{-5}\dot{M}_\odot$-$0.013\dot{M}_\odot$ (CS). The ξ Boo estimates are particularly interesting. I predict a higher mass-loss rate for ξ Boo A whereas Wood & Linsky (2010) suggest that it is ξ Boo B that contributes most of the mass-loss in this system despite ξ Boo A being extremely coronally active. The authors suggest that, above some activity level, mass-loss is inhibited by some mechanism.

In addition to comparing the mass-loss rates of individual stars, I also compare the overall samples. Figure 5.4 shows the mass-loss rates per unit surface area plotted in blue against X-ray flux for the Parker and CS models. Mass-loss rates are given by $\dot{M} = 4\pi\rho(r_\star)v(r_\star)r_\star^2$ for the Parker model and taken directly from the CS model. X-ray fluxes are calculated by dividing the X-ray luminosities, from equation (5.5), by the stellar surface areas. Numerical values for the mass-loss rates can be found in appendix 5.A. Additionally, I have overplotted the data presented by Wood et al. (2014) in red (see their Fig. 4 or Fig. 1.9). From their

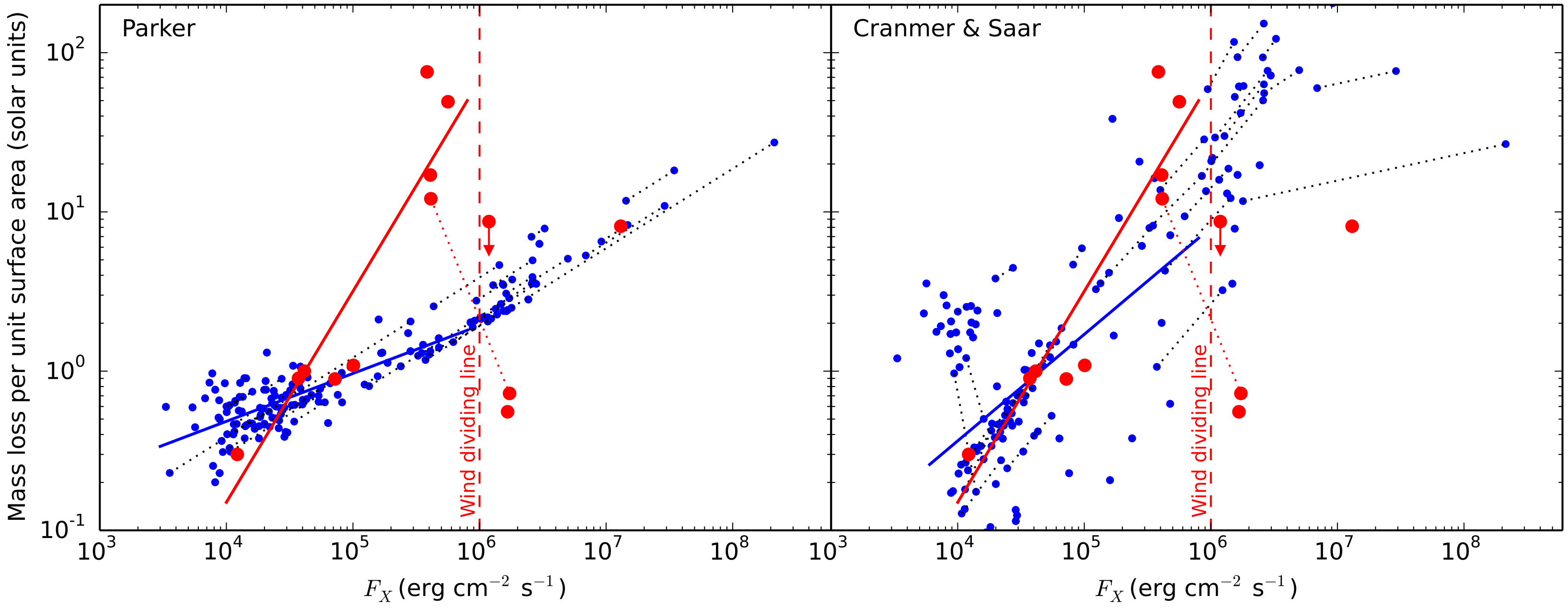

Figure 5.4: Mass-loss rates per unit surface area as a function of X-ray flux for the Parker (left) and CS (right) models are plotted in blue. Values for these mass-loss rates can be found in App. A. The mass-loss rates and the wind dividing line of Wood et al. (2014) are overplotted in red (see their Fig. 4). These authors fit a power law (red solid line), $\dot{M} \propto F_X^{1.34\pm0.18}$, to their data points below the wind dividing line. For the Bcool data, I find power laws of $\dot{M} \propto F_X^{0.30\pm0.02}$ and $\dot{M} \propto F_X^{0.67\pm0.10}$ for the Parker and CS models respectively (solid blue lines). If I use the entire sample, I find $\dot{M} \propto F_X^{0.38\pm0.01}$ and $\dot{M} \propto F_X^{0.72\pm0.07}$ respectively. I note that the quoted errors are in the fit only.

data, the authors suggest that winds from solar-type stars fall into two regimes separated by a so-called wind dividing line (dashed red line). For the stars below this line, they find a power law of $\dot{M} \propto F_{\mathrm{X}}^{1.34\pm0.18}$ (solid red line). I find power laws of $\dot{M} \propto F_{\mathrm{X}}^{0.30\pm0.02}$ and $\dot{M} \propto F_{\mathrm{X}}^{0.67\pm0.10}$ for the Parker and CS models respectively when accounting for the low activity stars only (solid blue lines). If I include the whole sample in the fits, I obtain $\dot{M} \propto F_{\mathrm{X}}^{0.38\pm0.01}$ and $\dot{M} \propto F_{\mathrm{X}}^{0.79\pm0.05}$ respectively. I note that the quoted errors are in the fits only. Both the Parker and CS models predict increasing mass-loss rates with increasing X-ray activity. This general trend is in agreement with that of Wood et al. (2014) below their wind dividing line although the power law value they find is higher. The main difference between the Parker & CS models and the results of Wood et al. (2014) is the behaviour at high X-ray flux. These authors suggest that solar-type stars can be divided into two wind regimes where the most active stars have lower mass-loss rates than some less active stars. They hypothesise that a change in magnetic field topology can explain the reduced mass-loss rates of the more active stars though Vidotto et al. (2016) find no such break in the large-scale topologies of fields on either side of the wind dividing line. The Parker model is unable to reproduce the reduced mass-loss rates above the wind dividing line unless the wind temperature is varied from star to star while the CS model does show some hints of this behaviour. It is clear that further astrospheric Lyα absorption observations of high activity stars are required to allow a more in depth study of winds from these stars.

It is also interesting to compare the results presented in this chapter to those of Vidotto et al. (2013), whose results are plotted in Fig. 5.3 with square symbols. These magnetospheric sizes, for fictitious Earth-analogues in the HZs of M dwarfs, are calculated considering only the pressure contribution of the stellar magnetic field and neglect the wind ram pressure. These points are shown as upper limits since including the wind ram pressure would only decrease the size of the planetary magnetosphere. None of their planets are able to maintain an Earth-sized magnetosphere although several, at the higher host star mass end of their sample, are able to maintain a Paleoarchean-sized one. To make a comparison with the M dwarfs, I use the red curve, rather than the entire sample of solar-type stars. This is a fairer comparison since the solar-type stars span a large range of ages. When using the Parker model there may be a smooth transition between the solar and M dwarf samples. The situation is not as clear for the CS model. There appears to be a mass range, at around 0.6 $M_\odot$ - 0.8 $M_\odot$, where magnetospheric sizes peak. At lower masses, the HZ is too close to the star where the magnetic pressure can be high, especially at younger ages. At higher masses, the higher basal Alfvén wave flux is able to drive much stronger winds, as previously discussed. 0.6 $M_\odot$ - 0.8 $M_\odot$ therefore represents a stellar mass regime where neither the magnetic or ram pressures are too high.

5.3.3 Evolution of planetary systems

The analysis presented so far considers each system at a particular snapshot in time. However, the present conditions of a given system are determined by its history and will, in turn, determine the future evolution of the system. The theoretical standoff curves plotted in Fig. 5.3 already give a sense of how planetary magnetospheres around solar-type stars would evolve. In particular, the red, 8 Myr, curve is an indication of the level of magnetospheric protection available to young Earth-analogues. For the Parker model, magnetospheric sizes greater than $5R_\mathrm{E}$ are possible for all stellar masses above 0.6 $M_\odot$. However, the CS model predicts much reduced magnetosphere sizes for Earth-analogues around higher mass stars. Consequently, these planets may have a more difficult time retaining their atmospheres in the face of the harsher winds expected during the early, more active period of a star's life. However, the Parker and CS models predict that stars with a higher coronal activity present stronger winds. Wood et al. (2014) present evidence that young solar-type stars may have much weaker winds than expected. If this is indeed the case, young Earth-analogues may be more able to protect their atmospheres than initially thought.

It is also pertinent to consider the time evolution of the M dwarfs. If given enough time, could their magnetic activity decline to the point where the magnetic pressure is no longer the dominant pressure in the HZ? Additionally, could it decline to the point where an Earth-analogue in orbit could maintain a large magnetosphere? The former question is not easily answered. Stellar magnetic fields and winds are both linked to the stellar dynamo (Schwadron & McComas, 2008) and both decline as a star ages along the main sequence (Wood et al., 2005; Vidotto et al., 2014). It is not clear when, or indeed if, the dominant pressure term might switch for a given spectral type. The latter question is easier to assess, at least in terms of magnetic pressure. West et al. (2008) studied how M dwarf activity lifetimes varied with spectral type. The authors find increasing activity lifetimes for later-type dwarfs; 8 Gyr for M7 dwarfs compared to 0.8 Gyr for M0. Vidotto et al. (2013) also studied the evolution of M dwarf magnetism using stellar rotation as a proxy for activity. The authors found that early- to mid-type M dwarfs require rotation periods of $\gtrsim$37-202 days in order for any Earth-analogues they host to maintain an Earth-sized magnetosphere. The required rotation period increases to $\gtrsim$63-263 days for late-type M dwarfs. Both results imply that only very old Earth-analogues around late type M dwarfs are able to maintain large magnetospheres.

Given the long timescales over which low mass stars remain magnetically active, it seems unlikely that an orbiting Earth-analogue could hold onto its atmosphere. Replenishment, via planetary volcanism, could be a solution to this problem (Papuc & Davies, 2008; Jackson et al., 2008; Padhi et al., 2012). However, this will only be effective if it is still occurring after stellar activity has declined sufficiently for the planet to maintain a large magnetosphere. This may be problematic given that volcanic activity has died down over geological timescales on Earth and Mars (Werner, 2009). Additionally, it is thought that water might be a necessary ingredient for plate tectonics (Regenauer-Lieb et al., 2001). If the atmosphere, and hence surface water, has already been lost, replenishment of the atmosphere by volcanism may be difficult. It is clear that planets in the HZs of M dwarfs would have greater difficulty maintaining their atmospheres. As such, planets around solar-type stars seem to be much more attractive targets for habitability in this regard.

5.3.4 Observing Earth-analogues

Section 5.3.1 demonstrates that, in general, exoplanets around solar-like stars do not simultaneously have both an Earth-like surface temperature and an Earth-sized magnetosphere. While most of the planets can maintain a Paleoarchean magnetosphere, it is still beneficial for them to have larger magnetospheres since the auroral opening, through which atmospheric leakage occurs, shrinks for larger magnetospheres (Tarduno et al., 2010; Vidotto et al., 2013). It would therefore be useful to identify the observational signatures of stars with weaker winds.

Fig. 5.5 shows the parameter space that the Bcool sample occupies in terms of Ca II H & K luminosity, L_{HK}, and bolometric luminosity with the points colour coded by magnetospheric size under the Parker model. The most striking feature is the presence of two distinct branches separated by the, so called, Vaughan-Preston gap (Vaughan & Preston, 1980). Many explanations have been proposed to explain the gap including different dynamos operating along each branch (Böhm-Vitense, 2007), an abrupt change in chromospheric activity with stellar age (Pace et al., 2009), or multiple waves of star formation (McQuillan et al., 2013).

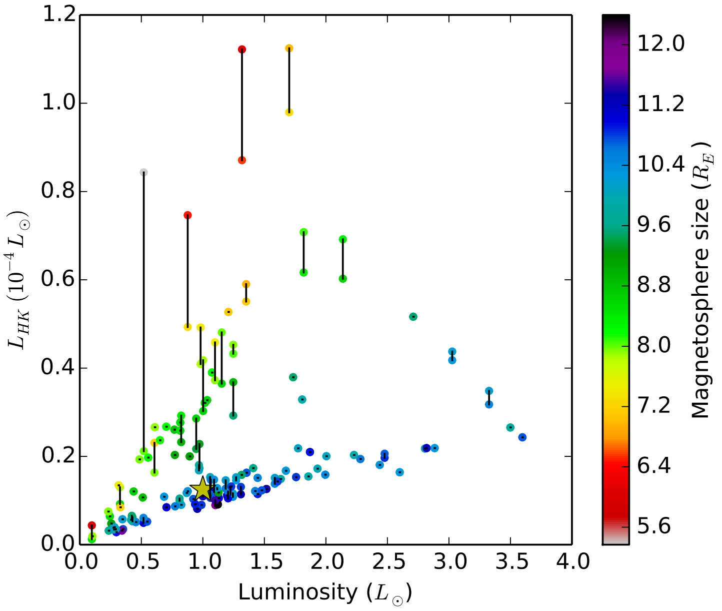

Figure 5.5: Each star is plotted in Ca II H & K luminosity-bolometric luminosity space and colour coded according to the magnetospheric size of its planet according to the Parker wind model. HD 107213 and HD 18256 have not been plotted because of their large luminosities. Low-luminosity and low-activity stars, i.e. the stars below the Vaughan-Preston gap, represent optimum observing targets.

In general, planets that orbit low chromospheric activity stars, at a given luminosity, have greater magnetospheric protection which is evident from Fig. 5.5. Planets orbiting stars on the lower, inactive, branch generally have larger magnetospheres. Whatever the cause for the Vaughan-Preston gap, it is clear that stars on the low activity branch are the optimum hosts of potentially habitable planets. The same trend can be seen when using the CS model although the data points have not been plotted.

5.4 Conclusion

In this chapter, I have presented a study on the effect of stellar winds on exoplanet magnetosphere sizes. This will better inform the search for extra-solar Earth analogues which may potentially be habitable. In particular, I have considered whether it is feasible for an exoplanet to simultaneously have an Earth-like surface temperature and Earth-sized magnetosphere. These constraints increase the chance of liquid water existing and help retain the planetary atmosphere respectively. Both are thought to be important to habitability. Since the exact size of magnetosphere required to protect a planetary atmosphere is not known, I consider two reasonable values of magnetospheric size. These are the present day magnetosphere size, 10.2 R_E, and its size 3.4 Gyr ago, estimated to be between 5 R_E and 7 R_E.

Using the wind models of Parker (1958) and Cranmer & Saar (2011), I estimated the magnetospheric extent of a hypothetical Earth orbiting each star in a sample of 124 solar-type stars. Within this modest sample, only a fraction of the planets were able to maintain a 10.2 R_E magnetosphere. Most of them are able to maintain one of at least 7 R_E within the Parker model although, within the CS model, a non-negligible number fall into, or below, the range of Paleoarchean magnetosphere sizes considered here. As stars age, the magnetospheric protection provided by an exoplanetary magnetic field of fixed strength will only increase thanks to the declining magnetic activity of the star. The results suggest that a level of protection comparable to the early Earth's should be possible for planets orbiting stars of age greater than roughly 1.5 Gyr under the Cranmer & Saar model and almost immediately after a star enters the main sequence according to the Parker model.

The result is striking when compared to that of Vidotto et al. (2013). Most terrestrial planet searches focus on M dwarfs because their low luminosities and masses are ideal for the transit and radial velocity techniques. However, from the point of view of atmospheric protection, young active M dwarfs can be less than ideal. Their habitable zones lie much closer in allowing the stellar magnetic pressure to compress planetary magnetospheres by a significant amount. Interestingly, when searching for well shielded planets in the habitable zone of stars, there are hints at the possibility of an optimum host star mass. For the Cranmer & Saar model, planets orbiting 0.6 $\mathrm{M}_\odot$ - 0.8 $\mathrm{M}_\odot$ stars seem to have the largest magnetospheric sizes. Around this range of masses, the star is dim enough that the habitable zone lies far out, and hence stellar magnetic pressure is low, whilst having a low enough mass that convective jostling of flux tubes only drives a relatively weak wind. For the Parker model, magnetospheric sizes increase with increasing host star masses. Both models agree that, in general, solar analogues are more likely than M dwarfs to host planets with large magnetospheres and surface temperatures appropriate for liquid water.

When considering atmospheric protection, it is important to remember that other factors, such as the size of the auroral oval or whether the atmosphere is being replenished, will also determine if a stable atmosphere is present. Additionally, the chosen values of 5 R_E to 7 R_E and 10.2 R_E should only be thought of as reasonable magnetospheric sizes on a sliding scale where larger sizes are clearly better. They should not be considered as strict criteria by which to judge magnetospheric protection. The results indicate that planets around 0.6 $M_{\odot}$ - 0.8 $M_{\odot}$ stars on the low activity side of the Vaughan-Preston gap are the optimum observing targets for habitable Earth analogues. This, as well as the contrast between solar-type stars and M dwarfs, highlights how important it is to characterise the host star when considering habitability.

5.A Data tables

In this appendix, I present data tables relevant for the work in this chapter.

Table 5.3: Ram pressure, $P_{\rm ram}$, exerted on a hypothetical Earth analogue located in the centre of the habitable zone, $r_{\rm HZ}$, the corresponding magnetospheric size, $r_{\rm ms}$, and the mass-loss rates, $\dot{M}$, for the Bcool sample of stars. Superscripts indicate the wind model used.

Star ID	$P_{\rm ram}^{\rm P}$ [$P_{\rm ram}^{\rm E}$]	$P_{\rm ram}^{\rm CS}$ [$P_{\rm ram}^{\rm E}$]	$r_{\rm ms}^{\rm P}$ [$R_{\rm E}$]	$r_{\rm ms}^{\rm CS}$ [$R_{\rm E}$]	$\dot{M}^{\rm P}$ [$\dot{M}_\odot$]	$\dot{M}^{\rm CS}$ [$\dot{M}_\odot$]	$r_{\rm HZ}$ [AU]
16 Cyg A	0.84/0.99	1.23/0.51	10.47/10.20	9.82/11.38	1.06/1.24	2.02/0.84	1.47
16 Cyg B	0.88/1.00	0.29/0.37	10.38/10.18	12.50/11.99	0.88/0.99	0.37/0.48	1.3
18 Sco	0.61/1.11	0.44/2.11	11.05/10.00	11.68/8.98	0.53/0.96	0.44/2.12	1.2
5 Pegase	0.55/0.70	0.29/0.51	11.24/10.80	12.50/11.37	0.58/0.74	0.37/0.65	1.34
EK Dra	7.28/14.91	75.36/96.42	7.31/6.48	4.95/4.75	5.28/10.81	59.38/75.98	1.09
ϵ Eri	2.61/4.75	2.30/6.97	8.67/7.85	8.85/7.36	0.73/1.33	0.66/2.01	0.67
HD 100180	0.72	0.98	10.74	10.21	0.79	1.25	1.36
HD 10086	1.84	7.54	9.19	7.26	1.35	6.19	1.1
HD 101501	4.35/7.91	6.27/17.88	7.96/7.21	7.49/6.29	2.18/3.96	3.65/10.41	0.91
HD 103095	1.36	0.28	9.67	12.57	0.27	0.06	0.57
HD 10476	1.00/1.32	0.43/0.74	10.18/9.72	11.69/10.70	0.36/0.47	0.17/0.30	0.76
HD 10697	1.22	1.85	9.84	9.18	2.67	6.04	1.95
HD 107213	0.44	2.56	11.65	8.7	1.87	14.97	2.73
HD 107705	0.65	0.9	10.92	10.35	0.98	1.62	1.6
HD 10780	2.33	2.66	8.83	8.64	0.99	1.27	0.83
HD 111395	2	9.38	9.06	7	1.28	6.5	1.03
HD 115404a	2.41	56.47	8.78	5.19	1.51	38.31	1.02
HD 117936	2.91	1	8.51	10.17	0.62	0.22	0.58
HD 120476a	8	0.67	7.19	10.87	2.27	0.22	0.67
HD 122064	0.64	0.11	10.96	14.72	0.16	0.03	0.64
HD 128165	1.85	0.57	9.18	11.18	0.41	0.13	0.59
HD 12846	1	0.46	10.18	11.57	0.67	0.37	1.06
HD 13043	1.07	0.75	10.06	10.68	1.69	1.56	1.65
HD 131511	4.33	13.54	7.97	6.59	1.77	5.83	0.81
HD 135101	0.66	1.31	10.9	9.73	0.76	1.93	1.4
HD 13825	0.62	0.36	11.03	12.06	0.56	0.39	1.24
HD 138573	0.79/0.85	0.43/0.53	10.58/10.44	11.71/11.31	0.68/0.73	0.45/0.55	1.2
HD 145825	1.09/1.23	3.89/4.94	10.03/9.83	8.11/7.79	0.87/0.98	3.44/4.37	1.15
HD 1461	0.61	0.37	11.03	12.01	0.59	0.43	1.28
HD 149661	2.55	3.64	8.7	8.2	0.94	1.42	0.77
HD 152391	3.56	13.1	8.23	6.63	1.66	6.5	0.87
HD 15335	1.24	2.48	9.81	8.75	3.34	10.36	2.18
HD 159909	1.41	1.35	9.6	9.68	1.59	1.94	1.39
HD 160346	0.99	0.77	10.18	10.62	0.29	0.24	0.69
HD 16141	0.85	1.63	10.45	9.38	1.33	3.48	1.65
HD 16160	1.07	0.31	10.05	12.39	0.25	0.08	0.61
HD 164595	0.68/0.74	0.38/0.46	10.84/10.70	11.97/11.57	0.59/0.63	0.39/0.47	1.2
HD 166435	4.74/6.51	64.34/89.75	7.85/7.44	5.08/4.81	3.81/5.25	57.47/80.17	1.16
HD 166620	0.73	0.16	10.73	13.84	0.22	0.05	0.69
HD 166	4.5	29.73	7.92	5.78	2.3	16.03	0.91
HD 171488	13.81/21.40	211.14/240.41	6.57/6.11	4.17/4.08	14.70/22.79	263.09/299.56	1.34
HD 175726	4.07/4.40	53.66/62.81	8.05/7.95	5.24/5.10	4.11/4.45	62.45/73.10	1.3
HD 179958	0.62/0.79	0.20/0.46	11.02/10.59	13.33/11.57	0.60/0.76	0.23/0.55	1.28
HD 18256	0.78	18.18	10.61	6.27	3.95	116.89	3
HD 1832	1.51	1.1	9.5	10.01	1.59	1.49	1.34
HD 183658	0.60/0.76	0.36/0.61	11.08/10.65	12.08/11.05	0.59/0.75	0.42/0.72	1.29
HD 185144	1.29/1.51	0.69/0.92	9.75/9.50	10.83/10.32	0.46/0.54	0.27/0.36	0.76
HD 18803	1.03	1.36	10.13	9.67	0.73	1.12	1.09
HD 190771	2.64/4.62	19.83/59.24	8.65/7.88	6.18/5.15	2.18/3.80	18.04/53.90	1.17
HD 194012	1.18	8.24	9.9	7.16	1.71	13.88	1.57
HD 196850	1	0.56	10.18	11.2	0.98	0.69	1.29
HD 206860	2.64/4.26	32.00/83.96	8.65/7.99	5.71/4.86	2.49/4.02	33.41/87.66	1.25
HD 208776	0.9	1.65	10.36	9.36	1.71	4.47	1.82

Table 5.3: continued...

Star ID	$P_{\rm ram}^{\rm P}$ [$P_{\rm ram}^{\rm E}$]	$P_{\rm ram}^{\rm CS}$ [$P_{\rm ram}^{\rm E}$]	$r_{\rm ms}^{\rm P}$ [$R_{\rm E}$]	$r_{\rm ms}^{\rm CS}$ [$R_{\rm E}$]	$\dot{M}^{\rm P}$ [$\dot{M}_\odot$]	$\dot{M}^{\rm CS}$ [$\dot{M}_\odot$]	$r_{\rm HZ}$ [AU]
HD 210277	0.55	0.23	11.23	13.03	0.43	0.21	1.14
HD 213575	1.16	1.71	9.93	9.31	1.68	3.51	1.59
HD 217107	0.31	0.2	12.39	13.25	0.28	0.21	1.24
HD 217813	3.51	46.1	8.25	5.37	3.09	44.92	1.21
HD 217877	0.93	2.2	10.3	8.92	1.24	3.75	1.51
HD 218687	8.66/9.76	94.20/123.31	7.10/6.96	4.77/4.56	9.39/10.58	125.64/164.47	1.36
HD 218868	0.79	0.61	10.57	11.03	0.5	0.45	1.03
HD 219134	0.99	0.22	10.19	13.12	0.24	0.06	0.62
HD 221146	0.78	2.18	10.6	8.93	1.4	5.22	1.76
HD 221354	0.72	0.21	10.74	13.17	0.33	0.11	0.86
HD 221356	0.85	0.62	10.46	11	0.98	0.9	1.4
HD 221830	1.19	1.9	9.88	9.14	1.53	3.34	1.49
HD 222143	2.69	25.07	8.63	5.95	2.29	23.45	1.19
HD 225261	0.83	0.31	10.5	12.37	0.31	0.13	0.79
HD 22879	1.85	0.47	9.18	11.53	1.64	0.58	1.24
HD 24213	0.68/0.74	2.01/2.16	10.84/10.70	9.05/8.95	1.33/1.44	5.23/5.61	1.84
HD 24496	0.61	0.66	11.03	10.91	0.36	0.42	0.98
HD 25680	2.77	24.33	8.59	5.98	2.31	22.39	1.18
HD 26965	1.24	0.57	9.82	11.19	0.43	0.22	0.75
HD 28005	0.52	0.24	11.36	12.91	0.63	0.36	1.44
HD 30562	0.59	1.85	11.11	9.18	1.31	5.4	1.96
HD 30652	1.49	14.54	9.52	6.51	3.18	37.97	1.92
HD 32147	1.02	0.29	10.14	12.5	0.25	0.07	0.62
HD 34411	0.7	1.69	10.8	9.32	0.97	3.02	1.55
HD 35296	3.18/4.03	84.50/137.43	8.39/8.06	4.86/4.48	4.66/5.92	142.14/231.19	1.57
HD 3651	0.59/0.84	0.22/0.47	11.12/10.47	13.13/11.55	0.25/0.36	0.10/0.22	0.84
HD 3765	0.45	0.12	11.62	14.48	0.13	0.04	0.68
HD 377	8.5	81.52	7.12	4.89	8.33	95.02	1.28
HD 3821	2.92	17.4	8.51	6.32	1.97	12.84	1.05
HD 39587	4.50/6.45	33.61/70.96	7.92/7.46	5.66/5.00	4.03/5.76	34.80/73.46	1.22
HD 45289	0.83	1.13	10.5	9.97	0.94	1.66	1.39
HD 4614	0.69	0.53	10.82	11.29	0.68	0.63	1.29
HD 4628	1.06/1.10	0.22/0.23	10.08/10.01	13.14/12.97	0.26/0.27	0.06/0.06	0.63
HD 4915	0.91	1.93	10.33	9.11	0.52	1.2	0.97
HD 5065	0.92	2.16	10.31	8.95	2.06	6.97	1.98
HD 50692	0.95/1.02	0.75/0.93	10.27/10.13	10.68/10.29	0.97/1.05	0.93/1.16	1.32
HD 56124	0.60/0.79	0.77/1.68	11.09/10.58	10.64/9.33	0.52/0.68	0.75/1.65	1.2
HD 59747	6.24	8.04	7.5	7.19	1.69	2.27	0.66
HD 71148	0.80/1.02	0.57/1.09	10.56/10.15	11.16/10.02	0.77/0.97	0.66/1.26	1.27
HD 73344	1.51	14.66	9.5	6.5	2.11	23.5	1.54
HD 73350	1.62/2.62	9.36/19.88	9.38/8.66	7.01/6.18	1.26/2.04	8.02/17.03	1.13
HD 75332	2.63/3.34	47.38/93.79	8.66/8.32	5.35/4.77	4.49/5.70	95.54/189.14	1.71
HD 76151	1.06/1.71	4.25/9.79	10.07/9.30	7.99/6.96	0.85/1.37	3.75/8.63	1.15
HD 7727	1.06	1.39	10.07	9.62	1.5	2.46	1.55
HD 78366	1.47/2.19	14.46/30.04	9.54/8.93	6.52/5.77	1.50/2.23	16.26/33.79	1.3
HD 82106	4.48	1.68	7.92	9.33	0.9	0.35	0.56
HD 8262	0.72	0.53	10.74	11.32	0.54	0.46	1.12
HD 86728	0.69	0.29	10.83	12.49	0.55	0.28	1.16
HD 88072	0.91/0.95	0.70/0.78	10.33/10.26	10.80/10.61	0.82/0.86	0.76/0.85	1.23
HD 88230	4.52	0.06	7.91	16.32	0.41	0.01	0.37
HD 88986	1.16	2.22	9.93	8.91	2.02	5.39	1.74
HD 89269	1.24/1.35	0.79/0.97	9.81/9.68	10.58/10.22	0.82/0.89	0.63/0.77	1.05
HD 9407	0.66	0.33	10.9	12.22	0.5	0.3	1.13
HD 9562	0.72	1.95	10.74	9.1	2.02	7.86	2.21
HD 98618	0.40/0.48	1.06/0.19	11.87/11.49	10.08/13.41	0.35/0.43	1.10/0.20	1.22
HD 9986	0.63/0.90	0.61/1.61	10.99/10.35	11.04/9.39	0.56/0.80	0.63/1.65	1.22
HIP 100970	1.11	1.94	9.99	9.11	1.69	4.05	1.62
HIP 10339	3.78	18.59	8.15	6.25	2.05	10.89	0.94
HIP 38228	3.54	23.85	8.24	6	2.08	14.9	0.98
HIP 41844	0.72	1.4	10.74	9.62	0.85	2.12	1.42
HIP 49350	0.88	1.49	10.38	9.52	0.64	1.21	1.09
HIP 53721	0.7	1.63	10.79	9.38	0.9	2.64	1.48

Table 5.3: continued...

Star ID	$P_{\mathrm{ram}}^{\mathrm{P}}$ $[P_{\mathrm{ram}}^{\mathrm{E}}]$	$P_{\mathrm{ram}}^{\mathrm{CS}}$ $[P_{\mathrm{ram}}^{\mathrm{E}}]$	$r_{\mathrm{ms}}^{\mathrm{P}}$ $[R_{\mathrm{E}}]$	$r_{\mathrm{ms}}^{\mathrm{CS}}$ $[R_{\mathrm{E}}]$	$\dot{M}^{\mathrm{P}}$ $[\dot{M}_{\odot}]$	$\dot{M}^{\mathrm{CS}}$ $[\dot{M}_{\odot}]$	r_{HZ} [AU]
HIP 7244	2.88	20.76	8.53	6.14	1.95	15.12	1.05
HIP 86974	0.93	1.24	10.3	9.81	1.88	3.79	1.88
HR 1817	7.38/9.38	206.09/227.42	7.29/7.01	4.19/4.12	10.22/12.97	320.74/353.94	1.52
κ Cet	2.12/3.15	12.11/24.13	8.98/8.40	6.71/5.98	1.45/2.15	8.92/17.77	1.06
τ Boo	0.92/0.99	3.56/4.51	10.32/10.19	8.23/7.92	2.19/2.37	10.48/13.26	2.03
υ And	0.83/0.97	3.12/3.64	10.50/10.22	8.42/8.20	2.16/2.54	10.81/12.62	2.13
ξ Boo A	4.24/46.31	18.87/43.06	7.99/5.37	6.23/5.43	1.86/20.28	8.69/19.82	0.84
ξ Boo B	2.94/26.33	0.001/0.15	8.50/5.90	31.76/14.00	0.28/2.47	0.0001/0.01	0.36

6

Time-scales of close-in exoplanet radio emission variability

This chapter is based on the work presented in See et al. (2015a).

6.1 Introduction

In chapter 5, I discussed the idea of exoplanetary habitability. The presence of a magnetosphere was identified as a key property required to prevent atmospheric mass-loss due to stellar wind erosion. Currently, there are no techniques to directly detect exoplanetary magnetic fields and so, by necessity, I assumed that the fictitious exoplanets had the same magnetic field strength as the present day Earth. However, there are a number of techniques that might be used to indirectly infer the magnetic field strength of an exoplanet. For example, observations of the hot Jupiter WASP-12b show that it has an asymmetrical transit in the ultraviolet (Fossati et al., 2010). Assuming that the asymmetry is due to the presence of a magnetospheric bow shock, Vidotto et al. (2010) determine that this planet should have a magnetic field strength of < 24G.

Another method by which the magnetic field strengths of exoplanets might be determined is via the detection of radio emissions. Within the solar system, all the magnetised planets are known to emit in the radio part of the electromagnetic spectrum (Zarka, 1998). Energetic particles from the solar wind are channeled into the planetary poles where their excess energy is emitted in various wavelength, including radio wavelengths (see Fig. 6.1). The angular frequency of these radio emissions appear to be dependent on the local magnetic field strength,

$$\omega_{\mathrm{c}} = \frac{eB}{m_{\mathrm{e}}}. \tag{6.1}$$

Here, ω_{c} is known as the electron cyclotron frequency, B is the local magnetic field strength and e and m_{e} are the electron charge and mass respectively. Such a dependence on the local magnetic field strength suggests that the electron-cyclotron maser instability is responsible for generating the radio signals (Treumann, 2006). This property is useful because it would allow us to infer the magnetic field strength of exoplanets from which radio emissions are detected.

The main energy source of the planetary radio emissions is the solar wind. Interestingly, the conversion efficiency between the incident and emitted energy is roughly constant for all the planets in the solar system. This correlation is known as the radiometric Bode's law (Desch & Kaiser, 1984; Farrell et al., 1999; Zarka et al., 2001; Zarka, 2007) and can be seen in Fig. 6.2.

In analogy with the solar system, it is thought that magnetised exoplanets may also emit in the radio wavelengths. Hot Jupiters are particularly interesting in this regard. Compared to the radio emitting planets in the solar system, hot Jupiters typically have much smaller star-planet distances (<0.1 au). The amount of energy incident on hot Jupiters from stellar winds should therefore be much higher. Extrapolating the radiometric Bode's law upwards, it is expected that radio emissions from hot Jupiters should be correspondingly larger (Stevens, 2005) and possibly detectable from Earth.

Despite repeated attempts, there have been no confirmed exoplanetary radio emission detections to date (Bastian et al., 2000; Ryabov et al., 2004; Lazio & Farrell, 2007; Smith et al., 2009; Lecavelier Des Etangs et al., 2009, 2011; Hallinan et al., 2013; Sirothia et al., 2014). Bastian et al. (2000) offer several possible reasons for the lack of detection. The observations may have been made at a frequency different to that of the radio emission or could simply have lacked the sensitivity required. Alternatively, the radio emissions, which

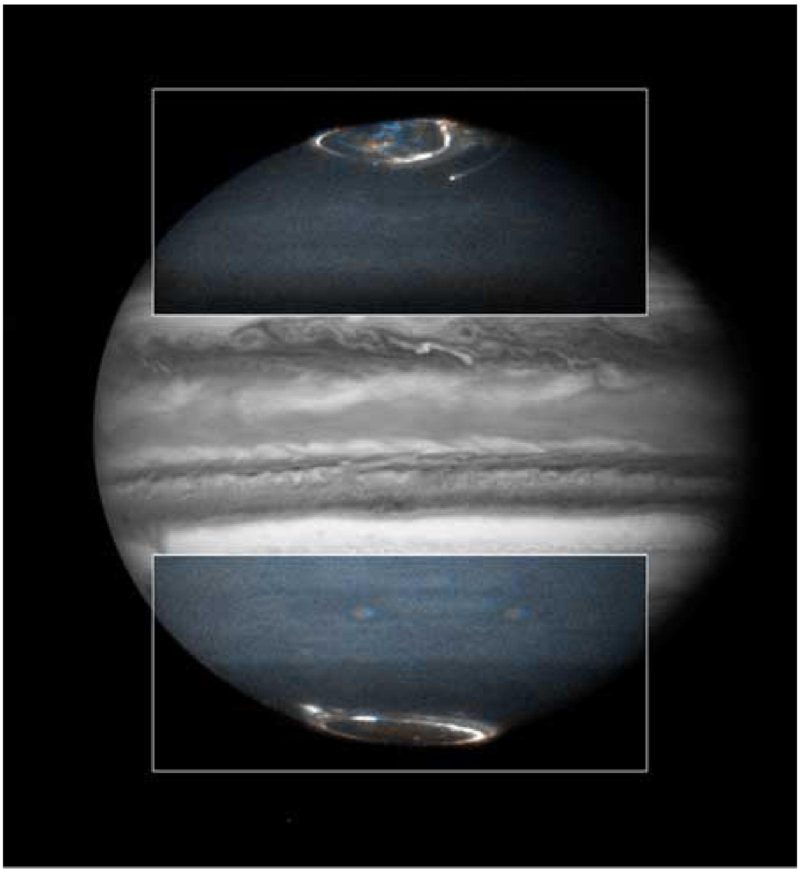

Figure 6.1: Image of Jupiter taken by NASA's Hubble Space Telescope. Overlayed are images of the auroral regions taken in UV. Auroral emissions are clearly visible in the auroral oval where radio emissions also originate from.

are believed to be emitted into a cone, may not have been beaming towards Earth. These explanations do not rule out the existence of exoplanetary radio emission, just our ability to detect it. The authors also argue that these systems could lack a source of keV electrons necessary to produce the emission. The lack of a detection would then be due to a genuine lack of emission. Lastly, the authors discuss the sporadic nature of radio emission. They argue that emissions above their detection threshold may exist but, due to emission variability, it was not detectable at the time of their observations.

Running in parallel with attempts to detect explanatory radio emissions are efforts to model the relevant physical processes in order to better inform the observations. Since planetary radio emissions can be traced back to stellar winds, progress in modelling the former is intrinsically tied to progress in modelling the latter. As discussed in section 1.5, advancing our understanding of stellar winds has been hampered due to the difficulty in observing them

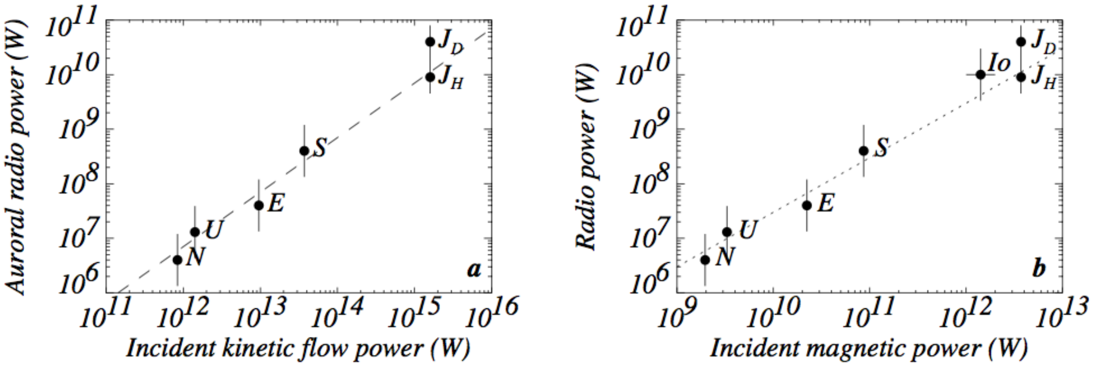

Figure 6.2: Radiometric Bode's law for the magnetised solar system planets. The figures show that the emitted radio power is proportional to the incident kinetic flow power (left) and the incident magnetic power (right) from the solar wind. Used with permission from (Zarka et al., 2001).

directly or indirectly. Some attempts at modelling radio emissions assumed a fixed value for stellar wind speeds (e.g. Stevens, 2005; Jardine & Collier Cameron, 2008). Other works have incorporated a radially varying wind speed (e.g. Grießmeier et al., 2007b) by using the wind model of Parker (1958). This resulted in improved radio emission predictions for close-in exoplanets where the stellar wind speed has not been accelerated to its terminal velocity. These types of radio emission models are all computationally cheap. Indeed, multiple authors have used them to systematically predict the radio emission from large samples of exoplanets with the aim of identifying the most promising candidates for future observation runs (Lazio et al., 2004; Grießmeier et al., 2007c; Jardine & Collier Cameron, 2008).

With few exceptions, emission variability has been neglected in radio emission models to date. Most assume stellar magnetic fields and winds that are both steady and isotropic. However, observations of the solar wind (e.g. Gosling, 1996), and modelling of stellar magnetic fields (e.g. Petit et al., 2008) and winds (e.g. Vidotto et al., 2009) show that this is not the case. Indeed, the dynamic nature of the solar wind is one of the factors, among others, known to affect the intensity of radio activity at Jupiter and Saturn (Zarka, 1998; Gurnett et al., 2002; Crary et al., 2005). More recent modelling efforts have incorporated three dimensional structure into stellar winds by using maps reconstructed with Zeeman-Doppler imaging (ZDI) (Fares et al., 2010; Vidotto et al., 2012, 2015). This type of approach accounts for variations in the wind along the planetary orbit. However, the ZDI maps that it is reliant on require a large amount of observation time. This makes it unfeasible to to apply this type of approach to a large sample of stars.

In this chapter I model the planetary radio emission from seven planet hosting systems, whose magnetic fields have been mapped and presented by Fares et al. (2013) using ZDI. In particular, I focus on HD 179949, HD 189733 and τ Boo. I incorporate these published magnetic maps into the radio emission model, as outlined in section 6.2, and consider the time-scales over which planetary radio emission variability might be expected.

The rest of the chapter will be structured as follows. In section 6.2, I outline the radio emission model. The sample of hot Jupiter hosting stars is discussed in section 6.3. In section 6.4, I discuss the results of the radio emission modelling for HD 179949b, HD 189733b, τ Boo b, and the rest of the sample and concluding remarks are given in section 6.5.

6.2 Radio emission model

The model of exoplanetary radio emission employed in this chapter is adapted from the model presented by Jardine & Collier Cameron (2008). Radio emissions originate from a population of electrons that have been accelerated in the current sheet that forms where the stellar and planetary magnetic fields interact. The power of the accelerated electrons is given by

$$P_{\mathrm{e}} = V_{\mathrm{cs}} \dot{n}_{\mathrm{run}} K, \tag{6.2}$$

where V_{cs} is the volume of the current sheet, $\dot{n}_{\mathrm{run}}$ is the rate at which runaway electrons are generated per unit volume, and K is the characteristic energy to which each electron is accelerated[1]. I take the acceleration region to be the size of the planetary magnetosphere, r_{ms}, with a fixed aspect ratio, α. Its volume is therefore given by $V_{\mathrm{cs}} = \pi r_{\mathrm{ms}}^2 \cdot \alpha r_{\mathrm{ms}} = \pi \alpha r_{\mathrm{ms}}^3$. The magnetosphere size, determined by pressure balance between the wind ram pressure, stellar magnetic pressure and planetary magnetic pressure, is given by

$$r_{\mathrm{ms}} = \left(\frac{B_{\mathrm{pl}}^2}{2\mu_0 n_{\mathrm{wind}} m_{\mathrm{p}} v_{\mathrm{eff}}^2 + B_\star^2(r_{\mathrm{orb}})} \right)^{1/6} r_{\mathrm{pl}}, \tag{6.3}$$

where B_{pl} is the planetary magnetic field strength, μ_0 is the permeability of free space, n_{wind} is the wind number density, m_{p} is the proton mass, v_{eff} is the effective wind speed (the speed at which the stellar wind impinges on the planetary magnetosphere, see equation 6.6), $B_\star(r_{\rm orb})$ is the stellar field strength at the orbit of the planet and $r_{\rm pl}$ is the planetary radius. As a brief aside, this equation has a slightly different form to the one I used to calculate $r_{\rm ms}$ in the previous chapter (equation (5.10)). Since hot Jupiters have small orbital distances compared to planets in the habitable zones of solar-type stars, the stellar magnetic pressure must be incorporated in order to accurately determine $r_{\rm ms}$.

---

[1] Jardine & Collier Cameron (2008) state the power in the accelerated electrons is given by $\pi R_m^2 v N_{\mathrm{run}} K$. However, the equation the authors give for the runaway electron number density, which they denote as N_{run} (their equation 13), is actually the rate at which runaway electrons are generated per unit volume with units of $\mathrm{m}^{-3}\mathrm{s}^{-1}$. The correct form is given by Eq. (6.2). This modification does not affect the scalings, and hence conclusions, drawn by these authors.

Jardine & Collier Cameron (2008) showed that the electric field, E, in the acceleration region determines the rate of runaway electron generation, $\dot{n}_{\rm run}$, and has a dependence given by

$$\frac{E}{E_{\rm D}} \propto \frac{v_{\rm eff} B_\star(r_{\rm orb})}{n_{\rm cs}}, \tag{6.4}$$

where $E_{\rm D}$ is the Dreicer field and n_{cs} is the density within the acceleration region. These authors also showed that the radiometric Bode's law for the Solar System planets can be reproduced if the density within the current sheet is enhanced by a factor, $f_{\rm comp}$, when compared to the solar wind density due to compression within this region, such that $n_{\rm cs} = f_{\rm comp} n_{\rm wind}$. Appendix 6.A contains further details of the parameters $\dot{n}_{\rm run}$, E, and $E_{\rm D}$. Finally, the radio flux density received at Earth, Φ, is given by

$$\Phi = \frac{P_{\rm rad}}{\Omega d^2 \delta f} \tag{6.5}$$

where $P_{\rm rad}$ is the radio emission power, Ω is the solid angle into which the emission is beamed, d is the distance to the system from Earth, and δf is the bandwidth which is set to be the cyclotron frequency, $eB_{\rm pl}/2\pi m_{\rm e}$ (Grießmeier et al., 2007b). Laboratory experiments have shown that roughly 10% of the power in the accelerated electrons is converted to radio emission such that $P_{\rm rad} = 0.1 P_{\rm e}$. For this study, I adopt values of K =10KeV, $\alpha = 10^{-8}$, Ω=1.6sr and $f_{\rm comp}$=15 which are characteristic values for these parameters, and Jovian parameters for the exoplanet.

Within this model, two factors control the magnitude and variability of radio emissions at each system. The wind density determines how large a pool of electrons is available for acceleration within the current sheet while the stellar magnetic field determines the amount of energy available to accelerate those electrons. Though the wind density decreases with orbital distance (roughly as r^{-2} once the wind is terminal), it does not vary significantly around the planetary orbit within this model. Instead, it is the stellar magnetic field structure that induces variability in the radio emissions.

A feature of this model is that the radio flux density received at Earth, (equation (6.5)), is independent of the assumed planetary field strength. A stronger field results in a larger planetary magnetosphere (equation. (6.3)). Since the volume of the current sheet is related to the magnetosphere size, $V_{\rm cs} \propto r_{\rm mp}^3$, a larger pool of electrons is available for acceleration (equation. (6.2)). The increased power is offset by increased losses, associated with a higher bandwidth, as the radio signal propagates to Earth (equation (6.5)). Since the frequency of radio emission depends on the planetary magnetic field strength (Zarka, 2007), which are observationally unconstrained, this model does not make a prediction on the frequency of radio flux density at Earth, just its magnitude.

The power of the accelerated electrons depends on the size of the magnetosphere, the effective velocity and the local electric field. These are determined by the large-scale flow in the wind and the stellar magnetic field. I will discuss these aspects of the model in more detail in the following subsections.

6.2.1 Stellar magnetic field extrapolation

In order to calculate how much magnetic energy is available from the stellar wind to be converted to radio emissions, the stellar magnetic field strength along the orbit of the exoplanet is first required (see equation (6.4)). This can be achieved by using the potential field source surface (PFSS) model, as outlined in section 2.2.3. The inner boundary, set at the stellar surface, is constrained by using a ZDI map while the outer boundary, known as the source surface, $r_{\rm ss}$, is forced to be purely radial, i.e. $B_\theta = B_\phi = 0$. Beyond the source surface, the field remains purely radial, decaying as an inverse square law.

For this work, I set the source surface to be $r_{\rm ss} = 3.41 r_\star$ which is consistent with published results (Fares et al., 2010). Examples of the ZDI maps used are shown in the top row of Fig. 6.3 for HD 179949 (Fares et al., 2012), HD 189733 (Fares et al., 2010) and τ Boo (Fares et al., 2013). On the second row, the magnetic field at the source surface is shown. Since higher order spherical harmonic modes decay more rapidly with distance away from the stellar surface, the field structure is predominantly dipolar at the source surface. This is true despite the more complex fields evident at the stellar surfaces shown in Fig. 6.3.

To carry out the field extrapolation, I use a modified version of the global diffusion code

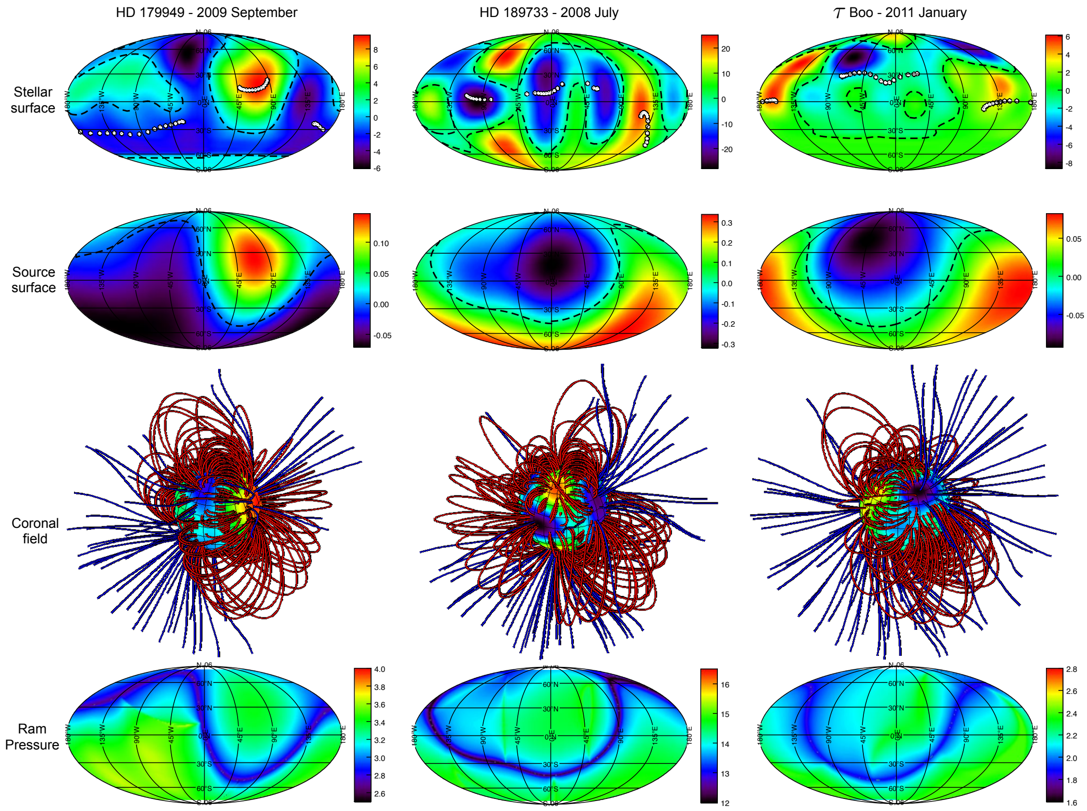

Figure 6.3: Examples of the magnetic field geometries of HD 179949 (2009 September), HD 189733 (2008 July), and τ Boo (2011 January). For each star, maps of the radial magnetic field at the stellar surface (first row) and source surface (second row) are shown. The colour bars indicate the magnetic field strengths in Gauss. Polarity inversion lines are shown with dashed lines. White dots on the surface maps indicate the foot points of the field lines that connect with the planet around the orbit. The large-scale 3D coronal field structure between the stellar surface and the source surface is also shown (third row). Closed and open field lines are coloured in red and blue respectively. Finally, the stellar wind ram pressure, for all latitudes and longitudes, at the orbit of the planet are shown in units of 10^{-6} dyne cm^{-2} (fourth row). All the stars display a complex field at the photosphere but a dipole dominated field exists at the source surface because higher order spherical harmonics decay more quickly with distance above the stellar surface. Three dimensional structure exists in the ram pressure and the stellar magnetic pressure (which has a structure similar to that seen in the second row).

of van Ballegooijen et al. (1998). The PFSS approach has previously been used to study a variety of stars (Jardine et al., 2002; Gregory et al., 2006; Lang et al., 2012; Johnstone et al., 2014). Examples of the 3D extrapolation for HD 179949, HD 189733, and τ Boo are shown in the third row of Fig. 6.3. The field lines are colour coded blue and red to represent open and closed field lines respectively.

6.2.2 Stellar wind

Equation (6.3) requires us to estimate two properties of the stellar wind. These are the effective wind velocity, i.e. the speed at which the interplanetary plasma impinges on the planetary magnetosphere from the reference frame of the planet, and the density of the wind. Both of these quantities may vary around the orbit of the planet.

For short-period planets, the effective velocity, v_{eff}, has a component from the wind velocity, v_{wind} and a component in the azimuthal direction, v_{az}, due to the orbital motion of the planet. The effective velocity is calculated by adding these components in quadrature,

$$v_{\text{eff}}^2 = v_{\text{az}}^2 + v_{\text{wind}}^2. \tag{6.6}$$

At the small orbital distances where hot Jupiters exist, the interplanetary plasma will be corotating with the star. The azimuthal velocity component is therefore given by $v_{\text{az}} = 2\pi r_{\text{orb}}/P_{\text{syn}}$ where r_{orb} is the orbital radius and $P_{\text{syn}} = \frac{P_{\text{rot}}P_{\text{orb}}}{P_{\text{rot}}-P_{\text{orb}}}$ is the synodic period of the planet with respect to the rotation of the star. P_{rot} and P_{orb} are the stellar rotation and planetary orbital periods respectively. In the rotating frame of the host star, it takes one synodic period for a planet to return to its starting position. Consequently, radio emissions are periodic with a time-scale given by the synodic period (Fares et al., 2010).

v_{wind} is calculated using a two step process. The wind speed is estimated at the source surface radius first. Solar wind speeds are known to correlate with the amount of field line divergence (Levine et al., 1977; Wang & Sheeley, 1990). Wang & Sheeley (1991) showed that such a correlation is plausible provided that the amount of Alfven wave energy flux is constant within open flux tubes. Building on the work of Wang & Sheeley (1990), Arge & Pizzo (2000) establish a continuous empirical relation between the magnetic expansion factor, f_s, and the solar wind velocity at the source surface of the Sun,

$$v_{\text{wind}}\left(r_{\text{ss}}\right) = 267.5 + \frac{410}{f_{\text{s}}^{2/5}}[\text{ms}^{-1}]. \tag{6.7}$$

The magnetic expansion factor is given by

$$f_{\text{s}} = \left(\frac{r_{\odot}}{r_{\text{ss}}}\right)^2 \frac{B(r_{\odot})}{B(r_{\text{ss}})}, \tag{6.8}$$

where $B(r_{\mathrm{ss}})$ is the magnetic field strength at a location on the source surface and $B(r_{\odot})$ is the magnetic field strength at the solar surface along the same magnetic field line. Since the so called Wang-Sheeley-Arge model is calibrated for the solar wind, I modify Eq. (6.8), replacing $r_{\odot}$ with $r_{\star}$. $B(r_{\star})$ and $B(r_{ss})$ are determined in the coronal field extrapolation by equations (2.39) - (2.41).

The second step is to propagate $v_{\mathrm{wind}}(r_{\mathrm{ss}})$ out to r_{orb}. Above the source surface, I assume that the wind evolves according to the model of Parker (1958). The wind velocity is found by integrating the momentum equation for the wind,

$$\rho m v_{\mathrm{wind}} \frac{\partial v_{\mathrm{wind}}}{\partial r} = -\frac{\partial}{\partial r}(\rho k_B T) - \rho m \frac{G\mathrm{M}_{\star}}{r^2}, \tag{6.9}$$

where ρ is the mass density, m is the average molecular mass, T is the isotropic wind temperature and the other symbols have their usual meanings. The wind temperature is chosen to match the velocities at the source surface. The wind velocity at the orbit of the planet can then be determined using this temperature. This approach to calculating the wind velocity allows the full 3D structure of the stellar magnetic field to be imprinted on the wind velocity. Thus the wind ram pressure varies around the planetary orbit in a way that is determined by the observed magnetic field geometry.

As discussed in section 1.5.2, no direct methods of observing the very low density winds of low-mass stars exist. Jardine & Collier Cameron (2008) use a scaled solar wind density in their model. These authors set the wind density to be $N_W = 1.7 \times 10^{-20}\,\mathrm{kgm}^{-3}$ at a distance of $r = 215 r_{\star}$ from the host star. The density at the exoplanet is then calculated according to mass conservation and assuming a wind that is terminal and radial, i.e. the wind density falls as r^{-2}. However, since I use a radially varying wind in this work, the density falls as $v_{\mathrm{wind}}^{-1} r^{-2}$ in order to conserve mass. Additionally, I scale the wind density by a factor, f_{mag}, where f_{mag} is the average foot point strength of the field lines that intersect the exoplanet's orbit normalised to the average Solar surface field (1G). Physically, f_{mag} accounts for the denser winds of more active stars (Mestel & Spruit, 1987). The density at the orbit of the planet is therefore given by

$$n_{\mathrm{wind}}(r) = 10^7 f_{\mathrm{mag}} \frac{v_{\mathrm{wind}}(r = 215 r_{\star})}{v_{\mathrm{wind}}(r)} \left(\frac{r_{\star}}{r_{\odot}}\right)^2 \left(\frac{r}{1\mathrm{AU}}\right)^{-2}. \tag{6.10}$$

The ram pressure of the wind on a shell at the orbital radius of the planet is shown in the last row of Fig. 6.3. The influence of the magnetic field structure can clearly be seen in the ram pressure structure.

6.3 Stellar system properties

In this chapter, I use the sample of seven hot Jupiter hosting stars presented by Fares et al. (2013) for which a ZDI map exists. In particular I focus on HD 179949, HD 189733 and τ Boo. Properties for these three systems are shown in Table 6.1 with details for the full sample available in Fares et al. (2013).

I choose these three systems for further discussion because they are often cited as promising targets for detectable exoplanetary radio emission (Lazio et al., 2004; Grießmeier et al., 2007c; Jardine & Collier Cameron, 2008) and have been extensively studied in the literature. In addition, these stars allow a comparison of two factors that affect exoplanetary radio emission. The first is the spectral type of the host star which affects the nature of the stellar wind. HD 179949, an F8 dwarf, and HD 189733, a K2 dwarf, allow us to make this comparison. The second is the relative angular velocity of the planet's orbital motion and the stellar rotational motion which determines whether the planet moves relative to the stellar magnetic field. The effect of this factor can be evaluated with HD 179949b and τ Boo b. Both planets have host stars with similar spectral types but the latter system is known to be tidally locked whilst the former is not.

HD 189733b and τ Boo b are known to orbit in, or close to, the stellar equatorial plane. Making use of the Rossiter-McLaughlin effect (Rossiter, 1924; McLaughlin, 1924), Triaud et al. (2009) determine the spin-orbit misalignment angle of HD 189733b to be $0.85^{\circ+0.32}_{-0.28}$. For τ Boo b, Brogi et al. (2012) find that the normal to the orbital plane is not significantly misaligned with the stellar rotation axis. For the purposes of this study, I will assume that both planets lie exactly in the stellar equatorial plane. For HD 179949b, Brogi et al. (2014) determine that the orbital inclination is $67.7^\circ \pm 4.3^\circ$. Fares et al. (2012) determine that the stellar inclination is roughly 60° using ZDI. Inclinations determined from ZDI can have errors of 10° or greater (e.g. Petit et al., 2008). I will assume a spin-orbit misalignment of 0° for HD 179949 since this is consistent with the stellar and orbital inclinations when considering the errors. Winn et al. (2010) note that hot Jupiter systems with hotter host stars ($T_{\rm eff}$ > 6250K) are more likely to have a large spin-orbit misalignment. Within the sample, HD 179949 and τ Boo are the hottest stars, with effective temperatures of 6168K and 6387K

Table 6.1: Properties of the HD 189733, HD 179949 and τ Boo systems. Listed are the spectral type, stellar mass and radius, planetary orbital radius, stellar rotation period, planetary orbital and synodic periods and distance from the Sun. All values referenced from Fares et al. (2013) with the exception of P_{syn} (calculated) and d (referenced below).

Parameter	HD 189733	HD 179949	τ Boo
SpT	K2V	F8V	F7V
$M_\star$ [$M_\odot$]	0.82	1.21	1.34
$r_\star$ [$r_\odot$]	0.76	1.19	1.42
r_{orb} [AU]	0.031	0.0439	0.048
P_{rot} [days]	12.5	7.6	3.31[a]
P_{orb} [days]	2.22	3.09	3.31
P_{syn} [days]	2.7	5.2	∞
d [pc]	19.3[b]	27.1[c]	15.6[d]

[a] Fares et al. (2013) use the equatorial rotation period of 3 days for τ Boo. I choose to use a rotation period 3.31 days, which is still consistent with the differential rotation exhibited by τ Boo, to explore the effects of a tidally locked planet.

[b] Fares et al. (2010), [c] Butler et al. (2006), [d] Grießmeier et al. (2007b)

respectively (Fares et al., 2013), and are the most likely to have large spin-orbit misalignments according to the trend noted by Winn et al. (2010). Nevertheless, I will proceed by assuming the planetary orbits are equatorial for the reasons given above. For the remaining, the spin-orbit misalignments are unknown since the planets are not transiting. For the purposes of this study, I assume that they also orbit within the stellar equatorial plane.

In terms of the geometry of the system, it is also important to consider the fact that the radio emission is anisotropic. The emissions are beamed into a cone which is aligned with the local planetary magnetic field (Zarka, 2007). If the magnetic dipole axis and planetary rotation axis are aligned, the radio emissions should be beamed in the direction of Earth at all times, if the geometry is favourable, or not at all. However, if there is a misalignment between the planetary magnetic dipole and rotation axes, then emissions, as observed from Earth, may be modulated on the planetary rotation period as the emission cone swings in and out of view from Earth. Given that I have no information about the planetary field alignment, I will assume the most favourable geometry, in which the radio emissions are always beamed towards Earth.

For each star in the sample, magnetic maps are reconstructed from spectropolarimetric observations. Two magnetic maps are available each for HD 179949 (Fares et al., 2012) and HD 189733 (Fares et al., 2010). For τ Boo, I use seven ZDI maps spanning four years (Donati et al., 2008a; Fares et al., 2009, 2013). ZDI maps for the remaining four stars are available in Fares et al. (2013). Fig. 6.3 shows examples of the magnetic field structure for HD 179949, HD 189733, and τ Boo. In each case, the radial component of the magnetic field at the stellar surface & source surface is shown, as well as the 3D coronal field structure between these two boundaries. Though complex structure is evident at the surface of each of the stars, it is predominantly the dipole component that survives at the source surface.

6.4 Results

6.4.1 HD 179949

Figure 6.4 shows magnetic maps at the source surface of HD 179949 (top row). These maps are obtained using the extrapolation process described in section 6.2.1 using magnetic maps of the stellar surface obtained during 2007 June and 2009 September (Fares et al., 2012). The colours represent the magnetic field strength in Gauss and the dashed lines represent polarity inversion lines, i.e. locations where $B_r = 0$. To calculate the expected planetary radio emission, the local stellar magnetic field strength in the vicinity of HD 179949b as it orbits over one synodic period is required. This is obtained by considering the stellar magnetic field strengths in the equatorial plane of the source surface maps and calculating the magnetic field strength at the distance of the planet according to an inverse square law decay. The local field strength has been plotted in the bottom row of Fig. 6.4 in blue as a function of the stellar longitude of the planet. The corresponding predicted radio flux received at Earth, over one synodic period, is also plotted in red. Figure 6.4 has been formatted such that the stellar longitudes of the top and bottom rows are aligned.

Over each synodic period (5.2 days), HD 179949b exhibits highly variable radio emission that correlates strongly with the local stellar field strength. The variability can be mostly attributed to the orbital motion of the planet through the stellar magnetic field. Comparing the source surface maps with the predicted radio flux curves, negligible emission occurs as the planet crosses the polarity inversion lines. Conversely, the highest emission occurs when the planet is over the magnetic poles, i.e. when the field strength is strongest. This is true during

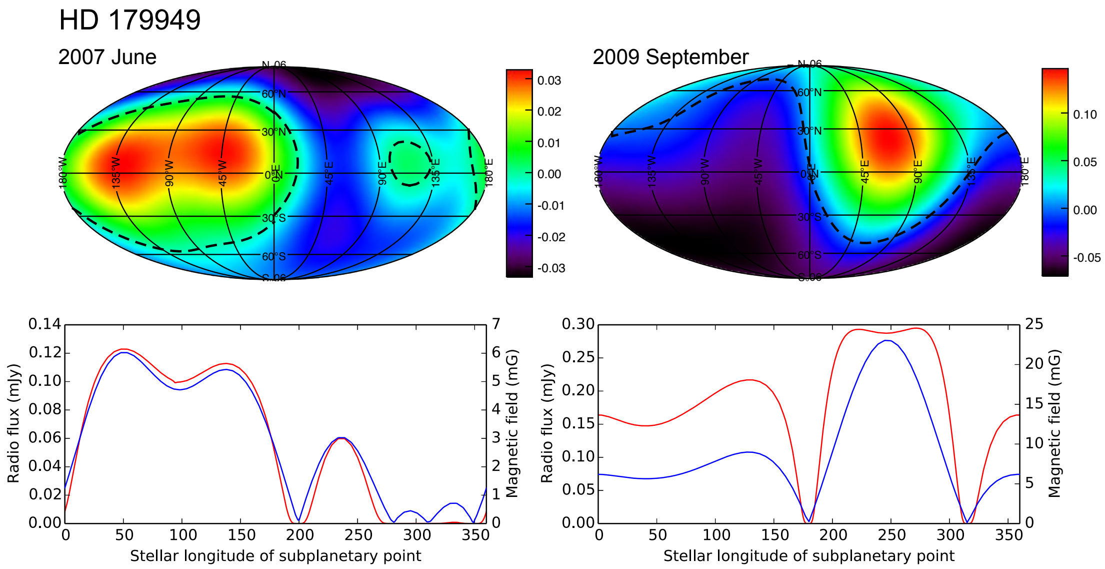

Figure 6.4: Properties of the HD 179949 system during the 2007 June (left) and 2009 September (right) epochs. Top: Magnetic field maps of the source surface displayed in the same format as Fig. 6.3. Bottom: Predicted planetary radio flux (red) and stellar magnetic field strength along the planetary orbit (blue) as a function of the stellar longitude of the subplanetary point. Large drops in radio emission are evident as the planet crosses the polarity inversion line.

both epochs, between which, the stellar field has evolved.

As well as planetary radio emission, several authors have suggested that magnetic interactions may also induce enhanced chromospheric activity near the stellar surface (Shkolnik et al., 2008; Lanza, 2009). Fares et al. (2012) searched for this type of interaction at HD 179949 finding hints of activity enhancement modulated at the synodic period of the system. Given that enhanced chromospheric activity and planetary radio emission are both thought to occur as a result of magnetic interactions between a planet and host star, it is unsurprising that both would be modulated on the synodic period.

6.4.2 HD 189733

Fig. 6.5, shows the same information as Fig. 6.4 but for the HD 189733 system. The ZDI maps used for the field extrapolations were presented by Fares et al. (2010). A comparison of Figs. 6.4 and 6.5 shows that HD 179949b and HD 189773b could both be expected to display strong variability, modulated on the synodic period of their respective systems during a given epoch. Given that both planets orbit stars where the dipole component of the magnetic field is tilted, the similarity is to be expected. The main difference between these systems is the

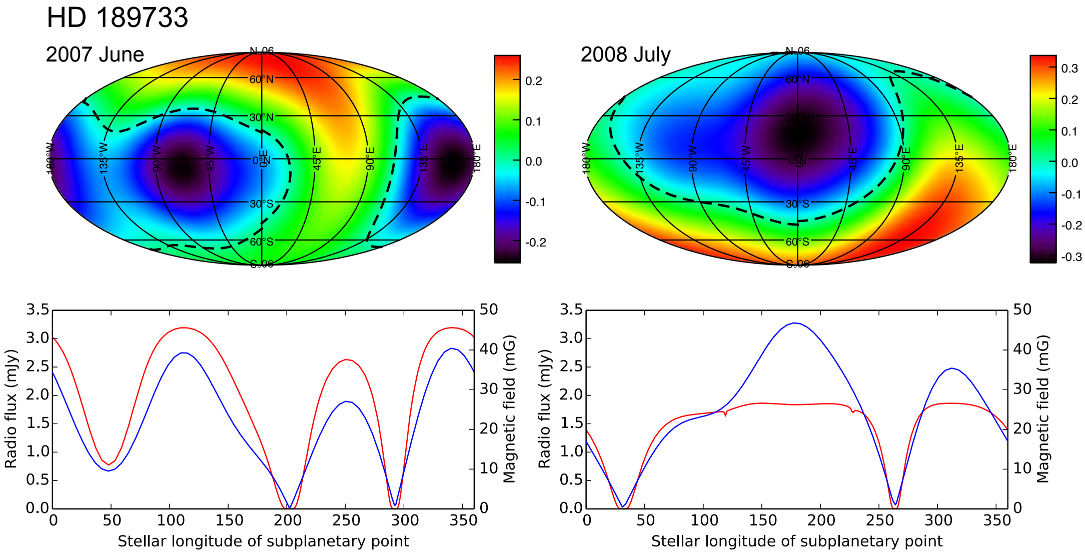

Figure 6.5: Properties of the HD 189733 system during the 2007 June (left) and 2008 July (right) epochs. Data displayed in the same format as Fig. 6.4.

magnitude of the radio flux density, smaller by roughly an order of magnitude at HD 179949b. This can be attributed to the lower photospheric magnetic field strength, the larger star-planet distance, and the greater distance from Earth for HD 179949.

Using the model presented by Grießmeier et al. (2007c), Fares et al. (2010) have also predicted the radio emission expected from HD 189733b. The shape of their radio flux curve as a function of subplanetary point is in agreement with ours though the magnitude of their radio emission is higher, reaching the hundreds of mJy, due to a higher conversion efficiency from the Poynting flux to radio emission.

A number of authors have searched for radio emission from HD 189733b. While none produced positive detections, 3σ upper limits of 2.1mJy, 2mJy, 81mJy, and 160μJy were found at frequencies of 150MHz (Lecavelier Des Etangs et al., 2011), 244MHz (Lecavelier Des Etangs et al., 2009), 307-347MHz (Smith et al., 2009), and 614MHz (Lecavelier Des Etangs et al., 2009) respectively. Recalling that the model presented in this chapter does not predict emission of a specific frequency, these limits can be compared to the predicted radio flux densities in Fig. 6.5. Assuming the predictions are correct, it is unsurprising that Smith et al. (2009) were not able to detect any radio emissions given their upper limit of 81mJy. However, at the other three frequency bands, the upper limits are either comparable, or significantly lower, than the predictions. Lecavelier Des Etangs et al. (2009) discuss several

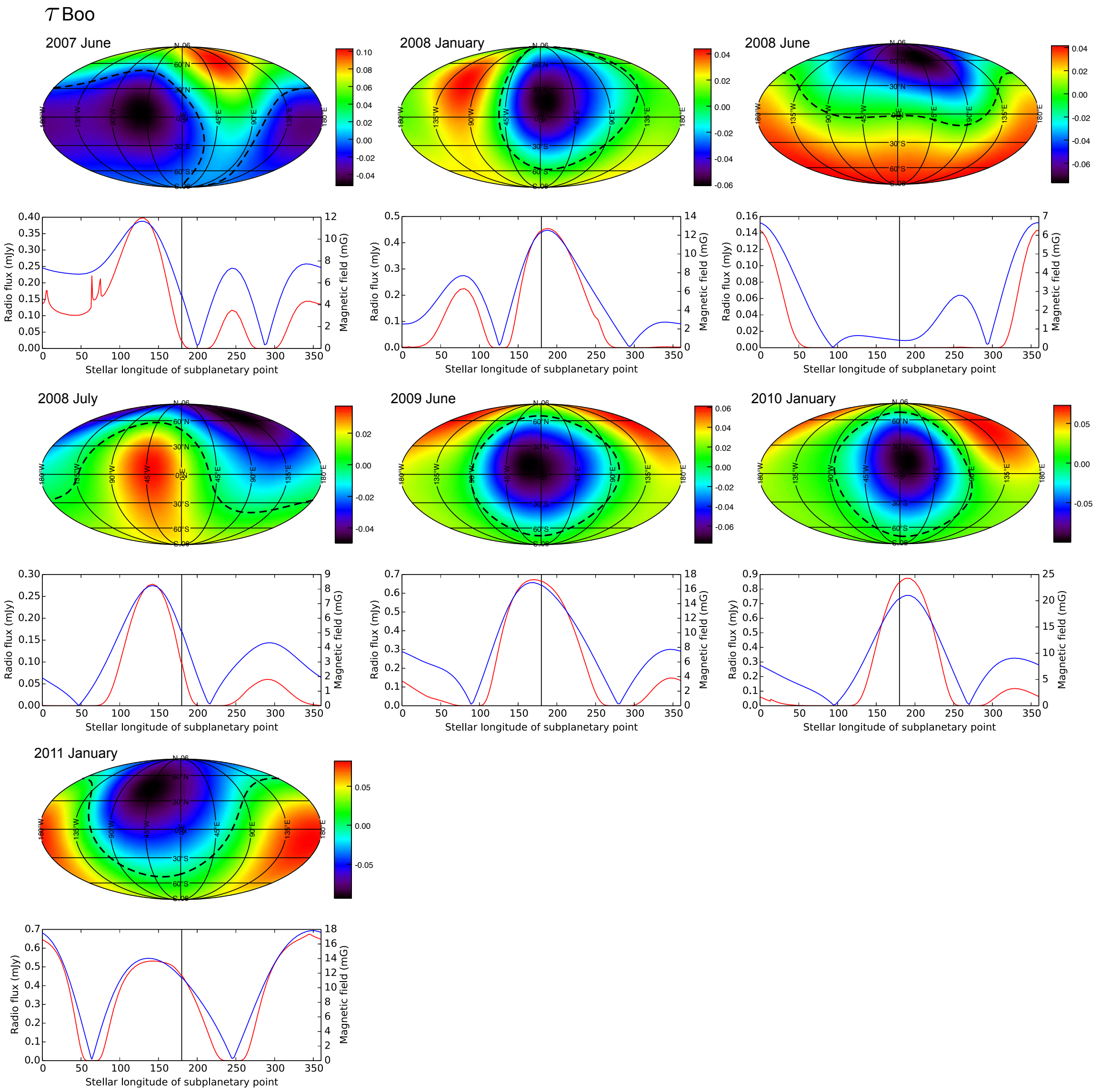

Figure 6.6: Properties of the τ Boo system over seven epochs. Data is displayed in the same format as Figure 6.5. The predicted radio flux displayed is that which could be expected if τ Boo b's subplanetary point sampled every stellar latitude. However it remains fixed at a single stellar longitude, 180°, due to tidal locking. Black vertical lines are included to indicate this longitude. The expected radio flux, at any given epoch, is given by the intersection of the red and black lines. Figure 6.7 shows how this flux varies with time.

reasons for the lack of detection and conclude that the most likely is because the emission was at a lower frequency.

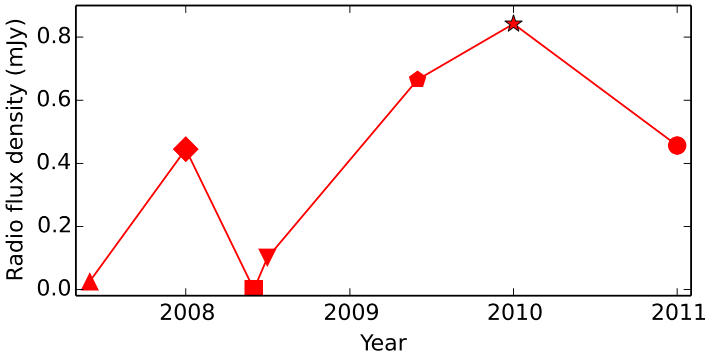

Figure 6.7: Predicted radio flux of τ Boo b as a function of time. The connecting lines are visual aids only and should not be interpreted as a form of interpolation. Each epoch is plotted with a different symbol to allow easier comparison with Figs. 6.8 and 6.9. In contrast to HD 189733, where the principle source of variability can be attributed to the orbital motion of the planet, variations in radio flux are caused by dynamo driven evolution of the stellar magnetic field.

6.4.3 τ Boo

Similarly to Figs. 6.4 and 6.5, I plot magnetic maps of the source surface and the predicted planetary radio emission for the τ Boo system in Fig. 6.6. I use seven ZDI maps, with epochs spread over three years (Donati et al., 2008a; Fares et al., 2009, 2013), for the field extrapolations of τ Boo.

Unlike the previous systems, the orbital motion of τ Boo b is tidally locked to its host star (Donati et al., 2008a). Consequently, the subplanetary point is fixed at one stellar longitude (180° in Fig. 6.6). Since there is no relative motion between planet and host star, radio emission variability from planetary motions through the stellar field no longer exists. The only source of variability, in this model, is from dynamo driven evolution of the stellar field between epochs. It is worth highlighting that this behaviour would not be seen from models where the stellar rotational velocity is neglected, such that the v_{az} component of v_{eff} is set to the Keplerian velocity of the planet. If v_{az} is non-zero, there must be some relative motion between the planet and the surrounding interplanetary plasma and magnetic field.

Given the lack of relative motion between host star and planet, the entire predicted radio curves in Fig. 6.6 would not be seen. Rather, these curves represent the expected radio flux if τ Boo b were not locked to its host star. In reality, one should only expect to see the radio flux indicated at 180° during each epoch, which has been highlighted by black vertical lines. The predicted radio flux from τ Boo b, as a function of time, is shown in Fig. 6.7 by collecting the

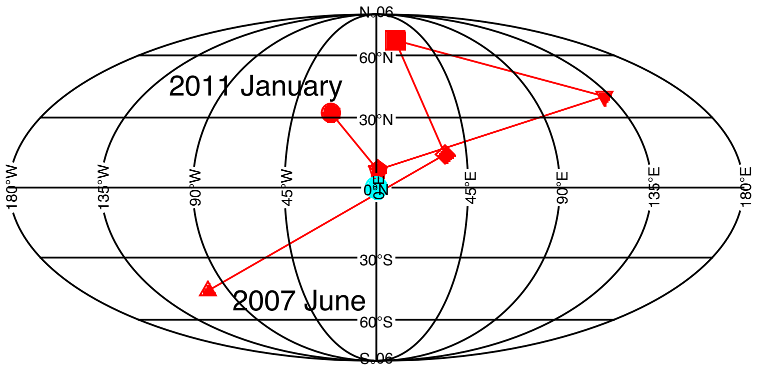

Figure 6.8: Location of the negative pole of the dipole component of τ Boo's magnetic field during each epoch. Lines connecting contiguous epochs are visual aids only and should not be interpreted as a form of interpolation. For each epoch, the symbol used is the same as that used in Fig. 6.7. The negative poles during 2009 June and 2010 January epochs are very close (latitude $\sim$8° and longitude $\sim$180°) and only appear to be a single data point in this plot.

radio fluxes, at 180° for each epoch, from Fig. 6.6 into one plot. A different symbol is used for each epoch to allow easier comparison between Figs. 6.7 - 6.9. This plot demonstrates that variability occurs over months/years, i.e. the time-scale of the field evolution. The predicted radio fluxes are of the same order of magnitude as those predicted by Vidotto et al. (2012) despite the differing models and assumptions used.

The radio flux variations in Fig. 6.7 occur due to evolution of the stellar field. The magnitude of the radio flux is highest when τ Boo b is over a magnetic pole, e.g. 2008 January, and weakest when it is over a magnetic cusp, e.g. 2008 June. Figure 6.8 shows the location of the negative pole of the dipole component (l=1 mode) during each epoch (red markers) and the subplanetary point (blue marker). Figure 6.9 shows the predicted radio flux as a function of angular separation between τ Boo b's subplanetary point and the nearest magnetic pole during each epoch (filled symbols if the nearest pole is negative and open symbols if it is positive). A clear trend of decreasing radio flux for increasing angular separation to the nearest magnetic pole is apparent. This result highlights the importance of knowing the three dimensional structure of the stellar magnetic field and not just the structure in the orbital plane of the exoplanet. It also argues for further ZDI observations of τ Boo which may allow us to determine any periodic behaviour in its large-scale magnetic field. If the evolution of the dipole component could be predicted, some estimate of the radio flux in the future could be made.

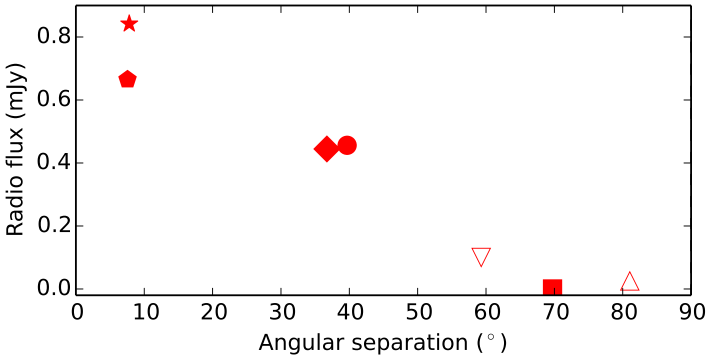

Figure 6.9: Radio flux as a function of angular separation between the subplanetary point and the closest magnetic pole of τ Boo during each epoch. Symbol shapes correspond to those used in Figs. 6.7 and 6.8. Filled symbols are used if the nearest pole is negative (the points plotted in Fig. 6.8) and unfilled symbols are used if the nearest pole is positive (antipodal to those in Fig. 6.8). A trend of decreasing radio flux can clearly be seen for increasing angular separation from the nearest stellar magnetic pole.

6.4.4 Rest of sample

From the sample of Fares et al. (2013), four further stars had detectable magnetic fields with one ZDI map existing for each. None of these planets are tidally locked to their host star. If any of these planets are radio emitters, all should show variability as a result of their orbital motions. Table 6.2 shows the predicted maximum planetary radio flux received at Earth per synodic period and the synodic period for each of these systems. None of these planets are predicted to be particularly strong radio emitters. Vidotto et al. (2015) have also calculated the radio fluxes emitted from these exoplanets. With the exception of HD 130322, they find fluxes that are roughly comparable (within a factor of a few to these results). These exoplanets have such low radio fluxes for similar reasons as those given to explain HD 179949b's lower radio flux density compared to HD 189733b's, namely low photospheric magnetic field strengths, large star-planet distances, and large distances to Earth. The combination of these factors means that these systems are not ideal targets for future planetary radio observations.

6.5 Discussion & Conclusion

I have presented a planetary radio emission model that incorporates a realistic geometry for the large-scale stellar magnetic field. Additionally, this model estimates the effective wind velocity, v_{eff}, more accurately than existing models in the literature. An accurate estimate should

Table 6.2: Maximum predicted planetary radio fluxes for the rest of the systems presented by Fares et al. (2013).

HD No.	102195	130322	46375	73256
Φ_{max} [mJy]	0.062	6.0×10^{-4}	0.018	0.19
P_{syn} [days]	6.2	18.2	3.3	3.1

include a wind component, v_{wind}, that accelerates radially, and an azimuthal component, v_{az}, that accounts for the exoplanetary orbital motion relative to the stellar rotation. Stevens (2005) assumes $v_{\text{eff}} = v_{\text{wind}} = 400\text{kms}^{-1}$ but do not include an azimuthal component. This is likely to be an overestimate of v_{wind} for hot Jupiters and an underestimate of v_{az}. Jardine & Collier Cameron (2008) assume $v_{\text{eff}} = v_{\text{az}}$ for planets orbiting close to their host star. These authors account for the stellar rotation but do not include a wind component. Grießmeier et al. (2007b) incorporates a radially accelerating wind component and an azimuthal component. However, they do not account for the stellar rotation and so overestimate values for v_{az} and hence v_{eff}. These examples demonstrate the need for careful consideration of the stellar system dynamics when calculating the effective velocity parameter.

Focusing on the HD 179949, HD 189733 and τ Boo planetary systems, I looked at the time-scales on which exoplanetary radio emissions may vary. I find that planetary radio emissions are strongly dependent on local stellar magnetic field strength along the exoplanetary orbit. Therefore, exoplanetary radio emissions could be used as a probe of the stellar magnetic field geometry.

In general, the height of magnetic loops on the surface of cool stars are comparable to their foot point separation. Therefore, higher order multipoles will decay more rapidly with height above the stellar surface. These higher order modes will contribute to the variability in the radio emissions of exoplanets that are orbiting close to the stellar surface of their host star. However, exoplanets at larger orbital radii, such as those studied in this chapter, will predominantly experience the dipole component of the stellar field. Emission maxima exist when the planet is above a pole while a minima would be expected inside a magnetic cusp. In general, the magnitude of radio emission is anticorrelated with the angular separation between the subplanetary point and the closest magnetic pole.

I find two time-scales for variability. The shorter time-scale is the synodic period of the planetary system and is caused by the orbital motion of the planet. From the reference frame of the planet, the local stellar magnetic field strength is constantly varying causing corresponding variations in the radio emission, typically on the order of days. This type of behaviour, which is exhibited by the HD 179949 and HD 189733 systems, has implications for future observations. It is similar to the behaviour described by Llama et al. (2013) with respect to observing early ingresses for transiting exoplanets. In both cases, unfavorable wind conditions may lead to a lack of detection and highlights the importance of considering the field/wind conditions when planning future observations.

The longer time-scale is most apparent in systems where the orbital and stellar rotation periods are similar in length. This results in a very long synodic period. In the most extreme case, when the stellar rotation period and orbital period are equal, there is no relative motion between planet and the stellar atmosphere in the azimuthal direction. For such systems, e.g. τ Boo, variability only occurs as a result of stellar magnetic field evolution. Previous models which estimate the azimuthal component of the effective velocity to be the Keplerian speed of the planet do not predict this type of behaviour for tidally locked systems. Indeed, by definition, the effective velocity in such systems cannot have a non-zero azimuthal component. One would expect variability at locked systems to occur over a characteristic time given by the magnetic cycle period. Non tidally locked systems will display variability on this time-scale as well but the time-scale for variability as a result of orbital motions will be much shorter.

Future exoplanetary radio emission detection attempts should focus on exoplanets orbiting close to stars with with strong magnetic fields and which are close to Earth. Additionally, the exoplanet would ideally have a large orbital velocity in the rotating frame of its host star. This would result in a higher azimuthal component of the effective wind velocity and hence higher Poynting flux.

6.A Runaway electron generation and the acceleration region

The component of the electric field that is parallel to the magnetic field in the acceleration region is given by

$$E = -\frac{2\sqrt{2\pi}}{\Gamma(1/4)} H^{-1/4} v_{\text{eff}} B_{\star}(r_{\text{orb}}), \tag{6.11}$$

where H is the magnetic Reynolds number and the remaining symbols are defined in the main text. This is the full version of Eq. (6.4). Jardine & Collier Cameron (2008) give a full derivation and discussion of this expression. In a plasma, the motions of the electrons, under the action of an electric field, are opposed by a drag force caused by coulomb collisions. For electrons with high enough velocities, the coulomb drag becomes negligible and the electrons can freely run out of the distribution. The exact behaviour is determined by the strength of the electric field. Below a critical field strength, known as the Dreicer field (Dreicer, 1959), only the electrons in the high velocity tail of the distribution runs away. However, at super-Dreicer strengths, the entire distribution is able to do so. The Dreicer field is given by

$$E_{\mathrm{D}} = 18 \times 10^{-12} n_{\mathrm{cs}} T^{-1}, \tag{6.12}$$

where the n_{cs} and T are the electron density and temperature respectively inside the current sheet. Due to compression of the plasma within the current sheet, the density does not necessarily take on the wind value. Both the compressed density and temperature in the current sheet are unknown. We find that an increase in the density by a factor of 15 and a temperature of 1MK reproduces the emitted radio power at the solar system planets well and adopt these values. The rate at which runaway electrons is given by Kruskal & Bernstein (1964):

$$\begin{aligned} \dot{n}_{\mathrm{run}} &= 0.35 n_{\mathrm{cs}} \nu_c f(E/E_{\mathrm{D}}) \\ &= 2.6 \times 10^{-5} n_{\mathrm{cs}}^2 T^{-3/2} f(E/E_{\mathrm{D}}) \end{aligned} \tag{6.13}$$

where ν_{c} is the electron collision frequency and $f(E/E_{\mathrm{D}})$ is given by

$$f\left(\frac{E}{E_{\mathrm{D}}}\right) = \left(\frac{E_{\mathrm{D}}}{E}\right)^{3/8} \exp\left[-\left(\frac{2E_{\mathrm{D}}}{E}\right)^{1/2} - \frac{E_{\mathrm{D}}}{4E}\right]. \tag{6.14}$$

7

Conclusions and outlook

The presence of magnetic fields on low-mass cool dwarfs is important to a wide range of phenomena, both on the star itself and in its surrounding environments. They are responsible for driving activity phenomena (flares, coronal mass ejections & winds), affect the rotational evolution of a star over its lifetime (disc braking on the pre-main sequence and spin-down resulting from winds) and have profound consequences for exoplanets (wind-planet interactions and effects on habitability). In this thesis, I have considered some of these aspects of stellar magnetism which I will summarise in this chapter before looking to the future of some of these fields.

7.1 Magnetic properties of low-mass dwarfs

Zeeman-Doppler imaging (ZDI) has been used to characterise the magnetic properties of cool dwarfs for two decades. This technique has allowed the community to investigate how the large-scale magnetic fields of these stars vary as a function of stellar mass (Donati et al., 2008a; Morin et al., 2008b, 2010; Gregory et al., 2012), rotation (Petit et al., 2008) and age (Vidotto et al., 2014; Folsom et al., 2016) as well as to assess their evolution on yearly time-scales (Donati et al., 2008b; Fares et al., 2009; Jeffers et al., 2014; Boro Saikia et al., 2015).

In chapter 3, I analysed the magnetic topologies of a sample of stars looking for trends that will further our understanding of stellar magnetism. Some of these results build on existing ZDI results. For example, Morin et al. (2010) have already demonstrated that there is a break in the large-scale magnetic field properties of cool stars at $\sim 0.5\,\mathrm{M}_{\odot}$ as a result of a change in internal structure. I find further evidence of this by showing that the toroidal energy has a different power law dependence on the poloidal energy for fully convective stars and stars with radiative cores.

I also explored the activity-rotation relation in this chapter. Vidotto et al. (2014) previously showed that stellar magnetism follows the activity-rotation relation, which is well known from X-ray studies. I found that the poloidal and toroidal components each individually follow the activity-rotation relation. There is some evidence that the fully convective M dwarfs fall into the saturated regime while higher-mass stars with radiative cores fall into the unsaturated regime, though this may be an effect of biases in the sample used.

As well as these results that are based on existing work, I find results that are entirely new and novel. One key result is the relationship between the axisymmetric and toroidal components of the field. I demonstrate that stars that are strongly toroidal are also strongly axisymmetric, i.e. that strong toroidal fields must be generated axisymmetrically. I also find that the orientation of the poloidal fields seem to have no bearing on the orientation of the toroidal fields. These observations represent new constraints for future theoretical dynamo simulations.

In chapter 4, I again analyse the large-scale magnetic topologies of low-mass stars. However, in this chapter, I do so with a specific focus on magnetic activity cycles. Previous works have found that activity cycle periods appear to lie on multiple branches which have been labelled the active and inactive branches (Brandenburg et al., 1998; Saar & Brandenburg, 1999; Böhm-Vitense, 2007). I find that the magnetic topologies of stars on each of these branches appears to be distinct. Inactive branch stars remain dominantly poloidal throughout their entire cycle while active branch stars are able to generate significant toroidal fields. This result may be a hint that the dominant shear layer contributing to dynamo action is different for stars on the two branches. However, the sample used in this chapter is still relatively small. It is not clear at this stage whether this result will hold when more stars are mapped with ZDI.

7.2 Exoplanet-wind interactions

Stellar winds are driven by the several million degree coronae of low-mass stars. Although the precise mechanisms by which they are heated to such high temperatures is not currently known, there is a consensus that the stellar magnetic field must play an important role. Within the solar system, the solar wind interacts with planetary atmospheres and magnetospheres in a variety of different ways. It is expected that similar interactions will also occur between stellar winds and exoplanets.

In chapter 5, I discuss the ingredients that a planet suitable to life must have. In particular, I focus on whether habitable zone (HZ) exoplanets are able to maintain magnetospheres large enough to protect their atmospheres from the erosive effects of stellar winds. Due to the small distance between M dwarfs and their HZs, exoplanets in the HZs of these stars are unlikely to have very large magnetospheres (Vidotto et al., 2013). There is also evidence that exoplanets around more massive stars are unlikely to have large magnetospheres. These host stars have more vigorous convective motions that drive stronger winds. It therefore seems that intermediate-mass stars ($0.6\,\mathrm{M}_\odot$ - $0.8\,\mathrm{M}_\odot$), whose HZs are not too close in and whose winds are not too strong, are the best candidates around which to look for habitable planets.

In chapter 6, I studied the radio emissions that can be expected from exoplanets as a result of stellar wind interactions. While there have been no confirmed exoplanetary radio emission detections to date, it is thought that, once detected, they will provide useful information about the exoplanet itself. Using a wind model and magnetic maps obtained form ZDI, I estimate the radio emission that could be expected from a sample of hot Jupiters. I find that emission variability is driven by the orbital motions of the planet as well as evolution of the stellar magnetic field as a result of dynamo action. One key finding is that the magnitude of emissions depends strongly on the angular separation between the magnetic dipole axis and the subplanetary point. This highlights the need to characterise the host star magnetic field when trying to learn about exoplanets.

7.3 Outlook

While ZDI has improved our understanding of stellar magnetism a great deal in the last two decades, there is still a great deal that is unknown. One example of such a gap in our knowledge is the temporal evolution of stellar magnetic fields on the time-scale of months and years. While a handful of stars have had their fields mapped over multiple epochs (Fares et al., 2013; Jeffers et al., 2014; Boro Saikia et al., 2015), there has not been a systematic study into the types of temporal evolution one could expect to see as a function of fundamental stellar parameters. Another question that remains unanswered is the reason for the bimodality seen in the lowest mass M dwarfs. It is expected that these and other related question will be effectively tackled with further ZDI campaigns.

On the exoplanet side of things, the hunt for a true Earth analogue is still ongoing. It is hoped that new missions, such as TESS (launch: 2017), JWST (launch: 2018) and PLATO (launch: 2024), that will follow on from the seminal Kepler mission, will be able to accomplish this task. Given the results of chapter 5, the PLATO mission is particularly relevant since its stated goal is to search for exoplanets in the HZs of solar-mass stars rather than in the HZs of lower-mass M dwarfs. However, these missions will have to deal with the problem of stellar activity jitter. The radial velocity signal of an Earth-mass planet in the HZ of a solar-mass star will be comparable to the radial velocity signal of the stellar activity from the host star. Therefore extra care will be needed to disentangle the two signals (e.g. Haywood et al., 2014).

The advent of the SPiRou instrument is a particularly exciting development in the context of ZDI studies as well as planet hunting. This is a NIR spectropolarimeter and velocimeter that is due to see first light in 2018. Its main science goals are to characterise rocky exoplanets in the HZs of M dwarfs. Additionally it will also characterise the magnetic fields of 100s of cool dwarfs. Since SPiRou incorporates a spectropolarimeter and a velocimeter into a single instrument, it will be able to simultaneously characterise an exoplanet and the magnetic activity of its host star allowing the two radial velocity signals to be more easily disentangled (Petit et al., 2015; Donati et al., 2015). This should allow for the detection of exoplanets that are even smaller than the smallest currently known exoplanets.

Bibliography

Altschuler, M. D., & Newkirk, G. 1969, solphys, 9, 131

Arge, C. N., & Pizzo, V. J. 2000, J. Geophys. Res., 105, 10465

Armstrong, D. J., Pugh, C. E., Broomhall, A.-M., Brown, D. J. A., Lund, M. N., Osborn, H. P., & Pollacco, D. L. 2016, MNRAS, 455, 3110, 1511.05306

Babcock, H. W. 1947, ApJ, 105, 105

Balikhin, M., Gedalin, M., & Petrukovich, A. 1993, Phys. Rev. Lett., 70, 1259

Baliunas, S. L. et al. 1995, ApJ, 438, 269

Baliunas, S. L., Henry, G. W., Donahue, R. A., Fekel, F. C., & Soon, W. H. 1997, ApJl, 474, L119

Baraffe, I., Chabrier, G., Allard, F., & Hauschildt, P. H. 1998, A&A, 337, 403, astro-ph/9805009

Barnes, J. R., Jeffers, S. V., & Jones, H. R. A. 2011, MNRAS, 412, 1599, 1011.1125

Barnes, S. A. 2003, ApJ, 586, 464, astro-ph/0303631

Bastian, T. S., Dulk, G. A., & Leblanc, Y. 2000, ApJ, 545, 1058

Benz, A. O. 2008, Living Reviews in Solar Physics, 5

Biermann, L. 1951, zap, 29, 274

Böhm-Vitense, E. 2007, ApJ, 657, 486

Boro Saikia, S., Jeffers, S. V., Petit, P., Marsden, S., Morin, J., & Folsom, C. P. 2015, A&A, 573, A17, 1410.8307

Borrero, J. M., & Ichimoto, K. 2011, Living Reviews in Solar Physics, 8, 1109.4412

Borucki, W. J. et al. 2012, ApJ, 745, 120, 1112.1640

Bouvier, J. et al. 2007, A&A, 463, 1017, astro-ph/0611787

Braithwaite, J., & Spruit, H. C. 2004, Nat, 431, 819, astro-ph/0502043

Brandenburg, A., Saar, S. H., & Turpin, C. R. 1998, ApJ, 498, L51

Brogi, M., de Kok, R. J., Birkby, J. L., Schwarz, H., & Snellen, I. A. G. 2014, A&A, 565, A124, 1404.3769

Brogi, M., Snellen, I. A. G., de Kok, R. J., Albrecht, S., Birkby, J., & de Mooij, E. J. W. 2012, Nat, 486, 502, 1206.6109

Broomhall, A.-M., Chaplin, W. J., Elsworth, Y., & Simoniello, R. 2012, MNRAS, 420, 1405, 1111.2492

Brown, B. P., Browning, M. K., Brun, A. S., Miesch, M. S., & Toomre, J. 2010, ApJ, 711, 424, 1011.2831

Brown, S. F., Donati, J.-F., Rees, D. E., & Semel, M. 1991, aap, 250, 463

Browning, M. K., Miesch, M. S., Brun, A. S., & Toomre, J. 2006, ApJl, 648, L157, astro-ph/0609153

Brun, A. S., Browning, M. K., & Toomre, J. 2005, ApJ, 629, 461, astro-ph/0610072

Butler, R. P., & Marcy, G. W. 1996, ApJ, 464, L153

Butler, R. P. et al. 2006, ApJ, 646, 505, astro-ph/0607493

Catala, C., Donati, J.-F., Shkolnik, E., Bohlender, D., & Alecian, E. 2007, MNRAS, 374, L42, astro-ph/0610758

Chabrier, G., & Baraffe, I. 1997, A&A, 327, 1039, astro-ph/9704118

Chabrier, G., & Küker, M. 2006, A&A, 446, 1027, astro-ph/0510075

Chandrasekhar, S. 1961, Hydrodynamic and hydromagnetic stability

Charbonneau, P. 2010, Living Reviews in Solar Physics, 7, 3

Charbonneau, P., & MacGregor, K. B. 2001, ApJ, 559, 1094

Chen, P. F. 2011, Living Reviews in Solar Physics, 8

Cohen, O., Ma, Y., Drake, J. J., Glocer, A., Garraffo, C., Bell, J. M., & Gombosi, T. I. 2015, ApJ, 806, 41, 1504.06326

Cranmer, S. R., & Saar, S. H. 2011, ApJ, 741, 54, 1108.4369

Cranmer, S. R., van Ballegooijen, A. A., & Edgar, R. J. 2007, ApJs, 171, 520, arXiv:astro-ph/0703333

Crary, F. J. et al. 2005, Natur, 433, 720

Crowe, S. A., Døssing, L. N., Beukes, N. J., Bau, M., Kruger, S. J., Frei, R., & Canfield, D. E. 2013, Nat, 501, 535

De Moortel, I., & Browning, P. 2015, Philosophical Transactions of the Royal Society of London Series A, 373, 20140269, 1510.00977

DeRosa, M. L., Brun, A. S., & Hoeksema, J. T. 2012, ApJ, 757, 96, 1208.1768

Desch, M. D., & Kaiser, M. L. 1984, Natur, 310, 755

do Nascimento, J. D. et al. 2014, in IAU Symposium, Vol. 302, IAU Symposium, 142–143, 1310.7620

do Nascimento, Jr., J.-D., Saar, S. H., & Anthony, F. 2015, in Cambridge Workshop on Cool Stars, Stellar Systems, and the Sun, Vol. 18, 18th Cambridge Workshop on Cool Stars, Stellar Systems, and the Sun, ed. G. T. van Belle & H. C. Harris, 59–64

Donahue, R. A. 1998, in Astronomical Society of the Pacific Conference Series, Vol. 154, Cool Stars, Stellar Systems, and the Sun, ed. R. A. Donahue & J. A. Bookbinder, 1235

Donati, J.-F. 1999, MNRAS, 302, 457

Donati, J.-F., & Brown, S. F. 1997a, aap, 326, 1135

——. 1997b, A&A, 326, 1135

Donati, J.-F., Catala, C., Landstreet, J. D., & Petit, P. 2006a, in Astronomical Society of the Pacific Conference Series, Vol. 358, Astronomical Society of the Pacific Conference Series, ed. R. Casini & B. W. Lites, 362

Donati, J.-F., Collier Cameron, A., Hussain, G. A. J., & Semel, M. 1999, MNRAS, 302, 437

Donati, J.-F., Collier Cameron, A., & Petit, P. 2003a, MNRAS, 345, 1187, astro-ph/0307448

Donati, J.-F. et al. 2003b, MNRAS, 345, 1145

——. 2015, MNRAS, 453, 3706, 1509.02110

——. 2006b, MNRAS, 370, 629, astro-ph/0606156

Donati, J.-F., & Landstreet, J. D. 2009, , 47, 333, 0904.1938

Donati, J.-F. et al. 2008a, MNRAS, 390, 545, 0809.0269

——. 2008b, MNRAS, 385, 1179, 0802.1584

Donati, J.-F., Semel, M., Carter, B. D., Rees, D. E., & Collier Cameron, A. 1997, MNRAS, 291, 658

Dreicer, H. 1959, Physical Review, 115, 238

Dressing, C. D., & Charbonneau, D. 2013, ApJ, 767, 95, 1302.1647

Ebert, R. W., McComas, D. J., Elliott, H. A., Forsyth, R. J., & Gosling, J. T. 2009, Journal of Geophysical Research (Space Physics), 114, A01109

Edberg, N. J. T. et al. 2011, Journal of Geophysical Research (Space Physics), 116, 9308

——. 2010, grl, 37, 3107

Fares, R. et al. 2009, MNRAS, 398, 1383, 0906.4515

——. 2012, MNRAS, 423, 1006, 1202.4472

——. 2010, MNRAS, 406, 409, 1003.6027

Fares, R., Moutou, C., Donati, J.-F., Catala, C., Shkolnik, E. L., Jardine, M. M., Cameron, A. C., & Deleuil, M. 2013, MNRAS, 435, 1451, 1307.6091

Farrell, W. M., Desch, M. D., & Zarka, P. 1999, J. Geophys. Res., 104, 14025

Folsom, C. P. et al. 2016, MNRAS, 457, 580, 1601.00684

Fossati, L. et al. 2010, ApJ, 714, L222, 1005.3656

Fressin, F. et al. 2012, Nat, 482, 195, 1112.4550

Gallet, F., & Bouvier, J. 2013, A&A, 556, A36, 1306.2130

——. 2015, A&A, 577, A98, 1502.05801

Gastine, T., Morin, J., Duarte, L., Reiners, A., Christensen, U. R., & Wicht, J. 2013, A&A, 549, L5, 1212.0136

Gosling, J. T. 1996, ARA&A, 34, 35

Granzer, T. 2002, Astronomische Nachrichten, 323, 395

Gregory, S. G., Donati, J.-F., Morin, J., Hussain, G. A. J., Mayne, N. J., Hillenbrand, L. A., & Jardine, M. 2012, ApJ, 755, 97, 1206.5238

Gregory, S. G., Jardine, M., Collier Cameron, A., & Donati, J.-F. 2006, MNRAS, 373, 827, astro-ph/0609667

Grießmeier, J.-M., Preusse, S., Khodachenko, M., Motschmann, U., Mann, G., & Rucker, H. O. 2007a, , 55, 618

——. 2007b, Planet. Space Sci., 55, 618

Grießmeier, J.-M. et al. 2004, A&A, 425, 753

Grießmeier, J.-M., Zarka, P., & Spreeuw, H. 2007c, A&A, 475, 359, 0806.0327

Grunhut, J. H., Wade, G. A., & the MiMeS Collaboration. 2011, ArXiv e-prints, 1108.2673

Guhathakurta, M., Holzer, T. E., & MacQueen, R. M. 1996, ApJ, 458, 817

Gurnett, D. A. et al. 2002, Natur, 415, 985

Hale, G. E. 1908, ApJ, 28, 315

——. 1913, ApJ, 38, 27

Hale, G. E., Seares, F. H., van Maanen, A., & Ellerman, F. 1918, ApJ, 47, 206

Hall, J. C., Lockwood, G. W., & Skiff, B. A. 2007, AJ, 133, 862

Hallinan, G., Sirothia, S. K., Antonova, A., Ishwara-Chandra, C. H., Bourke, S., Doyle, J. G., Hartman, J., & Golden, A. 2013, ApJ, 762, 34, 1210.8259

Harmanec, P., & Prša, A. 2011, PASP, 123, 976, 1106.1508

Hart, M. H. 1978, Icarus, 33, 23

Hathaway, D. H. 2015, Living Reviews in Solar Physics, 12

Haywood, R. D. et al. 2014, MNRAS, 443, 2517, 1407.1044

Howard, A. W. et al. 2013, Nat, 503, 381, 1310.7988

Howe, R., Christensen-Dalsgaard, J., Hill, F., Komm, R. W., Larsen, R. M., Schou, J., Thompson, M. J., & Toomre, J. 2000, Science, 287, 2456

Huang, S.-S. 1960, Am. Sci., 202, 55

Jackson, B., Barnes, R., & Greenberg, R. 2008, MNRAS, 391, 237, 0808.2770

Jardine, M., & Collier Cameron, A. 2008, aap, 490, 843, 0808.2889

Jardine, M., Collier Cameron, A., & Donati, J.-F. 2002, MNRAS, 333, 339, astro-ph/0205132

Jardine, M., & Unruh, Y. C. 1999, aap, 346, 883

Jardine, M., Vidotto, A. A., van Ballegooijen, A., Donati, J.-F., Morin, J., Fares, R., & Gombosi, T. I. 2013, MNRAS, 431, 528, 1304.0349

Jeffers, S. V., Petit, P., Marsden, S. C., Morin, J., Donati, J.-F., & Folsom, C. P. 2014, A&A, 569, A79

Jellinek, A. M., & Jackson, M. G. 2015, Nature Geoscience, 8, 587

Johnstone, C. P., Jardine, M., Gregory, S. G., Donati, J.-F., & Hussain, G. 2014, MNRAS, 437, 3202, 1310.8194

Judge, P. G., Solomon, S. C., & Ayres, T. R. 2003, ApJ, 593, 534

Kaltenegger, L., & Traub, W. A. 2009, ApJ, 698, 519, 0903.3371

Kasting, J. F., Kopparapu, R., Ramirez, R. M., & Harman, C. E. 2014, Proceedings of the National Academy of Science, 111, 12641, 1312.1328

Kasting, J. F., Whitmire, D. P., & Reynolds, R. T. 1993, icarus, 101, 108

Kemp, J. C., Swedlund, J. B., Landstreet, J. D., & Angel, J. R. P. 1970, ApJl, 161, L77

Keppens, R., & Goedbloed, J. P. 1999, aap, 343, 251, arXiv:astro-ph/9901380

Khodachenko, M. L. et al. 2007, Astrobiology, 7, 167

Kopparapu, R. K. et al. 2013, ApJ, 765, 131, 1301.6674

Kopparapu, R. K., Ramirez, R. M., SchottelKotte, J., Kasting, J. F., Domagal-Goldman, S., & Eymet, V. 2014, ApJ, 787, L29, 1404.5292

Kruskal, M. D., & Bernstein, I. B. 1964, Physics of Fluids, 7, 407

Küker, M., & Rüdiger, G. 1999, A&A, 346, 922

Laakso, T., Rantala, J., & Kaasalainen, M. 2006, A&A, 456, 373, 1402.7244

Lammer, H. et al. 2009, aapr, 17, 181

——. 2012, Earth, Planets, and Space, 64, 179

——. 2007, Astrobiology, 7, 185

Lang, P., Jardine, M., Donati, J.-F., Morin, J., & Vidotto, A. 2012, MNRAS, 424, 1077, 1207.2165

Lanza, A. F. 2009, A&A, 505, 339, 0906.1738

Lazio, W., T. J., Farrell, W. M., Dietrick, J., Greenlees, E., Hogan, E., Jones, C., & Hennig, L. A. 2004, ApJ, 612, 511

Lazio, T. J. W., & Farrell, W. M. 2007, ApJ, 668, 1182, 0707.1827

Lecavelier Des Etangs, A., Sirothia, S. K., Gopal-Krishna, & Zarka, P. 2009, A&A, 500, L51, 0906.2783

——. 2011, A&A, 533, A50, 1108.3730

Lee, G., Helling, C., Dobbs-Dixon, I., & Juncher, D. 2015, A&A, 580, A12, 1505.06576

Levine, R. H., Altschuler, M. D., & Harvey, J. W. 1977, JGR, 82, 1061

Llama, J., Vidotto, A. A., Jardine, M., Wood, K., Fares, R., & Gombosi, T. I. 2013, MNRAS, 436, 2179, 1309.2938

Llama, J., Wood, K., Jardine, M., Vidotto, A. A., Helling, C., Fossati, L., & Haswell, C. A. 2011, MNRAS, 416, L41, 1106.2935

Lockwood, G. W., Skiff, B. A., Henry, G. W., Henry, S., Radick, R. R., Baliunas, S. L., Donahue, R. A., & Soon, W. 2007, ApJ, 171, 260, astro-ph/0703408

Mamajek, E. E., & Hillenbrand, L. A. 2008, ApJ, 687, 1264, 0807.1686

Marcy, G. W., & Butler, R. P. 1996, ApJ, 464, L147

Marsden, S. C. et al. 2011, MNRAS, 413, 1922, 1101.5859

——. 2014, MNRAS, 444, 3517, 1311.3374

Matt, S. P., MacGregor, K. B., Pinsonneault, M. H., & Greene, T. P. 2012, ApJ, 754, L26, 1206.2354

Mayor, M., & Queloz, D. 1995, Nat, 378, 355

McIvor, T., Jardine, M., Mackay, D., & Holzwarth, V. 2006, MNRAS, 367, 592

McLaughlin, D. B. 1924, ApJ, 60, 22

McQuillan, A., Aigrain, S., & Mazeh, T. 2013, MNRAS, 432, 1203, 1303.6787

Mengel, M. W. et al. 2016, MNRAS, 459, 4325

Messina, S., & Guinan, E. F. 2002, A&A, 393, 225

Mestel, L. 1968, MNRAS, 138, 359

Mestel, L., & Spruit, H. C. 1987, MNRAS, 226, 57

Metcalfe, T. S. et al. 2013, ApJ, 763, L26, 1212.4425

Mohanty, S., & Basri, G. 2003, ApJ, 583, 451, astro-ph/0201455

Morgenthaler, A., Petit, P., Morin, J., Aurière, M., Dintrans, B., Konstantinova-Antova, R., & Marsden, S. 2011, Astronomische Nachrichten, 332, 866, 1109.3982

Morgenthaler, A. et al. 2012, A&A, 540, A138, 1109.5066

Morin, J. et al. 2008a, MNRAS, 384, 77, 0711.1418

——. 2008b, MNRAS, 390, 567, 0808.1423

Morin, J., Donati, J.-F., Petit, P., Delfosse, X., Forveille, T., & Jardine, M. M. 2010, MNRAS, 407, 2269, 1005.5552

Moss, D. 2001, in Astronomical Society of the Pacific Conference Series, Vol. 248, Magnetic Fields Across the Hertzsprung-Russell Diagram, ed. G. Mathys, S. K. Solanki, & D. T. Wickramasinghe, 305

Mullan, D. J. 1979, ApJ, 231, 152

Mullan, D. J., & MacDonald, J. 2005, MNRAS, 356, 1139

Murray-Clay, R. A., Chiang, E. I., & Murray, N. 2009, ApJ, 693, 23, 0811.0006

Musielak, Z. E., & Ulmschneider, P. 2002, A&A, 386, 606

Noyes, R. W., Hartmann, L. W., Baliunas, S. L., Duncan, D. K., & Vaughan, A. H. 1984, ApJ, 279, 763

Oláh, K. et al. 2009, A&A, 501, 703, 0904.1747

Pace, G. 2013, A&A, 551, L8

Pace, G., Melendez, J., Pasquini, L., Carraro, G., Danziger, J., François, P., Matteucci, F., & Santos, N. C. 2009, A&A, 499, L9, 0904.3199

Padhi, C. M., Korenaga, J., & Ozima, M. 2012, Earth and Planetary Science Letters, 341, 1

Papuc, A. M., & Davies, G. F. 2008, Icarus, 195, 447

Parker, E. N. 1955, ApJ, 122, 293

——. 1958, ApJ, 128, 664

Petit, P., Dintrans, B., Morgenthaler, A., Van Grootel, V., Morin, J., Lanoux, J., Aurière, M., & Konstantinova-Antova, R. 2009, A&A, 508, L9, 0909.2200

Petit, P. et al. 2008, MNRAS, 388, 80, 0804.1290

——. 2015, A&A, 584, A84, 1503.00180

Pizzolato, N., Maggio, A., Micela, G., Sciortino, S., & Ventura, P. 2003, aap, 397, 147

Poppenhaeger, K., Günther, H. M., & Schmitt, J. H. M. M. 2012, Astronomische Nachrichten, 333, 26, 1303.0311

Regenauer-Lieb, K., Yuen, D. A., & Branlund, J. 2001, Sci, 294, 578

Reimers, D. 1975, Memoires of the Societe Royale des Sciences de Liege, 8, 369

——. 1977, aap, 61, 217

Reiners, A. 2012, Living Reviews in Solar Physics, 9, 1203.0241

Reiners, A., & Basri, G. 2009, A&A, 496, 787, 0901.1659

Reiners, A., Schüssler, M., & Passegger, V. M. 2014, ApJ, 794, 144, 1408.6175

Réville, V., Brun, A. S., Matt, S. P., Strugarek, A., & Pinto, R. F. 2015, , 798, 116, 1410.8746

Robinson, R. D., Worden, S. P., & Harvey, J. W. 1980, ApJl, 236, L155

Robrade, J., Schmitt, J. H. M. M., & Favata, F. 2012, A&A, 543, A84, 1205.3627

Rosén, L., Kochukhov, O., & Wade, G. A. 2015, ApJ, 805, 169, 1504.00176

Rossiter, R. A. 1924, ApJ, 60, 15

Ryabov, V. B., Zarka, P., & Ryabov, B. P. 2004, Planet. Space Sci., 52, 1479

Saar, S. H., & Brandenburg, A. 1999, ApJ, 524, 295

Sakurai, T. 1985, aap, 152, 121

Schrijver, C. J., Cote, J., Zwaan, C., & Saar, S. H. 1989, ApJ, 337, 964

Schrijver, C. J., & Title, A. M. 2001, , 551, 1099

Schröder, K.-P., & Cuntz, M. 2005, ApJl, 630, L73, arXiv:astro-ph/0507598

Schuessler, M., Caligari, P., Ferriz-Mas, A., Solanki, S. K., & Stix, M. 1996, A&A, 314, 503

Schuessler, M., & Solanki, S. K. 1992, A&A, 264, L13

Schwadron, N. A., & McComas, D. J. 2008, ApJ, 686, L33

See, V., Jardine, M., Fares, R., Donati, J.-F., & Moutou, C. 2015a, MNRAS, 450, 4323

See, V. et al. 2015b, MNRAS, 453, 4301, 1508.01403

See, V., Jardine, M., Vidotto, A. A., Petit, P., Marsden, S. C., Jeffers, S. V., & do Nascimento, J. D. 2014, A&A, 570, A99, 1409.1237

Semel, M. 1989, aap, 225, 456

Shkolnik, E., Bohlender, D. A., Walker, G. A. H., & Collier Cameron, A. 2008, ApJ, 676, 628, 0712.0004

Sirothia, S. K., Lecavelier des Etangs, A., Gopal-Krishna, Kantharia, N. G., & Ishwar-Chandra, C. H. 2014, A&A, 562, A108

Skumanich, A. 1972, ApJ, 171, 565

Smith, A. M. S., Collier Cameron, A., Greaves, J., Jardine, M., Langston, G., & Backer, D. 2009, MNRAS, 395, 335, 0901.2344

Soderblom, D. R., Duncan, D. K., & Johnson, D. R. H. 1991, ApJ, 375, 722

Sterenborg, M. G., Cohen, O., Drake, J. J., & Gombosi, T. I. 2011, J. Geophys. Res., 116, 1217, 1102.0003

Stevens, I. R. 2005, MNRAS, 356, 1053, astro-ph/0410600

Strassmeier, K. G. 2002, AN, 323, 309

Tarduno, J. A. et al. 2010, Science, 327, 1238

Thompson, M. J., Christensen-Dalsgaard, J., Miesch, M. S., & Toomre, J. 2003, ARAA, 41, 599

Treumann, R. A. 2006, A&AR, 13, 229

Triaud, A. H. M. J. et al. 2009, A&A, 506, 377, 0907.2956

van Ballegooijen, A. A., Cartledge, N. P., & Priest, E. R. 1998, ApJ, 501, 866

van Saders, J. L., & Pinsonneault, M. H. 2012, ApJ, 746, 16, 1108.2273

Vaughan, A. H., & Preston, G. W. 1980, PASP, 92, 385

Vidotto, A. A. et al. 2016, MNRAS, 455, L52, 1509.08751

Vidotto, A. A., Fares, R., Jardine, M., Donati, J.-F., Opher, M., Moutou, C., Catala, C., & Gombosi, T. I. 2012, MNRAS, 423, 3285, 1204.3843

Vidotto, A. A., Fares, R., Jardine, M., Moutou, C., & Donati, J.-F. 2015, MNRAS, 449, 4117, 1503.05711

Vidotto, A. A. et al. 2014, MNRAS, 441, 2361, 1404.2733

Vidotto, A. A., Jardine, M., & Helling, C. 2010, ApJl, 722, L168, 1009.5947

Vidotto, A. A., Jardine, M., Morin, J., Donati, J. F., & Lang, P. 2013, MNRAS

Vidotto, A. A., Jardine, M., Opher, M., Donati, J. F., & Gombosi, T. I. 2011, MNRAS, 412, 351, 1010.4762

Vidotto, A. A., Opher, M., Jatenco-Pereira, V., & Gombosi, T. I. 2009, ApJ, 699, 441, 0904.4398

Vilhu, O. 1984, A&A, 133, 117

Waite, I. A., Marsden, S. C., Carter, B. D., Hart, R., Donati, J.-F., Ramírez Vélez, J. C., Semel, M., & Dunstone, N. 2011, MNRAS, 413, 1949, 1102.3475

Wang, Y.-M., & Sheeley, Jr., N. R. 1990, ApJ, 355, 726

——. 1991, ApJ, 372, L45

Weber, E. J., & Davis, Jr., L. 1967, ApJ, 148, 217

Werner, S. C. 2009, Icarus, 201, 44

West, A. A., Hawley, S. L., Bochanski, J. J., Covey, K. R., Reid, I. N., Dhital, S., Hilton, E. J., & Masuda, M. 2008, AJ, 135, 785, 0712.1590

Wilson, O. C. 1978, ApJ, 226, 379

Winn, J. N., Fabrycky, D., Albrecht, S., & Johnson, J. A. 2010, ApJ, 718, L145, 1006.4161

Wood, B. E. 2004, Living Reviews in Solar Physics, 1

——. 2006, ssr, 126, 3

Wood, B. E., & Linsky, J. L. 2010, ApJ, 717, 1279, 1005.3281

Wood, B. E., Müller, H.-R., Redfield, S., & Edelman, E. 2014, ApJ, 781, L33

Wood, B. E., Müller, H.-R., Zank, G. P., & Linsky, J. L. 2002, ApJ, 574, 412, astro-ph/0203437

Wood, B. E., Müller, H.-R., Zank, G. P., Linsky, J. L., & Redfield, S. 2005, ApJl, 628, L143, arXiv:astro-ph/0506401

Wright, N. J., Drake, J. J., Mamajek, E. E., & Henry, G. W. 2011, ApJ, 743, 48, 1109.4634

Yadav, R. K., Christensen, U. R., Morin, J., Gastine, T., Reiners, A., Poppenhaeger, K., & Wolk, S. J. 2015, ApJ, 813, L31, 1510.05541

Zarka, P. 1998, , 103, 20159

——. 2007, , 55, 598

Zarka, P., Treumann, R. A., Ryabov, B. P., & Ryabov, V. B. 2001, apss, 277, 293

Zendejas, J., Segura, A., & Raga, A. C. 2010, icarus, 210, 539, 1006.0021